FLORIDA INTERNATIONAL UNIVERSITY

Miami, Florida

SYNTHESIS AND CHARACTERIZATION OF BIOMIMETIC OXO- AND HYDROXO-BRIDGED DINUCLEAR COPPER PYRAZOLATE COMPLEXES, THEIR REDOX AND OXYGEN TRANSFER CHEMISTRY

A dissertation submitted in partial fulfillment of

the requirements for the degree of

DOCTOR OF PHILOSOPHY

in

CHEMISTRY

by

Eduardo Mollinedo

2023

To: Dean Michael R. Heithaus
College of Arts, Sciences and Education

This dissertation, written by Eduardo Mollinedo, and entitled Synthesis and Characterization of Biomimetic Oxo- and Hydroxo-Bridged Dinuclear Copper Pyrazolate Complexes, Their Redox and Oxygen Transfer Chemistry, having been approved in respect to style and intellectual content, is referred to you for judgment.

We have read this dissertation and recommend that it be approved.

_____

Konstantinos Kavallieratos

_____

Christopher Dares

_____

Sonia Underwood

_____

Jiuhua Chen

_____

Raphael G. Raptis, Major Professor

Date of Defense: June 28, 2023

The dissertation of Eduardo Mollinedo is approved.

_____

Dean Michael R. Heithaus
College of Arts, Sciences and Education

_____

Andrés G. Gil
Vice President for Research and Economic Development
and Dean of the University Graduate School

Florida International University, 2023

ACKNOWLEDGMENTS

I would like to thank my advisor Professor Raphael G. Raptis for his dedication and unwavering perseverance. It is with his continuous support that this work was made possible, I thank him for pushing and elevating me to reach new heights, and I strive to make him proud of both myself and this work as his graduate student.

I would like to extend my gratitude to my committee members, Prof. Konstantinos Kavallieratos, Prof. Christopher Dares, Prof. Sonia Underwood, and Prof. Jiuhua Chen. Their advice and support throughout this journey are greatly appreciated.

I would like to extend my gratitude to the members of the Raptis lab, both old and new, without their help and motivation, I fear this project would not have come to fruition. I would like to extend an extra special thanks to the two post docs I was lucky enough to have met along this journey, Drs Logesh Mathivathanan and Indranil Chakraborty. I would also like to extend my gratitude to the members of the chemistry department at FIU, and the graduate/undergraduate students whom have helped make this work possible.

Lastly, I would like to extend my gratitude to my family for supporting me through this journey. I am grateful they were able to stand up to the Cuban Castro regime and make a better life for themselves and I in the United States of America. I am forever grateful towards them and their sacrifices.

ABSTRACT OF THE DISSERTATION

SYNTHESIS AND CHARACTERIZATION OF BIOMIMETIC OXO- AND HYDROXO-BRIDGED DINUCLEAR COPPER PYRAZOLATE COMPLEXES, THEIR REDOX AND OXYGEN TRANSFER CHEMISTRY

by

Eduardo Mollinedo

Florida International University, 2023

Miami, Florida

Professor Raphael G. Raptis, Major Professor

The project entailed a detailed study of the properties of biomimetic oxo- and hydroxo/alkoxo-bridged dinuclear copper(II) pyrazole complexes. The chemistry of the complexes and their ability to undergo a reversible reduction/oxidation process coupled with oxygen transfer is of great interest, due to their potential applications in industrial catalytic oxygenation as well as their relevance to biological oxidation/oxygenation of organic substrates. The project's proposed goals included: 1) optimization of the synthesis of dicopper(II) complexes, 2) exploring the synthesis and study of related new dicopper complexes, and 3) the study of their oxygenation/oxidation chemistry. Spectroscopic techniques, such as UV-Vis, Fourier transform infrared (FTIR), were applied to the characterization studies of the complexes, and single-crystal X-ray diffraction for structure determination. Electrochemical studies were carried out in comparison to analogous biological copper-based enzymes and their synthetic models, while spectroscopic and gas chromatographic techniques applied to the systems reveal their catalytic processes. The results of the project are intended to be relevant to biological oxygen delivery systems.

Table of Contents

Chapter Page

LIST OF FIGURES

FIGURE PAGE

LIST OF SCHEMES

SCHEME PAGE

ABBREVIATIONS AND ACRONYMS

ATR	Attenuated Total Reflection
BDE	Bond Dissociation Energy
CV	Cyclic Voltammetry
DCM	Dichloro Methane
DFT	Density Functional Theory
DMSO	Dimethyl Sulfoxide
FTIR	Fourier-Transform Infrared Spectroscopy
GCMS	Gas Chromatography-Mass Spectrometry
HDS	Hydrodesulfurization Process
MCO	Multicopper Oxidases
MSM	Methyl Sulfonyl Methane
NMR	Nuclear Magnetic Resonance
pMMO	Particulate Methane Monooxygenase
ROE	Ring Opening Event
sMMO	Soluble Methane Monooxygenase
SSI	Secondary Sphere Interaction
TOF	Turn Over Frequency

TON	Turn Over Number
TPA	Terephthalic Acid
TPAOH	2-Hydroxyterephthalic Acid

Chapter 1: Introduction

1.1: Copper background

Copper (elemental symbol Cu) is a first-row transition metal with a rich history. Elemental copper has an atomic weight of 63.546, atomic number of 29, and a simplified electronic configuration of $[Ar]3d^{10}4s^{1}$, and it is the 26^{th} most abundant element in the crust of the Earth. In the natural world, copper is found in many combination minerals, such as chalcocite, bornite, malachite and cuprite. Copper is an excellent conductor of heat and electricity, as well as a malleable, flexible metal. Trace amounts of copper are found in nearly all living organisms with important roles in the physiology of humans ranging from red blood cell production, iron adsorption, and as an essential component of metalloproteins. Copper metalloproteins typically play important roles in the metabolic pathways of the human body [1]. Copper containing metalloproteins in Nature are also known to mediate catalytic reactions as either electron sources or accepters (*vide infra*). While trace amounts of copper are essential to the proper functions of the body, high concentrations lead to adverse effects, including tissue damage, Alzheimer's and Parkinson's disease, and various forms of cancer [2]. Dimeric copper species, on the other hand, have been proposed as possible anti-cancer agents [3]. In this work the role of copper in biological and synthetic systems, as well as the importance of the secondary sphere interactions that may or may not be present, is explored.

1.1.1: Metal-oxide catalysis

Catalysts are always in high demand in today's world, whether for biological system modeling [4], industrial processes [5], or laboratory synthesis of new compounds with

currently around 90% of all reactions involving a catalytic step. While the field has certainly come a long way since the early days of the 1950's, a renaissance of renewed fervor sparked by a demand for greener, more sustainable chemistry has gripped the chemical world in recent years. Typical catalysts can be subdivided into three categories: heterogenous catalysis, homogenous catalysis, and biocatalysts, with the majority (80%), falling into the first category, and the remaining (17%, 3% respectively) making up the rest [6]. Metal-oxide complexes rose to the forefront of catalysis research due to their abilities to mediate a wide range of reactions, including oxidations and acid-base reactions. Examples of such catalysts range from simple oxides; silica, alumina, zinc oxide, copper oxide, and zeolites, to the more complex porous and mesoporous metal oxides; MOF's, polyoxometalates, and perovskites [7]. Table 1 Summarizes some important industrial metal oxide catalysts.

Table 1. Industrially important metal oxide catalysts and their applications. Redrawn from reference [7].

Catalyst	Applications
SiO_2–Al_2O_3, acid zeolites	acid-catalyzed reactions, for example, FCC, isomerization
Fe_2O_3, CoO_x	Fischer–Tropsch reaction, ethyl benzene dehydrogenation to styrene
TiO_2	major component of deNO_x catalysts and photocatalysts
ZrO_2–SO_4^{2-}	isomerization
Cu–ZnO/Al_2O_3	methanol synthesis from H_2/CO mixtures
$(VO)_2P_2O_7$	selective oxidation of butane to maleic anhydride, of pentane to phthalic anhydride+maleic anhydride
$FePO_4$ and its hydrates	oxidation of methacrolein to methacrylic acid
Cu–Cr oxides	hydrogenation, combustion reactions
$AlPO_4$	acid-catalyzed reactions, polymerization
Sn–Sb oxides	selective oxidation, as propene to acrolein or isobutene to methacrolein
Bi molybdates	propene selective oxidation/ammoxidation to acrolein/acrylonitrile
V–Mo oxide	selective oxidation of acrolein to acrylic acid
MoVTeNbO	direct propane (amm)oxidation to acrylic acid (acrylonitrile)

Of particular interest are their (metal oxides) ability to transfer O-atoms and attack even the stronger C-H bonds [8]. Reactions are typically carried out in heterogeneous gas/solid or liquid/solid phases with the complex in the solid phase, or in homogeneous liquid solutions [9]. Selective, controlled oxidation of primary, secondary, and tertiary alkanes is a difficult endeavor, with bond dissociation energies around and above 100 kcal mol^{-1} and the challenges of overoxidation, where it is not uncommon to start with a primary alkane and end up with the corresponding carboxylic acid, or CO_2 (Figure 1). The challenges of selectivity arise from the lower C-H dissociation energies of the alcohol and aldehyde

products *vs.* unactivated saturated alkanes (e.g., CH_4), typically leading to the formation of more oxidized products [10].

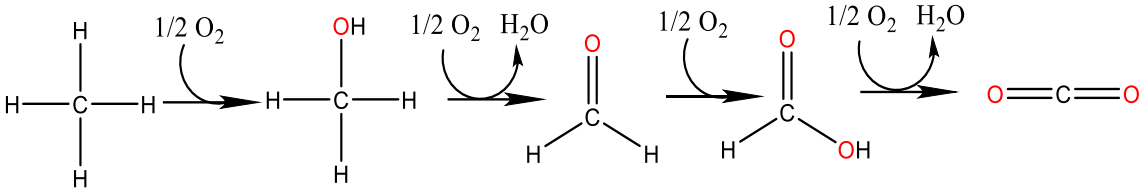

Figure 1: Progression of successive aliphatic alkane oxidations.

Functionalization of carbon-hydrogen bonds by metal-oxide complexes has been observed and studied for nearly every transitional metal in the periodic table [11]; Certainly, this is a well-known and well-studied area of chemistry to which copper is no exception. The most common copper-oxygenation complexes contain the Cu^{III}-O, $Cu^{II}(\mu\text{-}\eta^2\text{:}\eta^2\text{-}(O_2)Cu^{II}$, $Cu^{III}(\mu\text{-}O)_2Cu^{III}$, and Cu^{II}—OOH motifs (Figure 2).

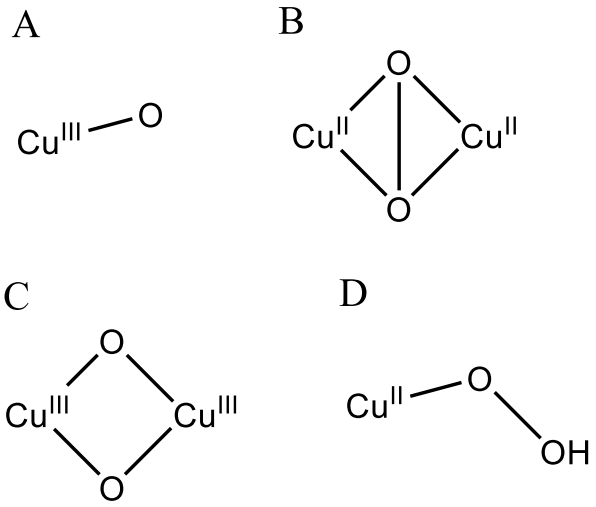

Figure 2. Common motifs of copper-based catalysts, (A) Cu^{III}-O, (B) $Cu^{II}(\mu\text{-}\eta^2\text{:}\eta^2\text{-}(O_2)Cu^{II}$, (C) $Cu^{III}(\mu\text{-}O)_2Cu^{III}$, and (D) Cu^{II}—OOH motif.

The oxidation of alkanes typically occurs via one of two pathways: the "oxygenase", or the "oxidase" pathway. In the oxygenase mechanism, an O-atom is transferred directly from the complex to the substrate, and the catalyst is regenerated by dioxygen. Particulate

methane monooxygenase (pMMO) is an example of a biological protein that employs this mechanism and synthetic oxo- and hydroxo-bridged diiron complexes have been extensively studied as oxygenase models [12]. The oxidase mechanism, on the other hand, couples the reduction of O_2 to H_2O or H_2O_2 and does not necessarily transfer an O-atom directly to the substrate; Figure 3 shows the two pathways of action [13]. Catalytic activity is evaluated by the turnover number (TON), measured in moles of substrate converted by one mole of the catalyst, and turnover frequency (TOF), the number of substrate moles converted per time units. While current synthetic catalysts have good TOF's, they are relatively poor with regard to their TONs, as they typically cannot survive in highly oxidative environments for long before catalytic poisoning occurs. Nature faces a similar situation where the catalysts do not survive for many cycles, however, they are constantly being replaced with new biosynthesized batches to keep up with demands, an option that is not feasible for synthetic models to date.

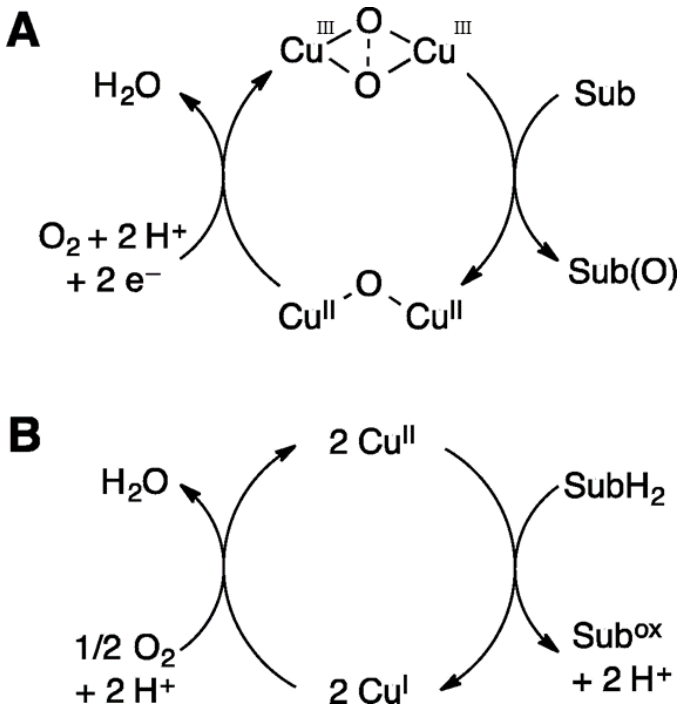

Figure 3. Oxygenase (A) and Oxidase (B) catalytic cycles. Adapted from reference [13].

1.2: Copper-containing enzymes and catalysts

Enzymes and catalysts play an important role in the mediation of chemical reactions, whether in biological or synthetic systems, and their reactivity is one of the most studied fields [14]. Transition metals, typically bound to proteins or in embedded cofactors, play an important role in biological catalysis. Perhaps the best-known examples being cytochrome P-450 (a heme iron species) with the ability to reversibly bind dioxygen and perform crucial oxygen transport chemistry, and soluble methane monooxygenase (sMMO), a dinuclear iron species that oxidizes methane to methanol [15] [16]. The chemistry of copper complexes is no exception, as evident by a large number of enzymes that use copper ions in respiration, oxidation and oxygenation processes, enabled by their ability to cycle among the Cu^{0}, Cu^{I}, Cu^{II}, and Cu^{III} oxidation states, a feature that allows copper to act through multiple pathways [17]. Typically, the rigid structure of the proteins

or synthetic complexes allows for one type of substrate to precisely interact with the active site/sites and lower the activation energy of the reaction without influencing the reaction's thermodynamics. In Nature, biological enzymes are often in close proximity to metal cofactors; iron, cobalt, copper, etc., which are responsible for the facilitation of the transport and transfer of electrons [18]. Copper containing enzymes and metalloproteins, in the last few decades have warranted much attention and study due to their pivotal roles in biological functions; dioxygen transport and activation, oxidation and catalysis of organic molecules, and most notably vital roles in electron transfer chemistry [19] [20]. The typical active centers are classified as type I, type II, and type III, which can be differentiated based on their spectroscopic and metal ion characteristics. Type I or "blue" copper proteins adopt a strongly distorted (almost exclusively trigonal planar or tetrahedral) coordination environment and typically possess a weakly Cu-coupled EPR spectrum [21]. Type II, "non-blue" copper proteins adopt a more planar coordination environment, a weak absorption in the visible light region, and a "normal" EPR spectrum with axial symmetry. Both type I and type II feature a single copper center. Of more recent interest are the type III species, which feature dimeric copper centers usually bridged by O-atom(s) and are EPR-silent due to antiferromagnetic coupling of the d^9 copper centers [22]. Today, as new data emerged, the classification types have increased and the number has been expanded from three to seven to include: Type IV, Cu_A, Cu_B, and Cu_Z. Type IV active sites typically combine type II and III to form a trinuclear site; Cu_A actives sites contain two delocalized mixed-valent Cu atoms with formal oxidation states of +1.5. Cu_B, contains a single Cu atom bonded to three His residues of which one is covalently bonded to a Tyr residue. Lastly, there is the Cu_Z active site, which contains four Cu atoms linked

by sulfur atoms; currently there is only one known representative enzyme of this species, N_2O reductase. Table 2 summarizes the known biological copper containing active sites.

Table 2. Summary of copper containing sites in biological proteins, adapted from references [23].

Entry	Active site(s)	Active site geometry	Main ligands	Function	UV-Vis (nm)	$g_{\perp}$	Example
Type I	Mono-nuclear	Distorted tetragonal, Trigonal planar	His, Cys, (Met)	Electron transfer	Strong 600 nm	Quartet	Nitrite reductase
Type II	Mono-nuclear	Distorted tetragonal	His, Asp, (Tyr)	Catalysis	Weak 700 nm	Quartet	Galactose oxidase
Cu_B	Mono-nuclear	Trigonal pyramid	His	Oxygen transport	Weak 610 nm	Quartet	Cytochrome C oxidase
Type III	Di-nuclear	Tetragonal Cu_2O_2	His, (Tyr)	Oxygen transport/ oxidation	Weak 700 nm	EPR-silent	Catechol oxidase
Cu_A	Di-nuclear	Tetragonal Cu_2O_2	His, Cys, (Met)	Oxygen transport	Strong 480, 530-580, 800 nm	Septet	Cytochrome C oxidase (Cu_A site)
Type IV	Tri-nuclear	Type II + III (Tetragonal)	His	Catalysis	Weak ~330, 600 nm	EPR-silent	Ascorbate oxidase
Cu_Z	Tetra-nuclear	Distorted tetrahedron	His, S^{2-}	Catalysis	Strong ~640 nm	Two Quartets	N_2O reductase

Dinuclear copper species have been found to activate myriad reactions of varying complexity. An enzyme containing a dicopper core, pMMO, converts methane to methanol. Dicopper cores are also present in enzymes, such as tyrosinase, and many multicopper oxidases/oxygenases (MCO) [24]. Metal-oxo complexes are of interest due to their ability to transfer O-atoms and attack even the stronger C-H bonds. Oxygen-bridged

copper(II) dimers usually have one of two motifs: a μ-O, or μ-OH bridge. Characterization by SCXRD reveals notable differences between the two forms; μ-O bridges tends to be closer to linear (~120-160°), with the two copper centers located further apart (~3.3-4.3 Å), while μ-OH bridges have more acute copper-oxygen-copper bond angles (~90-109.5°) and the two copper centers in closer proximity to each other (2.9-3.5 Å) (Figure 4) [25]. In biological proteins, the angle is determined by the organic bridging ligands (protein backbone) that hold the two Cu atoms in their positions while in synthetic models, especially bent-oxo species, bond angles are determined by the support scaffolding (zeolites, bridging and auxiliary ligands, etc.) of the complexes.

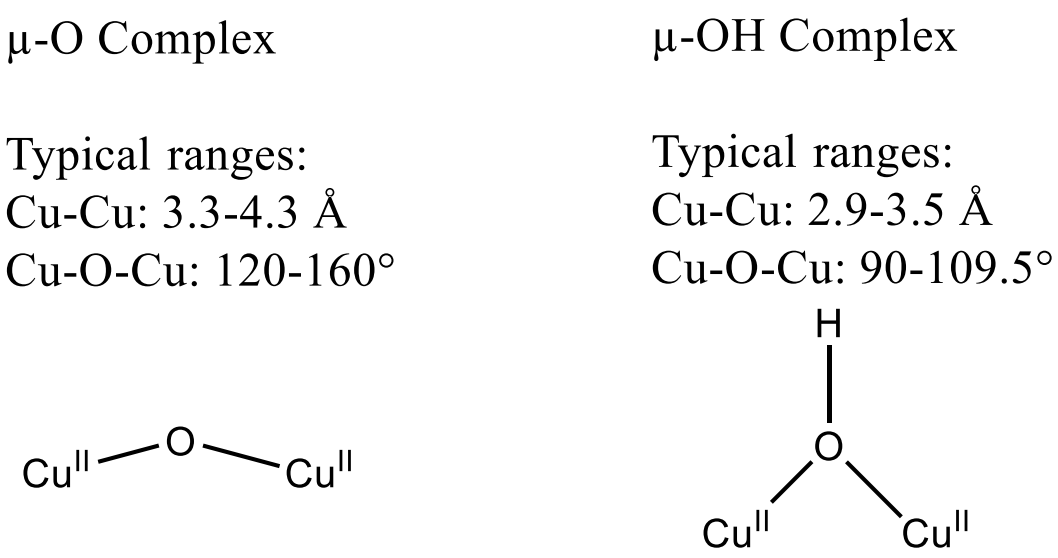

Figure 4. Comparison of μ-O vs. μ-OH Cu-dimers.

In terms of stability, the μ-O motif is the more reactive of the two, while μ-OH motifs remain relatively stable. The reactivity of the μ-OH motif increases upon deprotonation. Examples are known of reactive bent μ-O motifs with H-bonded ligands in the secondary coordination sphere that impart stability to the complexes [26]. Then, as incoming substrates in solution disturb the H-bonding, the complex becomes reactive towards

oxygen transfer chemistry. This is in sharp contrast to copper(II) trimers where the oxygen atom sits directly in the center of three copper metal centers in planar fashion. In this case, oxidative reactivity has been reported upon oxidation of the copper center(s) to copper(III). It is now recognized that the secondary coordination sphere of metal centers in metalloproteins is important in modulating their catalytic activity [27]. This secondary sphere consists of a set of H-bonds to the protein backbone surrounding the copper active center. Synthetic catalysts capable of mimicking bioproteins and selectively oxidizing alkanes are of great interest, with studies into their catalytic mechanisms providing new insights into the topic. Copper(II) has a d^9 electron configuration, S = 1/2, which can lead to either ferromagnetic or antiferromagnetic coupling of the metal centers in multinuclear complexes [28]. In the literature, it has been shown that a hydroxo-bridged dicopper(II) complex can undergo two one-electron oxidations and readily switch between the dicopper(II), the mixed-valence dicopper(II/III), and the dicopper(III) species [29]. In the II/III case, intervalence charge transfer (IVCT) transitions between the two delocalized heterovalent metal centers produce characteristic absorption bands. These typically occur in the near-IR region and can lend some insight as to the nature of the mixed-valence species. The formation of fully delocalized mixed valence copper dimers in a biological system is not uncommon [30].

1.3: Dioxygen activation and aerobic oxidation

Dioxygen is an abundant natural oxidant; however, as far as industrial oxidation processes are concerned, it remains largely untapped as it contains a strong oxygen-oxygen bond (119 kcal/mol) and a triplet ground state, two contributing factors to the thermodynamic

stability and inertness (kinetic stability) of the molecule. The triplet ground state arises from the two unpaired electrons in the anti-bonding π_{2px}* and π_{2py}* HOMO (Figure 5).

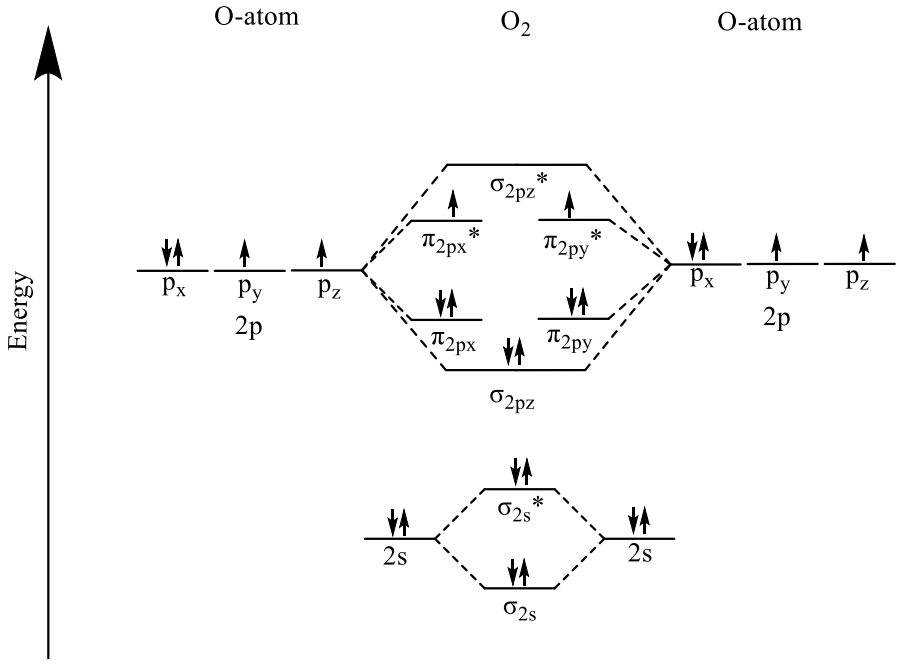

Figure 5. Molecular orbital diagram for the formation of O_2.

A catalyst is required to both lower the activation energy and provide a selective pathway for the desired reactions [31] [32]. One of the inherent challenges of O_2 with respect to alkane oxidation, is over oxidation, as a four-electron oxidant is used to achieve a two-electron oxidation. The second challenge comes with the use of first row transition metals, which tend to undergo one-electron redox steps (Cu^{I}/Cu^{II} to Cu^{II}/Cu^{III}). To overcome this limitation, the use of multinuclear complexes (dimers, trimers, etc.) are typically employed. These types of complexes are capable of oxidative carbon-heteroatom bond-forming reactions (C-H oxidations). Cu^{II} dimers offer certain advantages over analogous second and third row transition metals, which are not limited to one-electron oxidations (e.g. Pd^{0}/Pd^{II} couple), mainly in being able to employ milder oxidants, such as O_2. Molecular

oxygen is an ideal terminal oxidant, as it is much more desirable than alternatives, such as hypervalent iodine or electrophilic halogen sources. These aerobic oxidations can accomplish one-electron, two-electron, and four-electron processes. Likewise, the oxidation of alkanes typically involves highly oxidizing species, where it is not uncommon for oxidative damage of the catalyst to occur, especially in coordination compounds and organic ligand bearing organometallic complexes. While oxidations of the precatalysts may result in novel complexes that can act as catalytic species in homogenous solutions, typically, catalyst poisoning or decomposition results [33]. O_2, being a milder oxidizing agent, helps mitigate precatalyst oxidation reactions. Current copper research focuses on oxygen transfer via mononuclear and dinuclear complexes that mimic metal ion enzymes [34]. Likewise, synthetic complexes are intended to work as oxygenases, with the ability to harness O atoms for oxidation of alkanes [35]. Of particular interest are dinuclear copper(II) complexes as new evidence suggests that they behave similarly to the particulate form of methane monooxygenase (pMMO), an important transmembrane metalloprotein capable of oxygenating methane to methanol (*vide infra*) [36]. The study suggests that when the bridging oxygen atom of a $Cu_2(\mu\text{-}O)$ unit is in a bent configuration ($90°<\theta<135°$), the complexes tend to be unstable and reactive towards oxidation [37]. The presence of nearby amino acid residues enables the formation of a hydrogen bond between the oxygen bridge and the amino acid residue stabilizing the bridging oxygen. To initiate the catalytic turnover, the metals must be reduced and subsequentially activated by O_2 to form the reactive species; the two copper centers are thus held in proximity to facilitate the switching between their two most common oxidation states, Cu^{I}_2 and $Cu^{II}_2(\mu\text{-}O/OH/O_2)$, in biological systems by transferring electrons and O-atoms. A notable example is a transmembrane

protein, cytochrome-c oxidase, which regulates cellular oxygen levels with pairs of electron donors and acceptors, such as NO and NO_2^-. Cytochrome-c oxidase itself contains a binuclear active site [38]. Like cytochrome-c oxidase, MMO has been extensively studied, and while the details of the binuclear iron sites of the soluble form (sMMO) are well known, the particulate form, pMMO, has not been settled yet. The most widely accepted crystal structure of pMMO shows a binuclear copper active site at a metal-metal distance that raises some controversy. The TON of pMMO is estimated to be between 25-130 mmol min^{-1} and its TOF is in the range of 3-16 min^{-1} [39]. In the synthetic world, some Cu^I complexes catalyze the four-electron reduction of dioxygen to water as they are oxidized to their Cu^{II} analogs [40]. Regeneration of the catalysts involve an O_2-mediated Cu(I) to Cu(II) redox step [41]. One-half O_2 molecule is required to facilitate the oxidation to hydroxo/oxo active complexes, while a full O_2 molecule is required for peroxo and related species.

1.4: Biological enzymes

Copper-containing biological enzymes are typically large macromolecules with complex chemical properties and structures, however, the active site, where catalysis occurs, only accounts for a small portion of the structure, and are largely dependent on primary and secondary sphere interactions, as well as incoming substrate dynamics. These enzymes encompass a wide range of diversity in Nature including plants, mammals, and most famously bacteria, with important roles in catalysis, specifically electron transfer and substrate redox chemistry [42]. Plenty of examples exist for both aerobic and anerobic oxidations of substrates. While the aerobic oxidation of methane to methanol has been

exhaustively studied, it should be noted that bacterial species capable of anaerobically oxidizing methane – e.g. particulate methane monooxygenase (pMMO) found in all methanotrophs, are known as well (Figure 6) . Another well-known example includes the (anerobic/aerobic) oxidation of ammonium (Figure 7). While anerobic oxidations are certainly fascinating, the focus of this work is on aerobic oxidations in an open atmosphere.

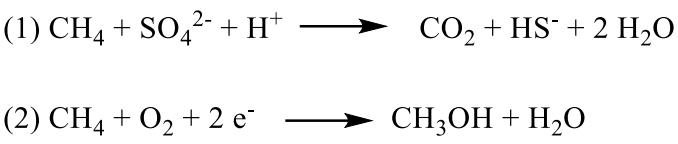

Figure 6. Schemes for (1) the anaerobic oxidation of methane to carbon dioxide, sulfide, and water by anaerobic methanotrophic archaea [43] and (2) the aerobic oxidation to methanol and water by methanotrophic bacteria [44].

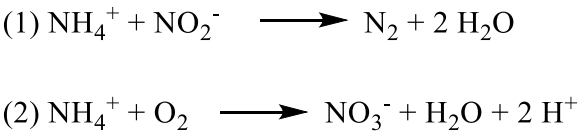

Figure 7. Schemes for (1) the anaerobic oxidation of ammonium to dinitrogen and water by Candidatus K. stuttgartiensis [45]and (2) the aerobic oxidation to nitrate and water by Nitrosomonas eutropha [46].

1.4.1: Biological enzymes: Catechol oxidase

Catechol oxidase, also known as o-diphenol oxidase, is a type III copper-containing enzyme responsible for catalyzing, as the name suggests, the oxidation of catechols to their corresponding o-quinones, a two-electron process (Scheme 1) [47].

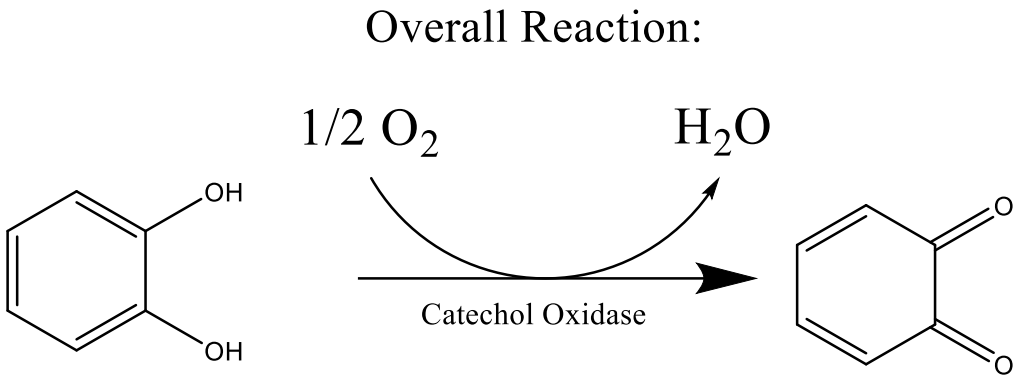

Scheme 1. Oxidation of catechol to o-benzoquinone.

Catechol oxidase was first purified in 1937 from a variety of fruits and vegetables, with varying molecular weights depending on the source of origin [48]. In 1998, Krebs et al. published the crystal structure of the protein, including the active site in the Cu^{II}_2 resting state [49]. The enzyme employs a dicopper(II) hydroxo-bridged complex (Cu-O-Cu angle: 92°) with six terminal N-histamines, and a 1.9 Å hydroxide-bridge between the tetrahedrally coordinated Cu atoms at a distance of 2.9 Å (Figure 8).

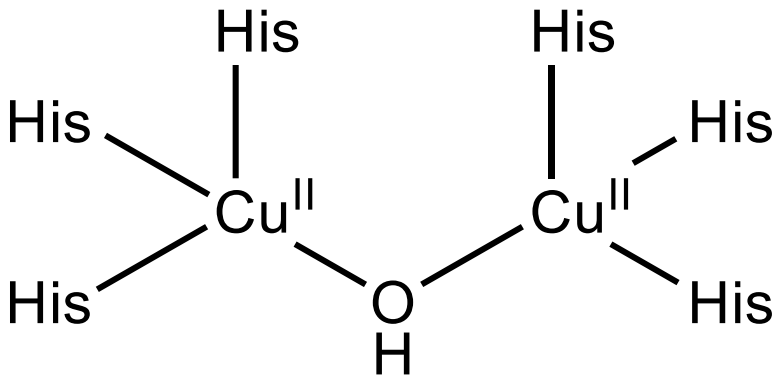

Figure 8. Catechol oxidase active site. Cu-Cu distance: 2.9 Å; Cu-O distance: 1.9, 1.89 Å; Cu-O-Cu angle: 92°.

The complete mechanism for the oxidation to o-quinones remains disputed, however, Scheme 2 shows the mechanism proposed by Krebs *et al.* based on spectroscopic evidence and X-ray data [50]. From the resting Cu^{II}_2 state, the incoming substrate binds to one of the

Cu centers to form an intermediate Cu^{II}/Cu^{II} species which is converted to the reduced Cu^{I}_2 species. In this state, the two Cu atoms are further apart, at ~4.4 Å, lacking the hydroxo-bridging ligand which has instead turned into a coordinated water molecule. The coordination geometry can best be described as distorted square planar about $Cu^{I}A$ and trigonal pyramidal about $Cu^{I}B$. To regenerate the complex, a molecule of water, and a second molecule of catechol coordinate to the active site, resulting in the Cu^{I} centers being oxidized to Cu^{II} and the formation of a peroxo-bridge with water as a byproduct. In the final step, O-O bond cleavage generates the resting state of the complex, as well as water, and a second molecule of o-quinone.

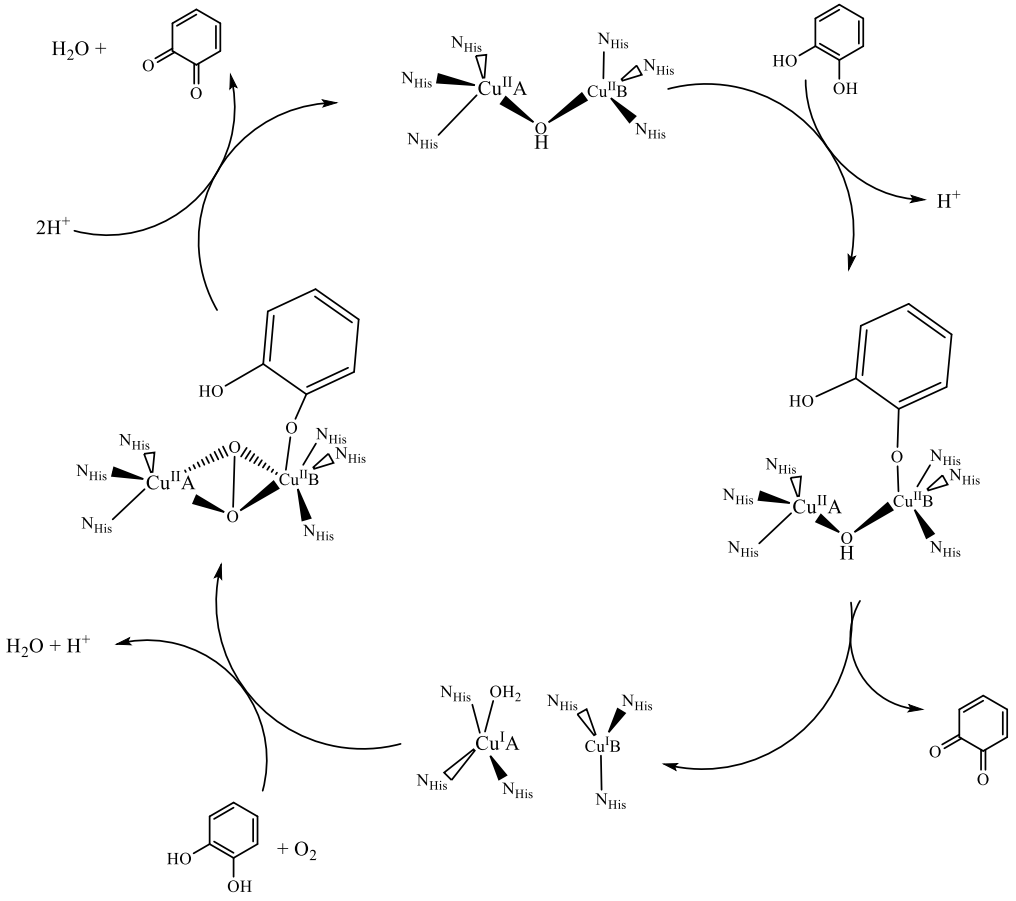

Scheme 2. Catechol oxidase mechanism proposed by Krebs et al. Redrawn from reference [50].

Solomon *et al.* proposed a similar mechanism to Krebs *et al.* with differences in the binding modes of catechol, where it is argued that due to strong σ donation to the Cu centers, the peroxo-bridge is more electrophilic in nature than end-on peroxycopper(II) complexes, which are more nucleophilic. Solomon *et al.* further argued that it is the peroxo σ* orbital's participation in back-bonding with the Cu centers that creates the extremely weak O-O bond, rendering it susceptible to bond cleavage [51]. In a 2004 study, Siegbahn argued that the O-O bond cleavage is the rate-determining step of the mechanism and that no outside proton transfer to or from protein residues outside the metal complex are needed [52]. Kinetics studies suggest that the rate-limiting step includes proton transfer [53].

1.4.2: Biological enzymes: particulate MMO

To this day, no synthetic catalyst is able to harness O_2 to directly convert methane to methanol, and while oxidative C-H activation of methane is thermodynamically and kinetically feasible at low temperatures, the large bond dissociation energies has hindered progress in this field for the past 100 years [54]. The oxidation of alkanes is both challenging and cumbersome in an industrial setting as well as in Nature, nonetheless, the oxidation of small molecules, such as methane, may play an important step in the energy, pharmaceutical, and agricultural sectors [55]. Of particular interest to the energy sector, where greenhouse emissions are intensely scrutinized, is a biomimetic complex capable of methane activation (C-H: 105 kcal/mol); an important goal of climate policy across the world [56]. In Nature this is accomplished remarkably well by methane monooxygenase and is often seen as the holy grail of catalytic reactions. Perhaps the best-known avenue in gaining insight in this field is the study of methanotrophic bacteria, dating back to when they were first discovered some one hundred years ago by Kaser and Söhngen [57] [58].

The two known forms include the soluble form (sMMO) and the membrane-bound particulate form (pMMO). Currently no other metalloprotein or biomimetic compound is capable of readily achieving this reaction to a satisfying degree. The non-heme diiron containing sMMO has been exhaustively studied and is well understood, however, the copper containing pMMO warrants further research, especially with regard to the nuclearity of the copper active site(s) and the mechanism of action. Rosenzweig *et al.* crystallized the protein from M. capsulatus (Bath) showing three active sites: a mononuclear copper site, a dinuclear copper site (Figure 9), and a second mononuclear zinc site [59]. The full mechanism and even structure of the active sites remains largely debated. EXAFS data indicate placing the activation of O_2 at the dinuclear site, consistent with a short Cu-Cu distance of 2.5 Å, however, crystallographic data remain ambiguous at best [60]. It is now accepted that methane oxidation occurs at the dinuclear copper active site [61].

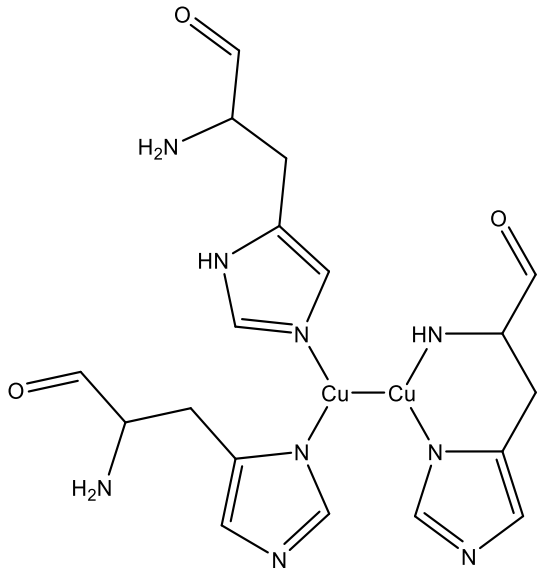

Figure 9. Proposed pMMO dinuclear copper active site in the resting state is shown. Cu-Cu distance: 2.5 Å.

While there is a lack of similar well-characterized sites in the literature, the proposed pMMO copper active sites do share characteristics consistent with Cu_A and type III dinuclear Cu centers of tyrosine, hemocyanin and multicopper oxidases. The EPR signal is more consistent with a type II copper signal further adding to the ambiguity of the active site, although fully delocalized Cu_A centers can give the appearance of a fully localized mononuclear Cu center [62]. The mechanistic understanding of pMMO is so far behind sMMO due to difficulties in isolating the protein, and instead current research focuses on discovery on biomimetic synthetic analogues. DFT and QM/MM studies suggest that a mixed valent $Cu^{II}Cu^{III}$ species could in fact be responsible for the oxidation of methane. Using the dicopper active site as a model, the formation of a μ-η^1:η^2-peroxo $Cu^{I}Cu^{II}$ or μ-η^2:η^2-peroxo $Cu^{II}Cu^{II}$ species is likely to form first, followed by O-O bond cleavage to generate a more reactive μ-oxo $Cu^{II}Cu^{III}$ species [63] [64]. In follow up studies, a (μ-O)(μ-OH)$Cu^{II}Cu^{I}$ center was shown to be more reactive towards methane oxidation [65]. Stabilization of the proposed center would be accomplished by protein residues in the secondary coordination sphere. Contradicting all the above, the most recent DFT and experimental studies suggest that the pMMO active center is in fact mononuclear [66] [67].

1.5: Synthetic analogues

Synthetic analogues of metalloproteins have been rigorously studied in hopes of better understanding the corresponding biological systems and their functions, as well as to create effective rational catalysts for selective oxidation of alkanes. In the literature there exists a vast amount of research conducted on biomimetic metal complexes featuring the first-row transition metals Mn, Fe, Co, Ni, Cu, and Zn. The complexes synthesized include

predominantly monomers, dimers, and trimers, but several multimetallic complexes are also known. In fact the ability of copper complexes to oxidize phenols and catechols has been known since the 1960's when Grinstead reported copper(II) chloride's ability to convert 3,5-di-tert-butylcatechol to 3,5-di-tert-butyl-o-benzoquinone in methanol [68]. More recent studies emphasize the importance of a short Cu-Cu distance and the nature of the bridging ligand, two factors that promote the deprotonation and coordination of the incoming phenol substrate. This makes the hydroxide, alkoxide, and phenoxide bridging ligands a far superior option, whereas strongly coordinated ligands which cannot be displaced, such as chloride, lead to a catalytically inert compound with respect to phenol/catechol oxidation [69]. Figure 10 shows some of the most active dicopper(II) mimics [70]. The best involved ligands in the mimics presented are those with phenoxide bridges and aromatic imine with high recorded catalytic activities (k_{cat}=1.08−3.24×10^4 h^{-1}).

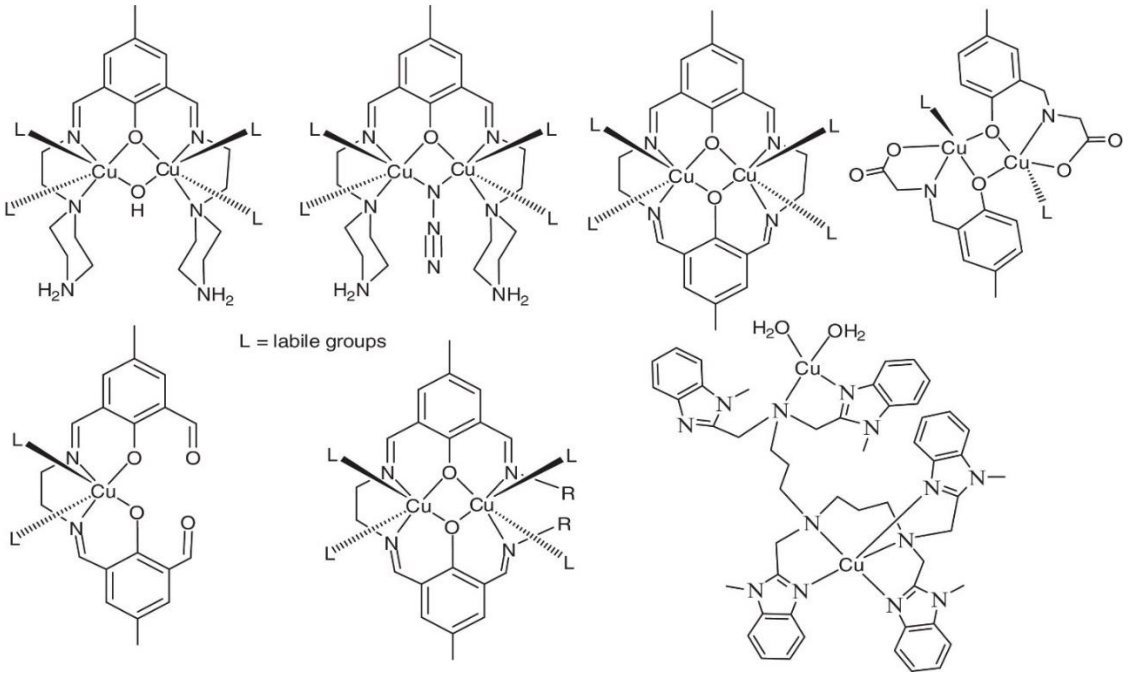

Figure 10. Metal environments of the most active (functional) model copper(II) complexes of catechol oxidase. Adapted from reference [70].

As of yet, dinuclear copper(II) systems show the most promise, however, to this date, besides methane monooxygenase, no other enzymes with diiron or dicopper active sites nor biomimetic synthetic complexes have been capable of oxidizing methane with the same efficiency [71]. A myriad of studies conducted on $[Cu_2O]^{2+}$ cores reached a consensus that these models are not particularly reactive towards methane oxidation [72]. Figure 11 shows the reactive Cu-OH-Cu cores in model copper-enriched zeolite catalysts and complexes. Nonetheless, these studies showed the importance of second-sphere effects on catalysis, particularly with respect to the stabilization of metal centers, access to active sites, and control of substrate binding.

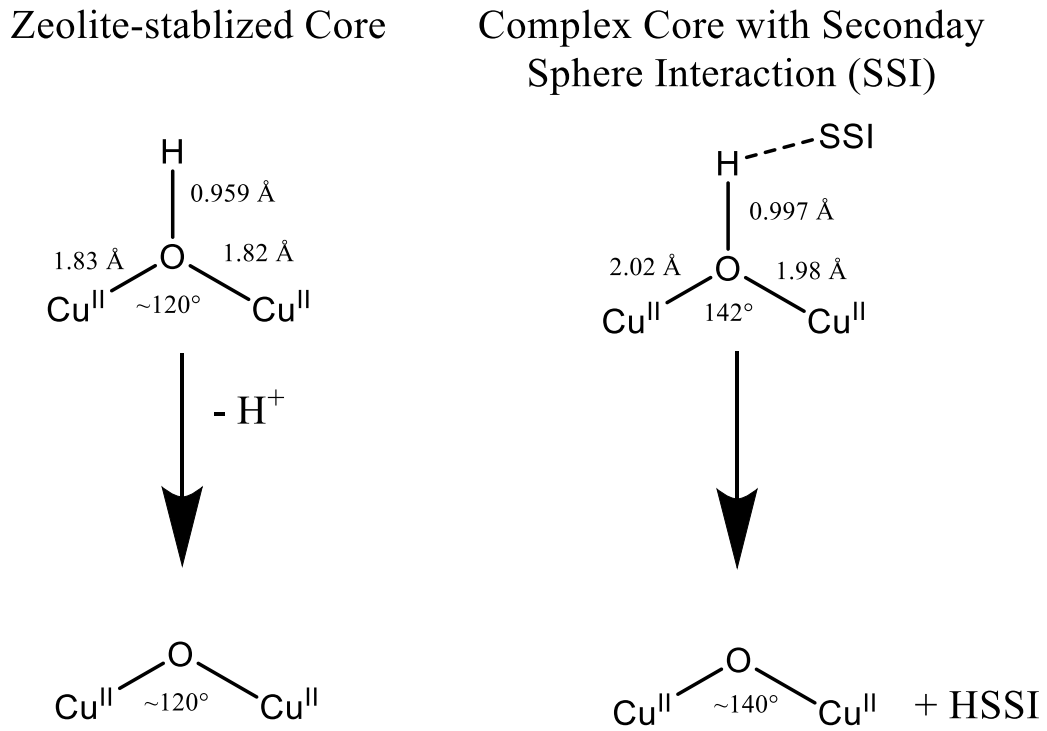

Figure 11. Schematics of Cu−OH−Cu product core in zeolite and in model complexes with secondary sphere interactions. Adapted and modified from reference [72].

Zeolites have been at the forefront of methane oxidation due to their ability to stabilize the reactive $[Cu_2O]^{2+}$ core by pushing the two Cu centers closer together than in solution, as

well as aiding in the hydrogen abstraction step. Tolman and coworkers proposed a model complex for the oxidation of methane, a dinuclear copper(II) hydroxo-bridged species with varying accessible oxidation states ranging from a Cu^{II}_2, to the mixed valent $Cu^{II}Cu^{III}$, and the Cu^{III}_2 species [73]. Figure 12 shows the crystal structure of the complex. The complex contains a relatively short Cu-Cu distance of 2.672(3) Å, Cu-O bond of 1.925(1)/1.92(1), and a Cu-O-Cu bond angle of 89.2°. What is notable of the hydroxo-bridged complex is that the bridging -OH motif is exposed and readily available for catalytic hydrocarbon oxidations. Magnetics and EPR experiments suggest an antiferromagnetically coupled singlet ground state with an isotropic magnetic exchange value of 2J= -11.5 cm^{-1}.

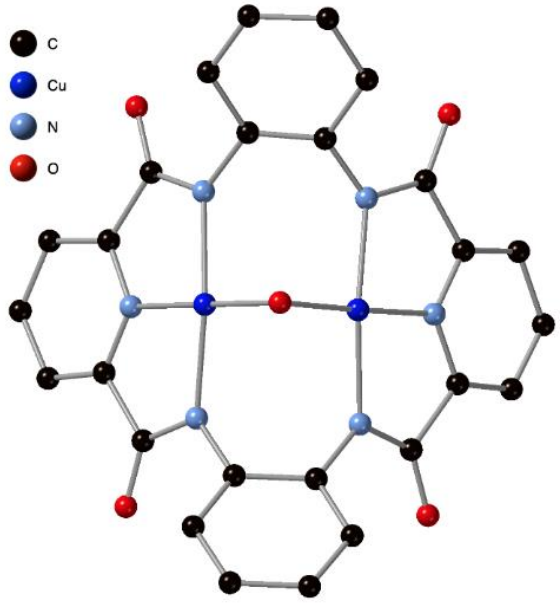

Figure 12. Model Complex for pMMO and oxidation catalysts. Accessible oxidation states: [Cu^{II}_2OH], [$Cu^{II}Cu^{III}$OH], [Cu^{III}_2OH]. Redrawn from reference [73].

Kodera and coworkers on the other hand have reported a dinuclear copper(II) oxo-bridged species for the oxidation of benzene to phenol [74]. The Cu-Cu distance of this complex is a much longer 3.799(1) Å and a more obtuse Cu-O-Cu bond angle of 158.18°. Figure 13 shows the crystal structure of the complex.

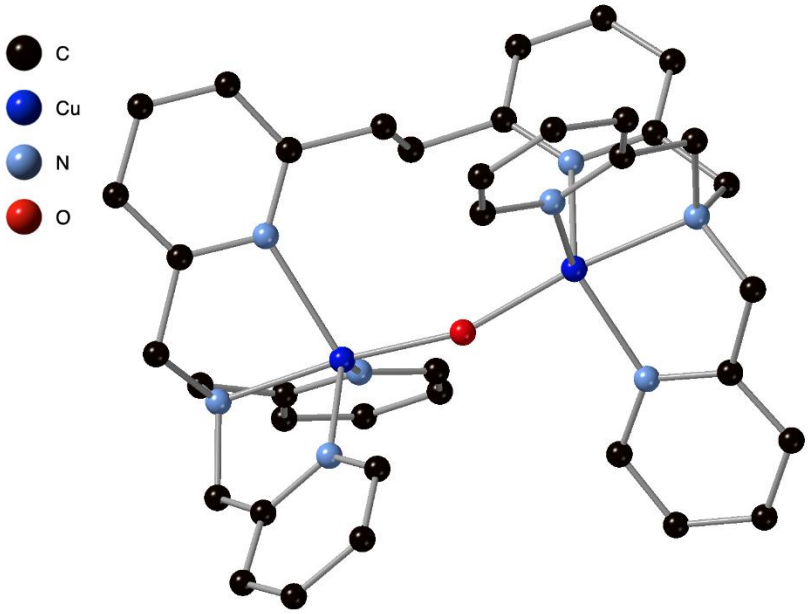

Figure 13. Model complex for the oxidation of benzene to phenol. Redrawn from reference [74].

The model complex boasts impressive experimental TON/TOF for benzene to phenol of 12250 mol^{-1}/1010 h^{-1}. The downside to the complex, however, is the need for H_2O_2, a less favorable reagent than O_2. A literature search conducted for select parameters (Cu-Cu distances, Cu-O distance, Cu-O-Cu angles, J values, $g_{\perp}$, and $g_{\parallel}$) on synthetic oxidation/oxygenation catalysts shows the versatility of copper(II) dinuclear complexes. Table 3 summarizes select parameters for the Cu_2-oxo and -hydroxo synthetic species.

Table 4 summarizes select parameters for biological proteins containing copper(II) dinuclear active sites.

Table 3. Dinuclear Cu-oxo/hydroxo species (**synthetic**).

Entry	Motif	Cu-Cu	Cu-O	Cu-O-Cu	J (cm^{-1})	$g_{\perp}$	$g_{\parallel}$	Reference
1	(μ-OH)	3.628	1.940, 1.940	142.04				[75]
2	(μ-OH)	2.751	1.930, 1.920	90.58	113	2.020	2.210	[76]
3	(μ-OH)	2.842	1.890, 1.890	102.69		2.047	2.296	[77]
4	(μ-OH)	3.651	1.916, 1.918	144.91	-223 (-2J)			[78]
5	(μ-OH)	3.437	1.913, 1.925	131.11	-167 (-2J)			[79]
6	(μ-OH)	3.370	1.899, 1.876	125.74	-149 (-2J)			[80]
7	(μ-OH)	3.645	1.913, 1.874	141.60	-161 (-2J)			[81]
8	(μ-OH)	2.659	1.898, 18.98	89.20				[29]
9	(μ-OH)	2.859	1.914, 1.903	103.52		2.057	2.246	[82]

Table 4. Dinuclear Cu-oxo/hydroxo species ***in proteins.***

Entry	Structure	Cu-Cu (Å)	Cu-O (Å)	Cu-O-Cu	J (cm^{-1})	$g_{\perp}$	$g_{\parallel}$	Refereence
1	Deoxy-TY	4.1	1.885, 1.902	136	<-100 (2J)	2.05	2.21	[83]
2	Cat. Ox	4.4		131				[84]
3	Met-cat.ox	2.9		92				[85]

1.7: Ligands: Pyrazole/pyrazolate

Ligands play a crucial role in the electronic and catalytic properties of biomimetic complexes, formally, ligands can bind to metal centers by donation of lone pair(s) of electrons. Pyrazole ligands tend to be versatile and can bind a variety of metal centers through the nitrogen atom and can be fine-tuned through peripheral substitution. When deprotonated, pyrazolate ions can act as bidentate bridging ligands through the two

nitrogen atoms and further substitution of the 3,5 positions tunes their steric requirements and electron donor properties [86]. Figure 14 shows the accessible binding modes.

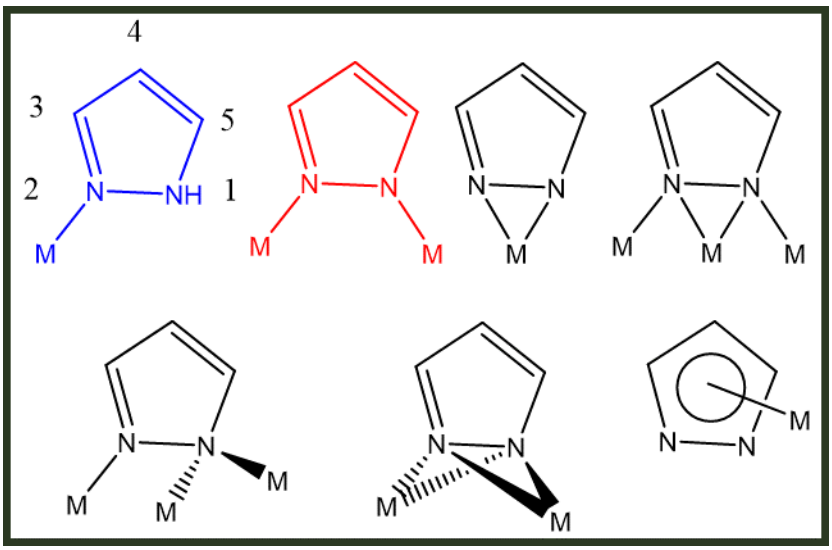

Figure 14. The binding modes accessible by pyrazoles and pyrazolates. The modes highlighted in blue and red represent the most common structural forms.

The versatility of the pyrazole ligands in supporting multicentered complexes stems from their ability to act as anionic bidentate ligands capable of holding two metal atoms in proximity while still allowing for a wide range of intermetallic separation ranging from 2.4-4.6 Å [87].

1.8: Hypothesis: Our approach

Oxo/hydroxo copper(II) dimeric complexes have shown a propensity towards alkane oxidation under the right circumstances (i.e. stabilization via secondary sphere interactions), coupled with the easily accessible redox states (Cu^{0}-Cu^{III}), makes them an attractive system for O-atom chemistry, and as biological protein mimics [88]. Our approach is to employ bulky pyrazole ligands, which can hold two Cu centers in close proximity, while also forcing the formation of a reactive bent-oxo bridge. Reactivity of the

complexes will be moderated by interactions with the secondary coordination sphere; either by hydrogen bonding which can impart partial stability towards the complex, while also being liable enough to not be detrimental, or by interactions with cationic/ionic species (Figure 15) [89]. Current research focuses on creating biomimetic catalysts capable of tackling the oxidation of methane, and while this is indeed a goal of the study, the problem of overoxidation will also be tackled by modifying the chemical and electrical properties of the pyrazole and auxiliary ligands. A key advantage of the pyrazole ligands employed in this study is the ability to force the formation of a bent-oxo bridging ligand without the need for zeolites, which leads to simpler chemistry. Figure 16 shows the overall project goals, where a viable synthetic metalloprotein mimic will be employed to model alkane oxidations as it cycles between the Cu^{II}_2 and Cu^{I}_2 states.

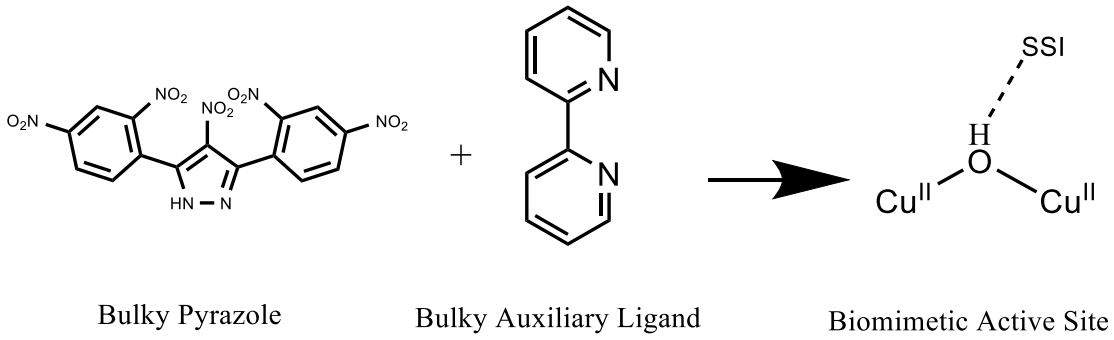

Figure 15. Components of the catalyst used in this study: bulky pyrazole bridges (left), auxiliary chelating bipyridine (center), dinuclear catalyst core (right). SSI = secondary sphere interaction.

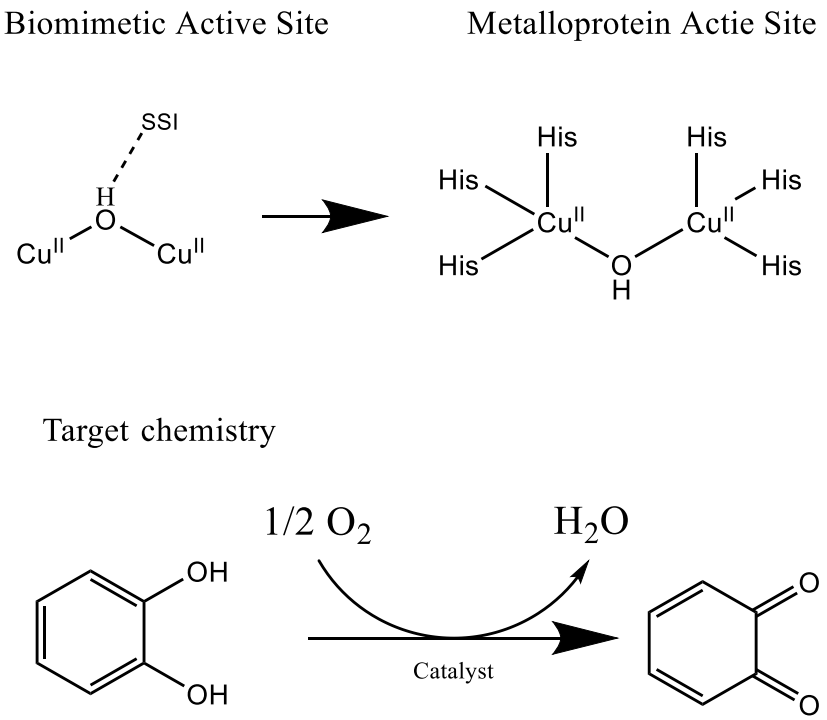

Figure 16. Overview of the goal of this study, to synthesize a viable metalloprotein mimic that can engage in substrate oxidation reactions.

Furthermore, investigation of the reactivity of the dinuclear copper complexes towards alkane oxidation with O_2 as the oxidant will be carried out and monitored by standard characterization methods (GCMS, UV-Vis, NMR), and the redox stability and reactivity via electrochemistry (CV voltammetry). The coordination geometries of the complexes, and secondary sphere environments, of which the importance is now more recognized, will be characterized and studied by SCXRD, as the catalytically active species presented in this work have significant similarities to metalloprotein active centers found in Nature. The project, if successful, will present a novel surrogate method to study the active sites of similar metalloproteins whose reactivity still presents lingering questions, as well as a model for alkane oxidation reactions in more readily accessible conditions.

1.9 Sulfur background and introduction

Most elemental cycles operate in reductive and oxidative modes, typically fueling each other, to which in Nature, sulfur is no exception. Sulfur species play an important role in geochemical processes and flow through the lithosphere, hydrosphere, atmosphere, and biosphere in what is known as the sulfur cycle (Figure 17) through processes such as atmospheric sulfur deposition and sediment runoff to aquatic ecosystems, while also undergoing multiple transformations in the form of oxidations or reductions [90]. The sulfur cycle governs an eight-electron oxidation/reduction system between the most reduced species, hydrogen sulfide (H_2S), to the most oxidized species, sulfate (SO_4^{2-}). Elemental sulfur is the fourteenth most abundant element on Earth; however, the sulfate ion is the second most abundant ion in both in seawater and fresh water sources [91].

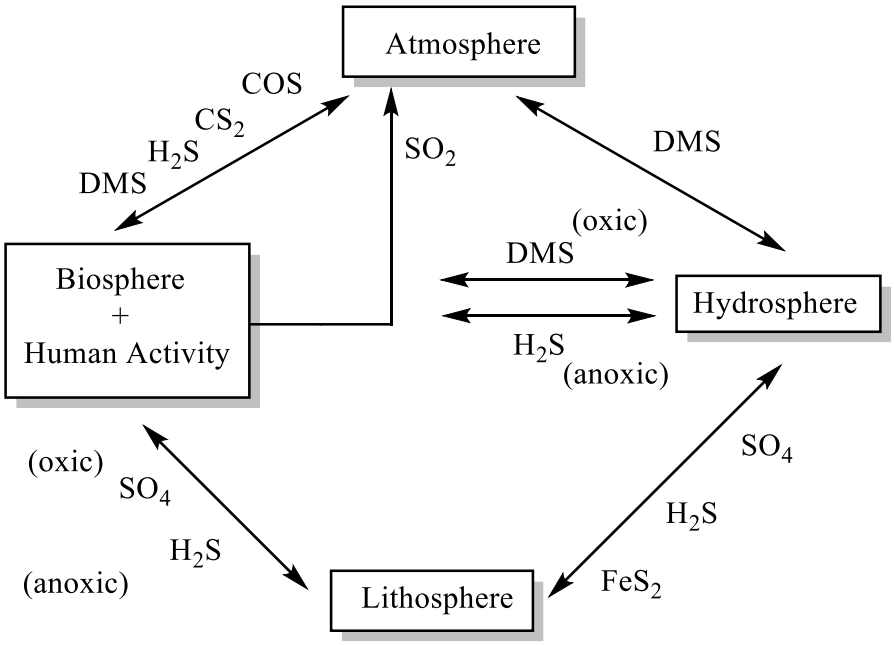

Figure 17. The simplified sulfur cycle shows the four main sources and natural sinks of elemental sulfur and its species. Redrawn from reference [91].

In recent years, anthropogenic sources of sulfur compounds, excavations from the lithosphere and the application of elemental sulfur as an agriculture fertilizer, have significantly affected the sulfur cycle, causing environmental concerns. The main worries stem from the eutrophication and contamination of seawater and freshwater systems, soil degradation, and airborne pollutants such as hydrogen sulfide [92]. The most common forms of sulfur used industrially are obtained as either hydrogen sulfide from natural gas sources or from the various sulfur containing compounds (sulfides, disulfides, mercaptans, etc.) produced from the refinement of crude oil via the hydrodesulfurization process (Figure 18) [93]. In recent years, efforts to develop an inexpensive, recyclable, catalyst for the oxidation of sulfur compounds with activated O_2 at mild temperatures and pressures have increased, as not only will it be commercially lucrative, but also greener for the environment, especially with regards to the petroleum and agricultural industries. This endeavor, however, remains a great challenge for today's researchers as O_2's kinetic stability (triplet ground state) necessitates multiple reductive activation steps [94].

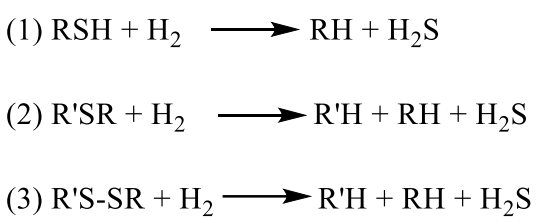

Figure 18. Hydrodesulfurization process for mercaptans (1), sulfides (2), and disulfides (3).

The resulting hydrogen sulfide gas is then further oxidized with O_2 via the Claus process in an industrial furnace (Figure 19). (1) In the Claus process, H_2S is initially converted to sulfur dioxide (SO_2) and water at high temperatures (1000-1200°C); (2) SO_2, in the same furnace, can further react with more H_2S and water, to produce the desired elemental sulfur.

(3) Leftover reactants are funneled further into a catalytic reactor where oxidation via O_2 occurs; typically, 75-98% sulfur recovery is achievable within 3-4 stages [95].

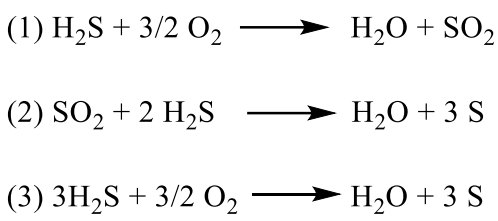

Figure 19. Scheme for the reactions of the Claus process. Reactions 1 and 2 occur in a high temperature furnace, while reaction 3 occurs in a separate catalytic reactor.

The HDS and Claus processes remains relatively inexpensive and well suited for the removal of most sulfur containing compounds found in the petroleum industry, however, refractory sulfur compounds, such as thiophenes and (di)benzothiophenes, are notoriously difficult and expensive to remove, especially the alkylated dibenzothiophenes, with 4-methyldibenzothiophene and 4,6-dimethyldibenzothiophene being the most difficult to be desulfurized. The kinetic stability of these compounds arises from (1) the aromaticity of the compound and (2) the steric hinderances resulting from the nearby alkyl groups near the sulfur atom [96]. Implementation of an effective catalyst that can work in conjunction with an environmentally benign and abundant oxidant, such as O2, would decrease the energy consumption and emissions of the petroleum industry.

1.9.1: H_2S oxidation

Currently, state of the art catalysts, capable of oxidization of H_2S, exist as both homogenous and heterogenous catalysts, with ligands ranging from inorganic chelates to organic ligands [97], [98]. Famously, there exist Fe(III) catalysts capable of H_2S oxidation in solution, with a vast amount of literature existing on the subject [99], [100], [101]. These catalyst function by coordination of HS^- in solution, followed by the generation of a $HS^{\cdot}$

radical as the catalyst is reduced to the Fe(II) state (Scheme 3). $HS^{\cdot}$ can then undergo multiple dimerization and polymerization reactions to produce elemental sulfur, as the catalyst is regenerated by O_2 back to Fe(III) and H_2O_2, the latter of which is suspected of causing catalytic poisoning.

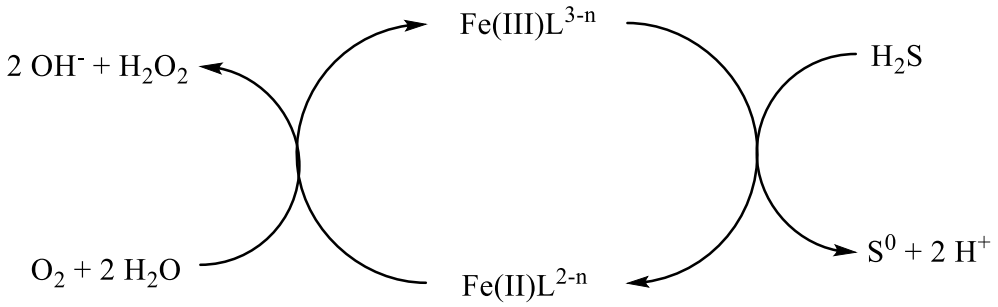

Scheme 3. Scheme for the catalytic oxidation of H_2S to elemental sulfur by a Fe(III) catalyst.

Catalytic poisoning by H_2O_2 occurs via OH radicals reacting with the chelating ligands, leading to ligand decomposition. Current research in this field focuses on the synthesis of a redox couple that is less susceptible to decomposition by reaction products, while maintaining both activity and selectivity towards H_2S. Copper(II) catalysts have also been shown to mediate H_2S oxidation, however, the mechanisms by which this occurs, are not fully understood [102].

1.9.2: Oxidation of Dimethyl Sulfoxide (DMSO) to Me_2SO_2

Research on the catalytic oxidation of dimethyl sulfoxide (DMSO) to the corresponding sulfone, Me_2SO_2, remains scarce, with few kinetic and mechanistic examples in the literature, and even more so with O_2 as the oxidant at ambient temperatures and pressures. Early on, Rao *et al*. proposed a study on an OsO_4 catalyst for the homogenous oxidation of DMSO to Me_2SO_2, however, in this case, O_2 was not the oxidant, instead potassium ferrate

(K_2FeO_4) was used, and required a high pH range of 9.8-11.9 [103]. The study found that DMSO could indeed be oxidized to Me_2SO_2 in a simple two step mechanism with a reaction rate that is first order with regards to Os_2O_4, zeroth order to K_2FeO_4, and fractional order to DMSO (Scheme 4).

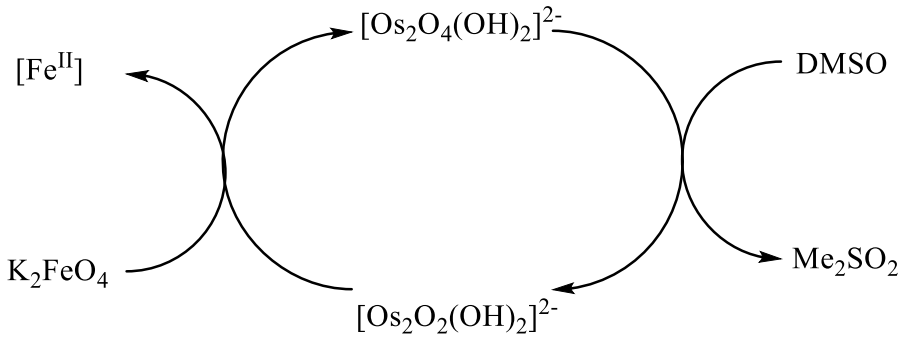

Scheme 4. Catalytic cycle for the oxidation of DMSO to Me_2SO_2 by an Os_2O_4 catalyst as proposed by Rao et al., adapted from reference [103].

In another more recent study, the oxidation of DMSO was investigated by two molybdenum complexes, molybdenum dichloride dioxide (MoO_2Cl_2), and cyclopentenyl molybdenum dioxide chloride ($CpMoO_2Cl$), two complexes known to catalyze the epoxidation of olefins in the presence of peroxide [104]. The catalytic cycle involves an initial associative addition by the terminal oxygen of the peroxide compound to the Mo center, followed by an H shift from the terminal oxygen to the second oxygen of the peroxide to release an alcohol and leave a peroxide group coordinated to the Mo center. A nucleophilic attack by the sulfur in DMSO to one of the activated oxygen atoms of the peroxide group coordinated to the Mo center of the catalyst follows suit and regenerates the complex as DMSO is oxidized to Me_2SO_2 (Scheme 5).

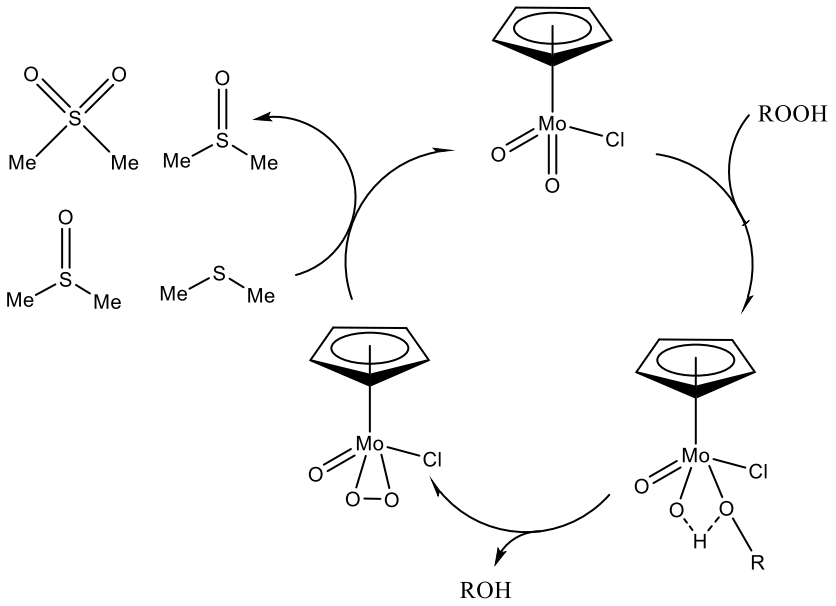

Scheme 5.Catalytic cycle for the sulfoxidation promoted by $CpMoO_2Cl$, propose by Veiros et al., redrawn from reference [104].

With regards to the oxidation of DMSO via oxygen transfer, with O_2 as the oxidant, there exists a study by Sartorel *et al.*, where a ruthenium catalyst was employed [105]. The inspiration for the system is based on metalloenzymes found in Nature, and the system is capable of transferign O^{2-} to DMSO turning it into MSM. The system has also been shown to work at mild temperatures and pressures, in a homogenous solution. In conclusion, most sulfur-oriented chemistry is focused on the conversion of the sulfur-containing compounds that result from the HDS process (mercaptans, sulfides, disulfides, thiophenes, etc.) to H_2S at milder temperatures and pressures. To this end, a catalytic system capable of oxidizing the sulfur-containing pollutants in petroleum with a benign and abundant natural oxidant, such as O_2, would greatly reduce both the environmental impact, and energy costs associated with current methods, which require exorbitant amounts of heat. Further oxidation of H_2S in the Claus process to elemental S would likewise benefit from a greener catalytic system that employs O_2. As for the oxidation of DMSO to Me_2SO_2, far less

literature is available on the subject, with scarce advancements recorded in the past decades, especially through the use of a discrete (non-polymeric) transition metal complex that can employ atmospheric O_2.

1.9.3: Detoxification of S-containing species by redox chemistry.

Besides industrial applications, the redox chemistry of the $R_2S/R_2SO/R_2SO_2$ system is of interest because of the toxicity of R_2SO_2 species in contrast to the non-toxic R_2S and R_2SO. SO_2 is a pollutant that is harmful to both humans and plants, specifically due to its ability to hydrate in water to form sulfite ions (HSO^{3-} and SO_3^{2-}), which, at high concentrations have been associated with plant death [106]. Sulfite in plants can be oxidized to sulfate by the molybdenum cofactor enzyme, sulfite oxidase, through a two-electron reaction which couples the oxidation of sulfite to the reduction of O_2 to H_2O_2. To humans, SO_2 is an eye and skin irritant known to cause severe injury, due to the high amounts of water found in the human body [107]. Tremendous efforts and standards are currently in place to reduce the atmospheric concentration of SO_2 from anthropogenic sources, as it's high solubility in water, and easy conversion to sulfurous and sulfuric acid, contribute to acid rain, and the destruction of various food crops, such as grains [108].

Chapter 2: Copper(II) pyrazole dimers for the oxidation of alkanes

2.1: Introduction

The Raptis research group has focused on the study of metal-pyrazolate complexes for their electrochemical, oxygen transfer, and magnetic properties and applications. Previous work by Dr. Guang Yang, Dr. Logesh Mathivathanan and Susana Herrera in our laboratory led to the synthesis of a dinuclear copper(I) and copper(II) pyrazolate species that switches between the two oxidation states while mediating oxygen transfer. By taking advantage of the nature of the oxo- and hydroxo-bridged copper(II) dimers facilitation of oxygen atom transfer to various substrates including alkanes, mercaptans, and phosphines, has been observed, with the ultimate goal being the oxidation of methane gas. In relevant chemistry, copper hydroxide has been overlooked as a convenient starting material; very few studies employ this copper(II) hydroxide, instead choosing more traditional materials, such as copper(II) chloride, nitrate, and sulfate or copper(I) iodide. Copper(II) hydroxide has the advantage of simultaneously acting as the copper source and as the base, which removes the need for additional base to deprotonate the ligands, (and in turn leads to a greener chemistry reaction). The choice in the transitional metal stems from the readily accessible oxidation states of the metal, ranging from Cu^{0} to Cu^{III}, as well as its ability to produce mixed valent species. Coupled with the abundance of biological enzymes that employ the metal, it makes for a rational choice. The formation of mixed valent species is an interesting aspect of chemistry and while not the focus of this study, it should be kept in mind. Peripheral substitution of the pyrazole ligand can lead to fine-tuning of the complex's electrochemical properties and the formation of hydroxo- or oxo-bridged motifs. The

present study focuses on the bulky substituted pyrazolate ligand, 3,5-diphenyl-1-H-pyrazole and its derivatives, where the complexes that can be produced are wide-ranging. Bidentate chelating ligands, such as 2,2'-bipyridine have so far been the most successful terminal ligands in terms of stabilizing the compound and preventing the formation of copper trimers, or larger oligomers. Copper(II) trimers are not preferable in this study as they tend to form stable μ_3-oxo/hydroxo bridges, which does not suggest applications in catalysis. Furthermore, DFT calculations suggest that dinuclear, bent μ-oxo/hydroxo bridges play an important role in model copper-mediated oxidation/oxygenation chemistry. Instead, the geometry of the [$Cu_3(\mu_3$-O)] moiety is planar with the oxygen being strongly bonded in its all-Cu(II) oxidation state, whereas O-atom transfer occurs upon oxidation to a formally 2-Cu(II)Cu(III) system. As the oxidation of methane is quite cumbersome with a bond dissociation energy of ~104 kcal mol^{-1} and requires a specialized high-pressure steel chamber, the typical research procedure, which is followed in this project, is to start with substrates containing activated C-H bonds, such as 9,10-dihydro-anthracene, with a relatively low bond dissociation energy of ~78 kcal mol^{-1}, establish the catalytic cycle, and advance to substrates with stronger C-H bonds, including toluene, cyclohexane, 2,2,4-trimethylpentane, methylcyclohexane, 3-methylhexane, and finally the natural gases, propane, ethane, methane. The bond dissociation energies are around 87, 100, 103, 105, and 101 kcal mol^{-1} respectively, and ~99 and ~101 kcal mol^{-1} for propane and ethane. Of the above substrates, only toluene and cyclohexane have been investigated with respect to their catalytic oxidation/oxygenation in the present work.

2.2: Experimental

2.2.1: Materials and instrumentation

Copper salts, 2,2'-bipy were obtained from commercial sources and used as received. Pyrazole ligands were synthesized from known methods. Solvents were purified using standard methods. All manipulations were performed open to atmosphere. ^{1}H-NMR spectra were recorded on a 400 Bruker NMR spectrometer and were referenced, FT-IR and UV-Vis spectra were recorded at room temperature with a Perkin Elmer Spectrum 100 FT-IR S and a Varian Cary 3000 spectrometer with quartz cuvettes, or capped quartz cuvettes where specified. Electrochemical experiments were performed with a BAS CV 50 W voltammetric analyzer in 0.1 M $TBAPF_6$/MeCN using a non-aqueous $Ag/AgNO_3$ reference electrode for which the ferricenium/ferrocene couple occurs at 0.426 V, glassy carbon auxiliary 55 electrode, and glassy carbon working electrode. Elemental analyses were performed at Galbraith Laboratories, Inc., Knoxville, Tennessee. The typical characterization progression of the complexes discussed in this work follows a standardized procedure as described by Scheme 6.

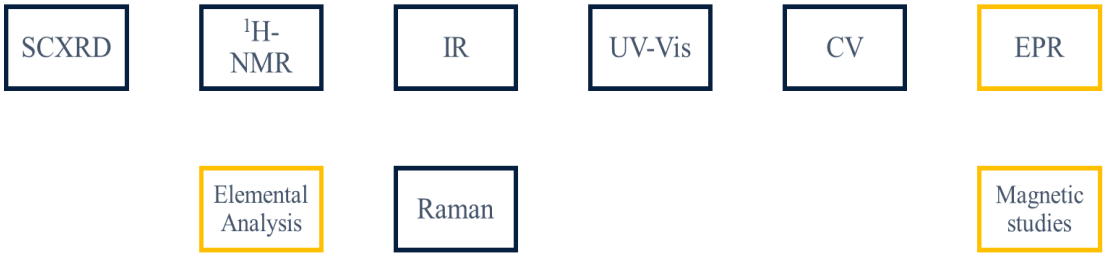

Scheme 6. Typical characterization progression of the complexes in this study. Gold boxes indicate work done by collaborators.

2.2.2: Synthesis

2.2.2.1: Synthesis of pyrazole ligands, PNpzH, 4-X-3,5-Ph2-pzH

PNpzH: A 50 mL round bottom flask is placed in a bed of chilled aluminum beads and charged with 10 mL H_2SO_4, followed by dropwise addition of 5 mL HNO_3, and an additional 5 mL H_2SO_4. 5 g (0.023 mol) 3,5-Ph_2-pzH is then added to the solution and the mixture is refluxed at 110° C for 48 h. The product is crashed out and neutralized of acid with distilled, chilled H_2O, and the precipitate collected via vacuum filtration and dried overnight in a desiccator. Recrystallization of the product is accomplished via slow evaporation acetone. Crystals of the ligand are afforded within a week, purified with Et_2O, and dried under vacuum. Yield 10.75 g, 93%. Elemental analysis shows experimental/calculated values of C 43.40/44.02; H 2.31/3.11; N 19.80/18.91.

4-Cl-3,5-Ph_2-pzH: A 50 mL round bottom flask is placed in a bed of aluminum beads and charged with 25 mL distilled H_2O and brought up to 60° C. Under stirring, 5 g (0.023 mol) 3,5-Ph_2-pzH, and 8.2 g (0.046 mol) N-chlorosuccinimide are added and refluxed for 24 h. The resulting precipitate is collected via vacuum filtration, washed with Et_2O, and dried under vacuum. Recrystallization of the product is achieved via slow evaporation of DCM. Crystals of the ligand are afforded within

a week, purified with Et_2O, and dried under vacuum. Yield: 4.62 g, 78%.

4-Br-3,5-Ph_2-pzH: A 50 mL round bottom flask is placed in a bed of aluminum beads and charged with 25 mL distilled H_2O and brought up to 40° C. Under stirring, 5 g (0.023 mol) 3,5-Ph_2-pzH, and 4.1 g (0.023 mol) N-bromosuccinimide are added and refluxed for 24 h. The resulting precipitate is collected via vacuum filtration, washed with Et_2O, and dried under vacuum. Recrystallization of the product is achieved via slow evaporation of DCM. Crystals of the ligand are afforded within a week, purified with Et_2O, and dried under vacuum. Yield: 6.0 g, 88%.

2.2.2.2: Synthesis of $[Cu^{I}_2(\mu\text{-PNpz})_2(MeCN)_2]$ (1)

Method A: A 20 mL scintillation vial is charged with 37.86 mg (0.20 mmol) CuI and 100 mg (0.20 mmol) PNpzH and dissolved, under stirring, in 5 mL MeCN. To the solution, 40 μL (0.398 mmol) Et_3N is added dropwise, and the mixture was stirred for 24 h. The reaction mixture was filtered through celite and glass wool to remove unreacted material, and the filtrate set to slow evaporate. deep red crystals were obtained within one week. Yield: 170.75 mg, 80%. Chemical formula, $C_{34}H_{18}Cu_2N_{16}O_{20}$; molecular weight, 1097.70 g/mol.

2.2.2.3: Synthesis of $[Cu^{I}_2(\mu\text{-PNpz})_2(bipy)_2]$ (2)

Method A: A 20 mL scintillation vial is charged with 75.70 mg (0.398 mmol) CuI, 200 mg (0.398 mmol) PNpzH, and 62.20 mg (0.398 mmol) 2,2'-bipy and dissolved, under stirring, in 5 mL MeCN. To the solution, 80 mL (0.796 mmol) Et_3N in 2 mL MeOH is added dropwise, and the mixture was stirred for 24 h. The reaction mixture was filtered through celite and glass wool to remove unreacted material, and the filtrate set to slow evaporate. deep red crystals were obtained within one week. Yield: 332.40 mg, 60%. Chemical formula, $C_{52}H_{36}Cu_2N_{18}O_{22}$; molecular weight, 1392.04 g/mol. Elemental analysis ($C_{50}H_{28}Cu_2N_{18}O_{20}$ with 6 H_2O in lattice; $C_{50}H_{40}Cu_2N_{18}O_{26}$), shows experimental/calculated values of C 42.71/42.78; H 2.26/2.76; N 17.82/17.27.

2.2.2.4: Synthesis of $[Cu^{II}_2(\mu\text{-}DMSO_2)(\mu\text{-PNpz})_2(bipy)_2]$ (3)

Method A: Red crystals of complex **2** were dissolved in 5 mL DMSO and the initially red solution slowly turned to a dark green over the course of 48 h.

Method B: A 20 mL scintillation vial is charged with 9.6 mg (0.10 mmol) $Cu(OH)_2$, 50 mg (0.10 mmol) PNpzH, 15.6 mg (0.10 mmol) 2,2'-bipy and dissolved, under stirring, in 5 mL MeOH. To the solution, 50 μL of DMSO is added dropwise, and the mixture was stirred for 24 h. The reaction mixture was filtered through celite and glass wool

to remove unreacted material, and the filtrate is set to slow diffuse in an Et_2O chamber. deep green crystals were obtained within two weeks. Yield: 35.55 mg, 25%. Chemical formula, $C_{52}H_{34}Cu_2N_{18}O_{22}S$; molecular weight, 1422.11 g/mol. Elemental analysis ($C_{52}H_{34}Cu_2N_{18}O_{22}S$), shows experimental/calculated values of C 44.89/43.92; H 2.34/2.41; N 18.00/17.73.

2.2.2.5: Synthesis of $[Cu_2(\mu\text{-PNpz})_3(C_7H_5O_2)_2]$ (4)

Method A: A 20 mL scintillation vial is charged with 139.204 (0.10 mmol) Complex **2**, 50 mg (0.10 mmol) PNpzH, 30.58 mg (0.10 mmol) $Cu(PhCO_2)_2$, and 10 μL (0.10 mmol) Et_3N, under stirring, in 5 mL MeCN. The mixture was stirred for 24 h and filtered through celite and glass wool to remove unreacted material, and the filtrate is placed in a 50 mL round bottom flask where the MeCN solvent is removed via rotary evaporation. The green powder is dissolved in DCM, and set to crystallize via layering of toluene/DCM. Turquoise flower crystals suitable for SCXRD were obtained within weeks. Yield: 42.5 mg, 25%. Chemical formula, $C_{59}H_{28}Cu_2N_{21}O_{34}$; molecular weight, 1702.06 g/mol. Elemental analysis was not conducted on this sample.

2.2.2.6: Synthesis of $[Cu^{II}_2(\mu\text{-4-Br-3,5-Ph}_2\text{-pz})_2(4\text{-Br-Ph}_2\text{-pz})_2(bipy)_2]$ (5)

Method A: A 20 mL scintillation vial is charged with 65.48 mg (0.67 mmol) $Cu(OH)_2$, 200 mg (0.67 mmol) 4-Br-3,5-Ph_2-pzH, and 104.5 mg

(0.67 mmol) 2.2'-bipy, under stirring, in 5 mL MeCN. The mixture was stirred for 24 h at rt, where it goes from a light blue color to a light green color and is filtered through celite and glass wool to remove unreacted material, and the filtrate is set to crystallize by slow diffusion in an Et_2O chamber. Translucent green crystals are obtained within a week. Yield: 17.80 mg, 30%. Chemical formula, $C_{80}H_{56}Br_4Cu_2N_{12}$; molecular weight, 1632.12 g/mol. Elemental analysis ($C_{80}H_{56}Br_4Cu_2N_{12}$), shows experimental/calculated values of C 58.16/58.87; H 4.03/3.46; N 9.40/10.30.

2.2.2.7: Synthesis of $[Cu^{II}_2(\mu\text{-}OH)(\mu\text{-}4\text{-}Cl\text{-}3,5\text{-}Ph_2\text{-}pz)_2(bipy)_2]I$ (6)

Method A: A 20 mL scintillation vial is charged with 73.80 mg (0.38 mmol) CuI, 100 mg (0.38 mmol) 4-Cl-3,5-Ph_2-pzH, and 60.0 mg 2.2'-bipy, and dissolved under stirring, in 5 mL MeCN/DCM. 38 μL (0.38 mmol) Et_3N is slowly pipetted, and the mixture was stirred for 24 h at rt, where it goes from a light blue color to a light green color and is filtered through celite and glass wool to remove unreacted material, and the filtrate is set to crystallize by slow diffusion in an Et_2O chamber. Light green crystals are obtained within a week. Yield: 240 mg, 60%. Chemical formula, $C_{50}H_{37}Cl_2Cu_2IN_8O$; molecular weight, 1090.78 g/mol. Elemental analysis ($C_{50}H_{37}Cl_2Cu_2IN_8O$), shows experimental/calculated values of C 53.89/55.06; H 3.40/3.42; N 9.57/10.37.

2.2.2.8: Synthesis: $[Cu^{II}_2(\mu\text{-}OMe)(\mu\text{-}4\text{-}Cl\text{-}3,5\text{-}Ph_2\text{-}pz)_2(bipy)_2].(4\text{-}Cl\text{-}3,5\text{-}Ph_2\text{-}pz)(MeOH)$ (7)

Method A: A 20 mL scintillation vial is charged with 37.80 mg (0.38mmol) $Cu(OH)_2$, 100 mg (0.38mmol) 4-Cl-3,5-Ph_2-pzH, and 60.0 mg (0.38mmol) 2.2'-bipy, and dissolved under stirring, in 5 mL DCM/MeOH. The mixture was stirred for 24 h at rt, where it goes from a cloudy blue color to an intense green color, and finally settles as a deep green color. The mixture is filtered through celite and glass wool to remove unreacted material, and the filtrate is set to crystallize by slow diffusion in an Et_2O chamber. Light green crystals are obtained within a week. Yield: 217.27 mg, 50%. Chemical formula, $C_{57}H_{53}Cl_3Cu_2N_{10}O_2$; molecular weight, 1143.56 g/mol. Elemental analysis was not submitted for this samples.

2.2.2.9: Synthesis: $[Cu^{II}_2(\mu\text{-}OMe)(\mu\text{-}I)(\mu\text{-}4\text{-}Cl\text{-}3,5\text{-}Ph_2\text{-}pz)(bipy)_2]I_3$ (8)

Method A: A 20 mL scintillation vial is charged with 144.70 mg (0.76 mmol) CuI, 100 mg (0.38 mmol) 4-Cl-3,5-Ph_2-pzH, and 60.0 mg (0.38 mmol) 2.2'-bipy, and dissolved under stirring, in 5 mL DCM/MeOH. The mixture was stirred for 24 h at rt, where it goes from a deep red color to an intense deep green color. The mixture is filtered through celite and glass wool to remove unreacted material, and the filtrate is set to crystallize by slow diffusion in an Et_2O chamber. Green crystals are obtained within a week. Yield: 117.0 mg, 25%. Chemical formula, $C_{36}H_{29}ClCu_2I_4N_6O$; molecular weight,

1231.82 g/mol. Elemental analysis was not submitted for this samples.

2.2.2.10: Synthesis of $[Cu^{II}_2(\mu\text{-}OH)(\mu\text{-}PNpz)_2(bipy)_2](PNpz)$ (9)

Method A. Red crystals of complex **2** were dissolved in 5 mL MeCN and layered over H_2O for recrystallization, the dark red solution changes to a light green color, and green crystals were collected for SXCRD within a week.

Method B: A 20 mL scintillation vial is charged with 25.60 mg (0.262 mmol) $Cu(OH)_2$, 200 mg (0.398 mmol) PNpzH, and 40.0 mg (0.262 mmol) 2,2'-bipy and dissolved, under stirring, in 5 mL MeCN. The mixture was stirred for 24 h at rt and filtered through celite and glass wool to remove unreacted material, and the filtrate is set to crystallize by layering of MeCN/H_2O. Deep green, X-ray quality crystals were obtained within a week. Yield: 230 mg, 50%. Chemical formula, $C_{65}H_{35}Cu_2N_{25}O_{31}$; molecular weight, 1789.23 g/mol. Elemental analysis ($C_{65}H_{35}Cu_2N_{25}O_{31}$), shows experimental/calculated values of C 43.47/43.63; H 1.89/1.97; N 19.20/19.57. A second monomeric complex crystallizes alongside the desired product and are removed by washing with MeOH (*vide infra*).

2.2.2.11: Synthesis of $[Cu^{II}(OH_2)(PNpz)_2(bipy)].H_2O$ (10)

Method A: A 20 mL scintillation vial is charged with 4.8 mg (0.05 mmol) $Cu(OH)_2$, 50 mg (0.10 mmol) PNpzH, and 7.8 mg (0.05 mmol) 2,2'-

bipy, under stirring, in 5 mL MeCN. The mixture was stirred for 24 h at rt and filtered through celite and glass wool to remove unreacted material, and the filtrate is set to crystallize by layering of MeCN/H_2O. The resulting deep blue crystals are dissolved in MeOH and recrystallized via slow evaporation. Yield: 17.80 mg, 30%. Chemical formula, $C_{42}H_{27}CuN_{17}O_{22}$; molecular weight, 1185.34 g/mol. Elemental analysis ($C_{42}H_{27}CuN_{17}O_{22}$), shows experimental/calculated values of C 42.62/42.56; H 2.28/2.30; N 20.44/20/09.

2.2.3 Crystal structure

2.2.3.1 Crystal structure solution and refinement

X-ray diffraction data were obtained from single crystals mounted atop a glass fiber or on a Mitegen® Cryoloop® with Paratone® oil. Data were collected using Bruker D8 Quest diffractometer with Bruker PHOTON II CMOS-based detector with graphite-monochromated Mo-Kα radiation (λ = 0.71073 Å). Frames were integrated with the Bruker APEX III software package using a narrow-frame algorithm. Absorption effects were corrected using the multi-scan method (SADABS). Structures were solved by intrinsic or direct methods with ShelXT or SHELXS and refined with ShelXL using full-matrix least-squares minimization on the Olex2 program [109]. All non-hydrogen atoms were refined anisotropically, Hydrogen atoms positions were calculated using the riding model. Disordered interstitial solvents, where present, were treated with PLATON SQUEEZE.

2.2.3.2 Crystal structure data tables

*Table 5. Structure refinement parameters for complexes **1-3**.*

Identification code	**1**	**2**	**3**
Empirical formula	$C_{34}H_{18}Cu_2N_{16}O_{20}$	$C_{51}H_{44}Cu_2N_{18}O_{21}$	$C_{52}H_{34}Cu_2N_{18}O_{22}S$
Formula weight	1097.72	1372.12	1422.11
Temperature/K	299(2)	300(2)	273.15
Crystal system	monoclinic	orthorhombic	monoclinic
Space group	$P2_1/c$	$Pccn$	$C2/c$
a/Å	14.4825(8)	18.636(3)	31.940(4)
b/Å	9.9168(5)	21.175(3)	20.535(2)
c/Å	14.6200(8)	15.376(2)	18.924(2)
α/°	90.00	90.00	90
β/°	97.482(2)	90.00	98.161(2)
γ/°	90.00	90.00	90
Volume/Å^3	2081.85(19)	6067.5(15)	12286(3)
Z	2	4	8
ρ_{calc}g/cm^3	1.751	1.502	1.538
μ/mm^{-1}	1.126	0.792	0.819
F(000)	1104.0	2808.0	5776.0
Crystal size/mm^3	0.13 × 0.06 × 0.03	0.16 × 0.13 × 0.1	0.251 × 0.224 × 0.213
Radiation	MoKα (λ = 0.71073)	MoKα (λ = 0.71073)	MoKα (λ = 0.71073)
2Θ range for data collection/°	5.9 to 52.92	5.74 to 53.04	4.73 to 50.34
Index ranges	-18 ≤ h ≤ 18, -12 ≤ k ≤ 12, -18 ≤ l ≤ 18	-23 ≤ h ≤ 23, -26 ≤ k ≤ 26, -19 ≤ l ≤ 19	-38 ≤ h ≤ 37, -24 ≤ k ≤ 24, -22 ≤ l ≤ 22
Reflections collected	59318	71062	55069
Independent reflections	4280 [R_{int} = 0.0938, R_{sigma} = 0.0449]	6263 [R_{int} = 0.1673, R_{sigma} = 0.0810]	10929 [R_{int} = 0.0810, R_{sigma} = 0.0667]
Data/restraints/parameters	4280/60/326	6263/2/424	10929/9/857
Goodness-of-fit on F^2	1.070	1.032	1.463
Final R indexes [I>=2σ (I)]	R_1 = 0.0575, wR_2 = 0.1472	R_1 = 0.0745, wR_2 = 0.2179	R_1 = 0.1563, wR_2 = 0.3894
Final R indexes [all data]	R_1 = 0.1027, wR_2 = 0.1716	R_1 = 0.1520, wR_2 = 0.2596	R_1 = 0.2443, wR_2 = 0.4848
Largest diff. peak/hole / e Å^{-3}	0.73/-0.47	1.09/-0.40	3.27/-0.87

*Table 6. Structure refinement parameters for complexes **4**-**6**.*

Identification code	**4**	**5**	**6**
Empirical formula	$C_{59}H_{30}Cu_2N_{21}O_{34}$	$C_{80}H_{56}Br_4Cu_2N_{12}$	$C_{50}H_{37}Cl_2Cu_2I_{1.5}N_8O$
Formula weight	1704.12	1632.08	1154.20
Temperature/K	273.15	296.69	273.15
Crystal system	monoclinic	monoclinic	monoclinic
Space group	*C2/c*	$P2_1/n$	*C2/c*
a/Å	27.193(6)	14.9399(7)	24.554(5)
b/Å	15.520(3)	15.9163(8)	33.841(8)
c/Å	20.888(5)	17.2745(9)	14.128(3)
α/°	90	90	90
β/°	107.684(5)	105.1970(10)	101.516(6)
γ/°	90	90	90
Volume/Å^3	8399(3)	3964.0(3)	11503(4)
Z	4	2	8
ρ_{calc}g/cm^3	1.348	1.367	1.333
μ/mm^{-1}	0.599	2.601	1.676
F(000)	3444.0	1636.0	4580.0
Crystal size/mm^3	0.151 × 0.142 × 0.051	0.309 × 0.219 × 0.096	0.363 × 0.35 × 0.319
Radiation	MoKα (λ = 0.71073)	MoKα (λ = 0.71073)	MoKα (λ = 0.71073)
2Θ range for data collection/°	4.712 to 49.48	5.848 to 52.862	4.814 to 50.186
Index ranges	-31 ≤ h ≤ 31, -18 ≤ k ≤ 17, -24 ≤ l ≤ 24	-18 ≤ h ≤ 18, -19 ≤ k ≤ 19, -21 ≤ l ≤ 21	-28 ≤ h ≤ 29, -40 ≤ k ≤ 40, -16 ≤ l ≤ 16
Reflections collected	28101	77129	51074
Independent reflections	7105 [R_{int} = 0.0918, R_{sigma} = 0.0920]	8148 [R_{int} = 0.0369, R_{sigma} = 0.0210]	10183 [R_{int} = 0.0626, R_{sigma} = 0.0600]
Data/restraints/parameters	7105/0/512	8148/0/442	10183/0/582
Goodness-of-fit on F^2	1.086	1.020	1.332
Final R indexes [I>=2σ (I)]	R_1 = 0.1251, wR_2 = 0.3340	R_1 = 0.0373, wR_2 = 0.0878	R_1 = 0.1201, wR_2 = 0.3373
Final R indexes [all data]	R_1 = 0.2281, wR_2 = 0.4292	R_1 = 0.0533, wR_2 = 0.0982	R_1 = 0.1679, wR_2 = 0.3872
Largest diff. peak/hole / e Å^{-3}	1.29/-0.69	0.86/-0.60	2.08/-2.17

*Table 7. Structure refinement parameters for complexes **7**-**8**.*

Identification code	**7**	**8**
Empirical formula	$C_{67}H_{53}Cl_3Cu_2N_{10}O_2$	$C_{18}H_{14.5}Cl_{0.5}CuI_2N_3O_{0.5}$
Formula weight	1263.62	615.89
Temperature/K	273.15	273.15
Crystal system	triclinic	orthorhombic
Space group	*P*-1	*Pnma*
a/Å	14.3459(3)	8.6711(11)
b/Å	15.1833(3)	16.528(2)
c/Å	16.3588(4)	27.587(3)
α/°	116.9220(10)	90
β/°	94.0350(10)	90
γ/°	107.9520(10)	90
Volume/Å^3	2928.37(11)	3953.6(8)
Z	2	8
ρ_{calc}g/cm^3	1.433	2.069
μ/mm^{-1}	0.919	4.304
F(000)	1300.0	2328.0
Crystal size/mm^3	0.459 × 0.083 × 0.057	0.185 × 0.169 × 0.059
Radiation	MoKα (λ = 0.71073)	MoKα (λ = 0.71073)
2Θ range for data collection/°	5.006 to 50.06	4.924 to 52.696
Index ranges	-17 ≤ h ≤ 17, -18 ≤ k ≤ 18, -19 ≤ l ≤ 19	-10 ≤ h ≤ 10, -20 ≤ k ≤ 20, -34 ≤ l ≤ 34
Reflections collected	58691	46872
Independent reflections	10323 [R_{int} = 0.0293, R_{sigma} = 0.0220]	4172 [R_{int} = 0.0347, R_{sigma} = 0.0153]
Data/restraints/parameters	10323/0/759	4172/0/239
Goodness-of-fit on F^2	1.070	1.153
Final R indexes [I>=2σ (I)]	R_1 = 0.0367, wR_2 = 0.0828	R_1 = 0.0376, wR_2 = 0.0824
Final R indexes [all data]	R_1 = 0.0448, wR_2 = 0.0861	R_1 = 0.0488, wR_2 = 0.0926
Largest diff. peak/hole / e Å^{-3}	0.35/-0.41	1.31/-1.06

*Table 8. Structure refinement parameters for complexes **9-10**.*

Identification code	**9**	**10**
Empirical formula	$C_{65}H_{37}Cu_2N_{25}O_{32}$	$C_{42}H_{27}CuN_{17}O_{22}$
Formula weight	1807.27	1185.34
Temperature/K	273.15	233.15
Crystal system	triclinic	triclinic
Space group	*P*-1	*P*-1
a/Å	16.480(6)	12.6690(4)
b/Å	16.668(6)	14.1098(5)
c/Å	22.481(8)	14.6712(4)
α/°	76.090(9)	94.424(3)
β/°	74.621(9)	91.343(2)
γ/°	69.582(9)	105.558(3)
Volume/Å^3	5505(3)	2516.30(14)
Z	2	2
ρ_{calc}g/cm^3	1.090	1.564
μ/mm^{-1}	0.460	0.535
F(000)	1832.0	1206.0
Crystal size/mm^3	0.552 × 0.332 × 0.252	? × ? × ?
Radiation	MoKα (λ = 0.71073)	MoKα (λ = 0.71073)
2Θ range for data collection/°	5.64 to 53.078	4.252 to 61.284
Index ranges	-20 ≤ h ≤ 20, -20 ≤ k ≤ 20, -28 ≤ l ≤ 28	-17 ≤ h ≤ 18, -20 ≤ k ≤ 20, -20 ≤ l ≤ 20
Reflections collected	125088	45807
Independent reflections	22602 [R_{int} = 0.0576, R_{sigma} = 0.0614]	14590 [R_{int} = 0.0656, R_{sigma} = 0.0971]
Data/restraints/parameters	22602/90/1124	14590/4/749
Goodness-of-fit on F^2	1.042	0.999
Final R indexes [I>=2σ (I)]	R_1 = 0.0534, wR_2 = 0.1427	R_1 = 0.0806, wR_2 = 0.2153
Final R indexes [all data]	R_1 = 0.1016, wR_2 = 0.1611	R_1 = 0.1535, wR_2 = 0.2501
Largest diff. peak/hole / e Å^{-3}	0.38/-0.34	1.38/-0.63

2.3 Results and discussion

The study conducted has shown the ability of bulky substituted pyrazoles to stabilize a variety of copper dimers with different bridging motifs, μ-O, μ-OH, μ-OMe, etc., and oxidation states, Cu^{I} and Cu^{II}. The plasticity of copper is evident by the large number of complexes that can be produced by simply varying the copper source and the solvent system, a characteristic that is highly desirable in catalytic oxidations.

2.3.1 Structural characterization

2.3.1.1 Pyrazole ligands

While pyrazole ligands tend to coordinate in monodentate fashion, once deprotonated by a base (OH^-, Et_3N in the present study), they typically bind in bidentate mode. This strategy allows the expansion of the nuclearity of the complexes it binds to form dinuclear, trinuclear, etc. For the scope of this project, dimers are of interest due to their ability to form oxygen bridges with bent geometry. Further substitution via electron withdrawing/donating substituents on the pyrazole ligands enables the fine-tuning of the redox and spectroscopic properties of the products. The choice of bulky peripheral ligands in the complexes stems from their ability to prevent the formation of trimers due to steric hindrance and push the formation of dimers (Figure 20). Pyrazolato compounds of Cu(I) are mostly trinuclear, where Cu ions have a linear coordination geometry and the pyrazolato ligands are (approximately) coplanar [110]. In this work, however, the presence of bulky dinitrophenyl substituents at the 3 and 5-positions sterically prevents the formation of triangular Cu-pyrazolato rings. This is however, not the first time it has been observed, dinculear compounds have been reported containing chelating groups at the 3-

and 5- positions [111]. In the present case, such chelating ligands are absent. 2,2'-bipy was used instead as an auxiliary ligand.

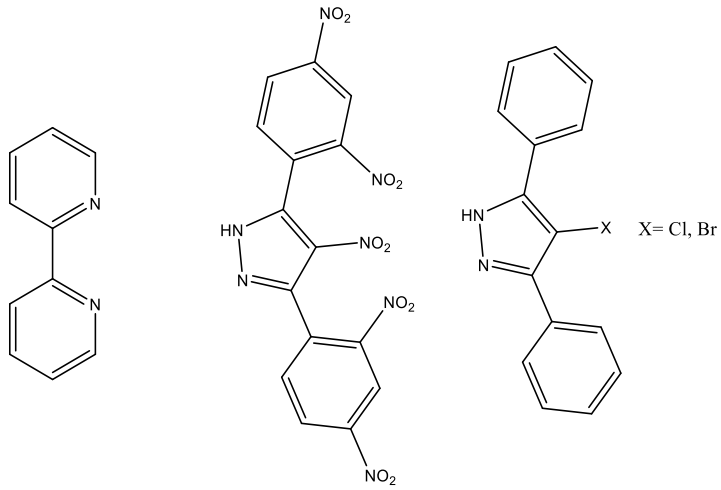

Figure 20. Bulky ligands of interest: 2,2'-bipy, PNpzH and 4-X-3,5-Ph_2-pzH.

The versatility of pyrazole ligands allows the fine tuning of the electronic properties of the complexes synthesized, to this end the substitution of more/less electronic withdrawing groups and the effects on the structural and electronic properties of the complexes can be mapped out. 3,5-Bis(2,4- dinitrophenyl)-4-nitro-1-H-pyrazole.acetonemonosolvate, $C_{15}H_7N_7O_{10}.C_3H_6O$, PNpzH·O=C$(CH_3)_2$ was prepared by a reported procedure [112]. The halogenation of 3,5-diphenyl-pyrazole to produce 4-X-3,5-Ph_2-pyrazole, 4-X-pzH (X= Cl, Br), was investigated and a variety of copper(II) containing dinuclear complexes were produced and characterized. The ligand 4-chloro-3,5-Ph_2-pyrazole (4-Cl-3,5-Ph_2-pzH) and 4-Br-3,5-Ph_2-pyrazole (4-Br-3,5-Ph_2-pzH) were prepared using a known synthesis by Zhao *et al.*, using 3,5-diphenyl-pyrazole and water [113]. Product yields were over 90%; this made the synthesis of chloro- and bromo- halogenated pyrazoles viable, as well as the PNpzH ligand (Scheme 7). Motifs ranging from μ-OH, μ-O, μ-OMe, and μ-(O_2SMe_2) were obtained and studied. Figure A. 1 shows the FTIR spectrum of the PNpzH ligand.

(**1**)

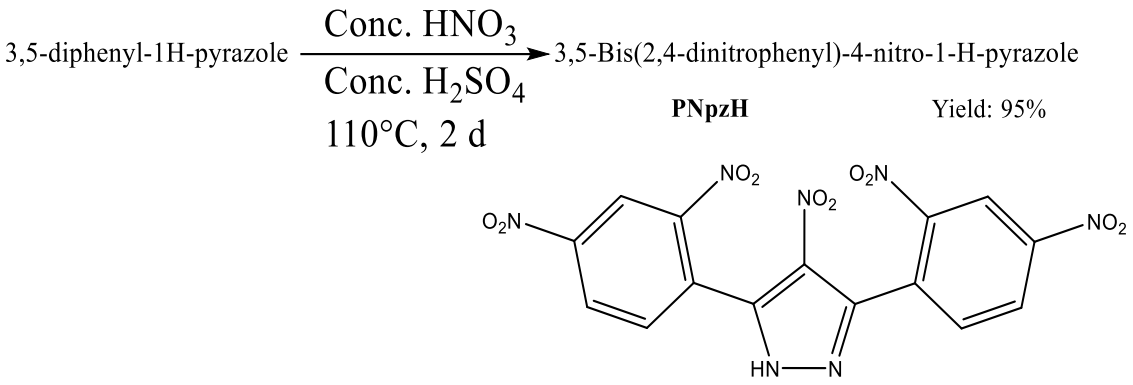

(**2**)

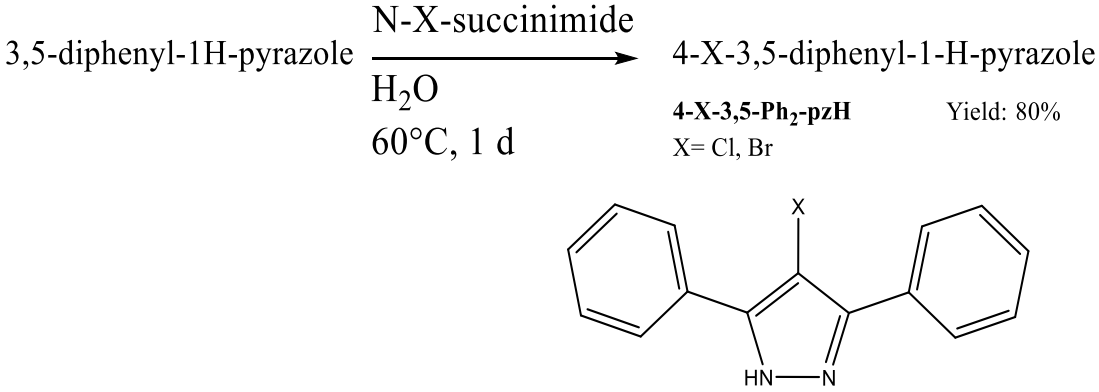

Scheme 7. Reaction conditions for the synthesis of (1) PNpzH and (2) 4-X-3,5-Ph$_2$-pzH. Synthetic procedures adapted from references [112] and [113].

2.3.1.2: Copper(I) dimers: Complexes 1, 2.

Complex **1** can be synthesized from the bulky pyrazole, PNpzH, which prevents the formation of higher nuclearity structures, however, unlike complex **2**, without the addition of an auxiliary neutral ligand, the complex is capped by solvent molecules which are easily displaced with incoming ligands, such as in the case of complex **2**. **1**, while unremarkable on its own, can be used as a starting material to produce the more valuable complex **2**, which can undergo oxidation to various Cu^{II} species. Scheme 8 shows the synthetic procedure for complex **1** and Figure 21 the line drawing. Scheme 9 shows the

synthetic procedure for complex **2**, Figure 43 the red crystals of **2** under the microscope, and Figure 22 shows the line drawing of the complex.

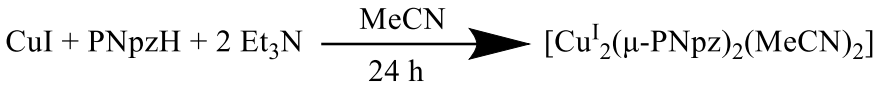

*Scheme 8. Reaction conditions for the synthesis of complex **1**.*

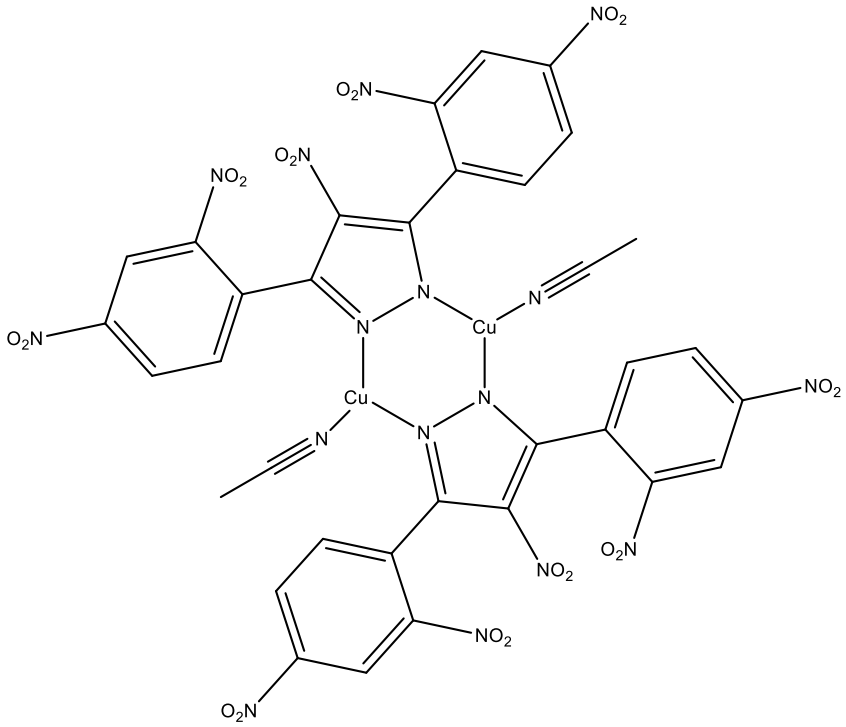

*Figure 21. Line drawing of complex **1**.*

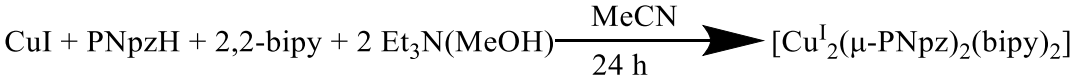

*Scheme 9. Reaction conditions for the synthesis of complex **2**.*

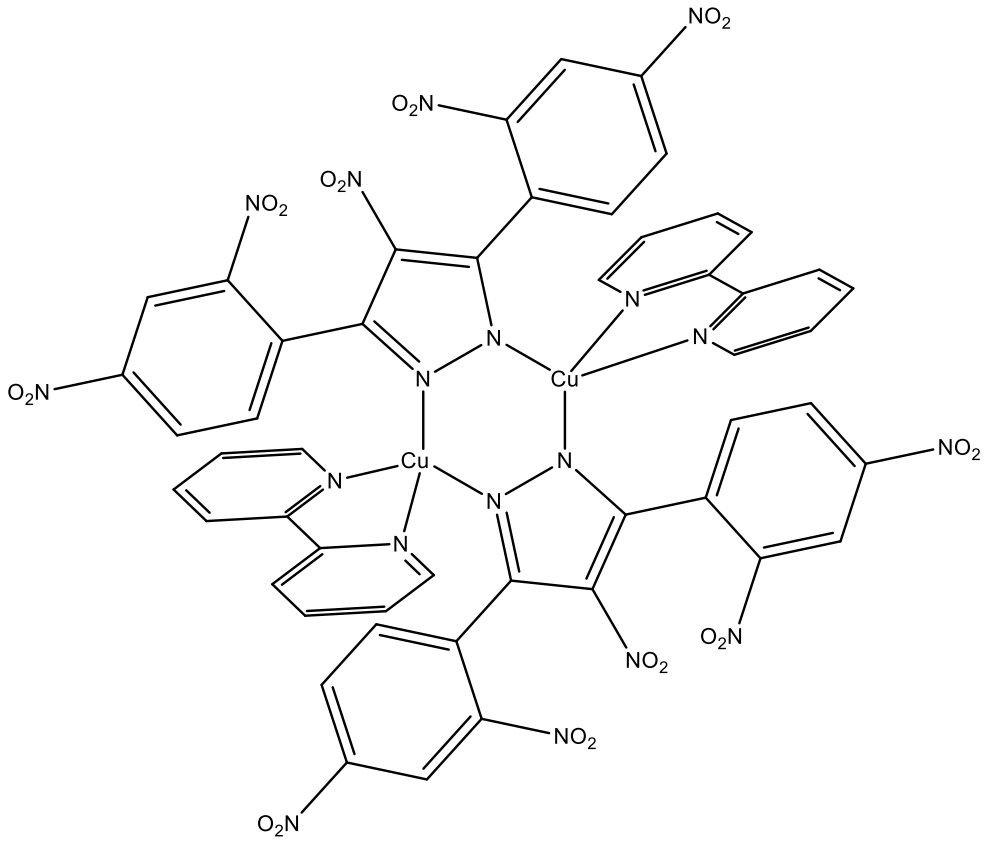

*Figure 22. Line drawing of complex **2**.*

^{1}H-NMR performed on complex **2** shows overlapping PNpz^{-} and bipy peaks in the aromatic region (Figure 23). No broad N-H, O-H, peaks were detected, nor paramagnetically shifted peaks. Figure 24 shows the FTIR spectrum of complex **2**. Figure 28 shows the UV-Vis spectrum of complex **2**.

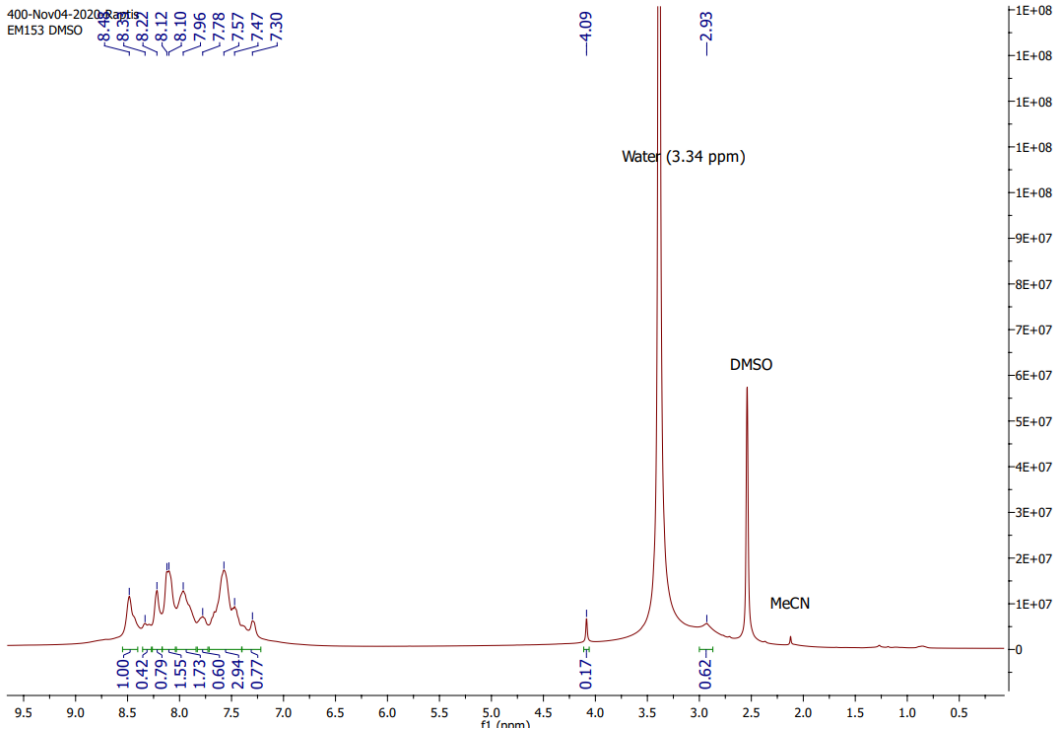

*Figure 23. ^{1}H-NMR spectrum (400 MHz, d_6-DMSO, ppm) of complex **2**.*

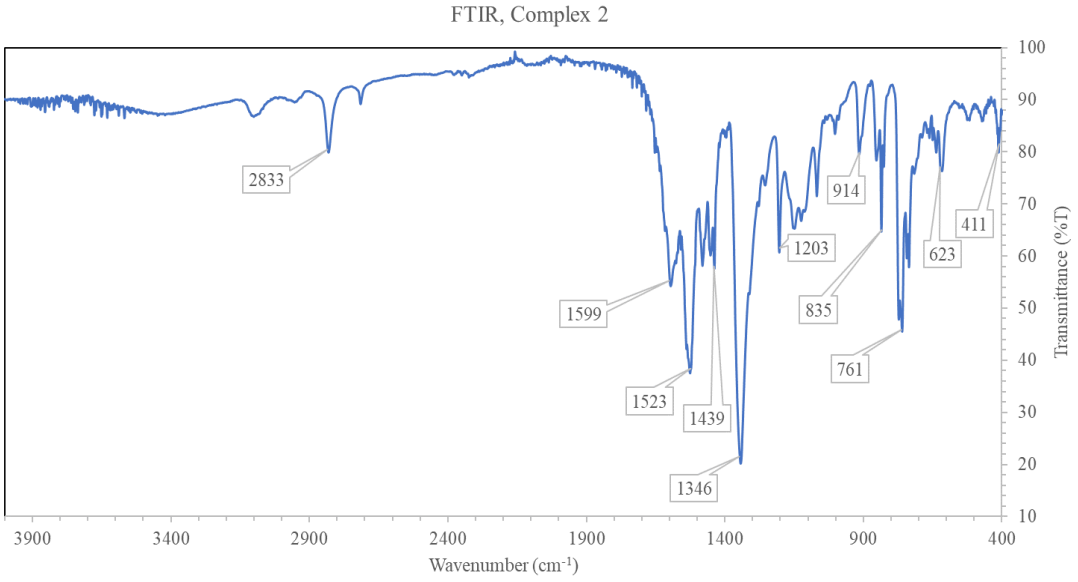

*Figure 24. FTIR spectrum (4 cm^{-1} resolution, ATR, crystalline sample) of complex **2**.*

2.3.1.3: Copper(II) dimers with unique bridging ligand: Complexes 3, 4.

Reacting complex **2** with DMSO produces a species that is bridged by μ_2-$O_2SMe_2^{2-}$ (Scheme 10). Figure 25 shows the line drawing of the complex. DMSO is known to be a coordinating ligand, however in this case, the DMSO has addressed an O^{2-} (from atmospheric O_2) to form an $O_2SMe_2^{2-}$ species, while the metal centers are oxidized from Cu^{I}_2 to Cu^{II}_2. The crystal structure of the **3** shows the bridging μ_2-O_2SMe_2 to be in a seesaw configure with a lone pair on the S-atom as opposed to a tetrahedral geometry which is indicative of dimethyl sulfone. Oxidation of DMSO to methyl sulfonyl methane (MSM) typically involves the use of ozone or hydroxyl radicals, however in the present case, neither have been employed. [114] [115]. The serendipitous discovery that **2** can mediate the transfer of O^{2-} originally alerted us to the possibility of employing this dinuclear complex as an oxidation/oxygenation catalyst.

$$Cu(OH)_2 + PNpzH + 2,2\text{-bipy} + DMSO \xrightarrow[24\ h]{MeOH} [Cu^{II}_2(\mu_2\text{-}DMSO_2)(\mu\text{-}PNpz)_2(bipy)_2]$$

*Scheme 10. Reaction conditions for the synthesis of **3**.*

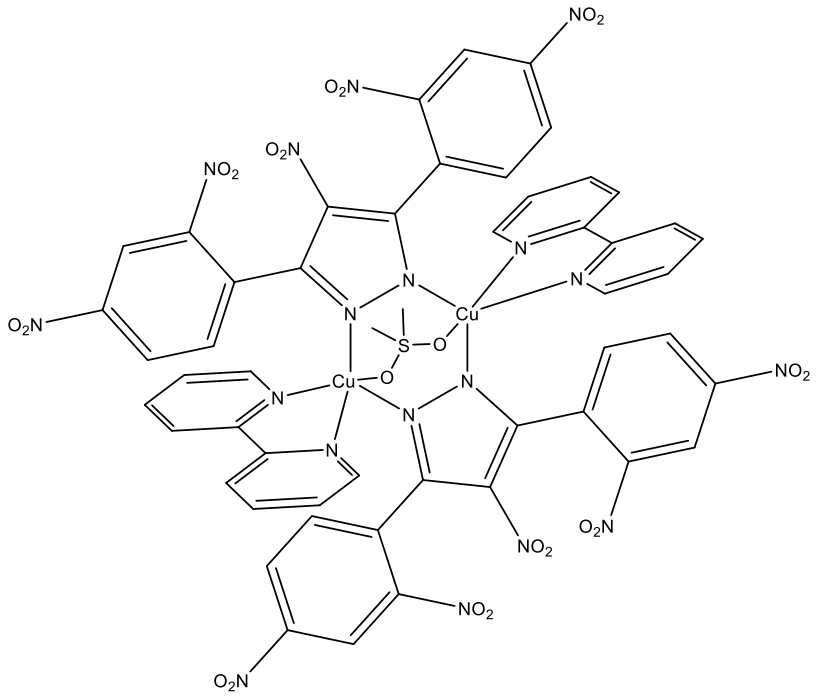

*Figure 25. Line drawing of complex **3**.*

A literature search for μ_2-$O_2SMe_2^{2-}$ specifically returned no results. Extensive research has been conducted on the catalytic oxidation of dialkyl and diaryl sulfides to their corresponding sulfoxides, both in homogenous and heterogenous systems [116] [117]. Catalytic oxidation to their corresponding sulfones, especially with respect to their kinetic and mechanistic studies, however, is scarce with only a few papers focusing on these compounds [118] [119] [120]. Examples of similar bridging ligands include μ_2-O_2SPh_2, μ_2-O_2SMe_2, and μ_2-O_2SeMe_2 (compounds **1a-4a′**) [121]. Table 9 compares select parameters of selenones and sulfones complexes with the one reported in this study. The rhodium complexes presented are polymeric, contain a neutral Me_2SO_2 ligand, and the sulfur atoms are in tetrahedral (T_d) geometry. What makes our complex so unique is that the bridging ligand is in fact a charged, $Me_2SO_2^{2-}$ species, and the geometry around the sulfur atom, C_{3v} supports this assignment. Table 10 shows a comparison of the free ligand.

*Table 9. Comparison of complex **3** with selected complexes of sulfones and selenones from the literature. Rhodium complexes are polymeric, with neutral Me_2SO_2 bridging ligands.*

Reference	Motif	M-M	M-O	M-O-S(Se)	O-S(Se)-O	O-S(Se)-C
[121]-**1a**	$Rh_2(\mu_2\text{-}O_2SMe_2)$	2.3951(9)	2.287(4), 2.307(4)	130.3(3), 139.9(3)	116.6(3)	108.3(3), 106.7(3)
[121]-**2a**	$Rh_2(\mu_2\text{-}O_2SPh_2)$	2.3947(9)	2.301(4), 2.290(4)	127.2(2), 163.9(3)	116.9(2)	108.0(3), 107.7(3)
[121]-**2b**	$Rh_2(\mu\text{-}O_2SPh_2)$	2.3973(4)	2.306(2)	132.07(13)	118.53(13)	107.84(14), 106.33(13)
[121]-**3b**	$Rh_2(\mu\text{-}O_2SMe_2)$	2.4104(7)	2.272(3)	127.2(2)	112.1(2)	110.2(2), 104.1(2)
[121]-**4a**	$Rh_2(\mu\text{-}O_2SeMe_2)$	2.4045(4)	2.265(2)	125.05(11)	118.38(14)	107.10(12), 109.98(17)
[121]-**4a′**	$Rh_2(\mu_2\text{-}O_2SPh_2)$	2.3988(6)	2.243(3), 2.266(2)	120.36(12), 142.30(15)	113.46(13)	109.00(17), 107.13(16)
This work (complex **3**)	$Cu_2(\mu_2\text{-}O_2DMS)$	3.617(2)	1.894(1), 1.896(9)	142.2(7), 138.1(7)	114.3(7)	123.5(9), 92.4(1)

Table 10. Comparison of free Me_2SO_2 to the coordinated $Me_2SO_2^{2-}$ in this work.

Molecule	Bond (Å) Angle (º)	Free Ligand	Coordinated Ligand (Complex **3**) $Me_2SO_2^{2-}$
Dimethyl Sulfone 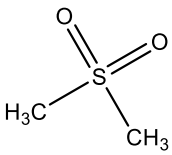	S=O S-C O-S-O C-S-O C-S-C	1.446(3) 1.765(5) 117.3(2) 108.5(1) 104.8(2)	1.376(1), 1.445(1) 1.780(3), 1.312(1) 114.3(7) 92.4(1), 123.5(9) 97.3(1)

As no counterion was found, the species is determined to be a neutral Cu^{II}_2 complex, with a bridging $(Me_2SO_2)^{2-}$ ligand. ^{1}H-NMR spectrum reveals the presence of a paramagnetic species with broad peaks between 30-60 ppm (Figure 26). Figure 27 shows the FTIR spectrum of the complex. Compared to the IR of complex **2**, several new peaks appear between 1000-800 cm^{-1} denoting the $(Me_2SO_2)^{2-}$ bridge. Free DMSO contains an S=O frequency at 1400 cm^{-1}, while free Me_2SO_2 shows an S=O at ~1300cm^{-1}, in the Rh compounds, this has shifted towards ~1140 cm^{-1}, and ~1100 cm^{-1} in complex **3**.The UV-Vis spectrum of complex **3** shows a shift compared to complex **2** in the aromatic region (Figure 28).

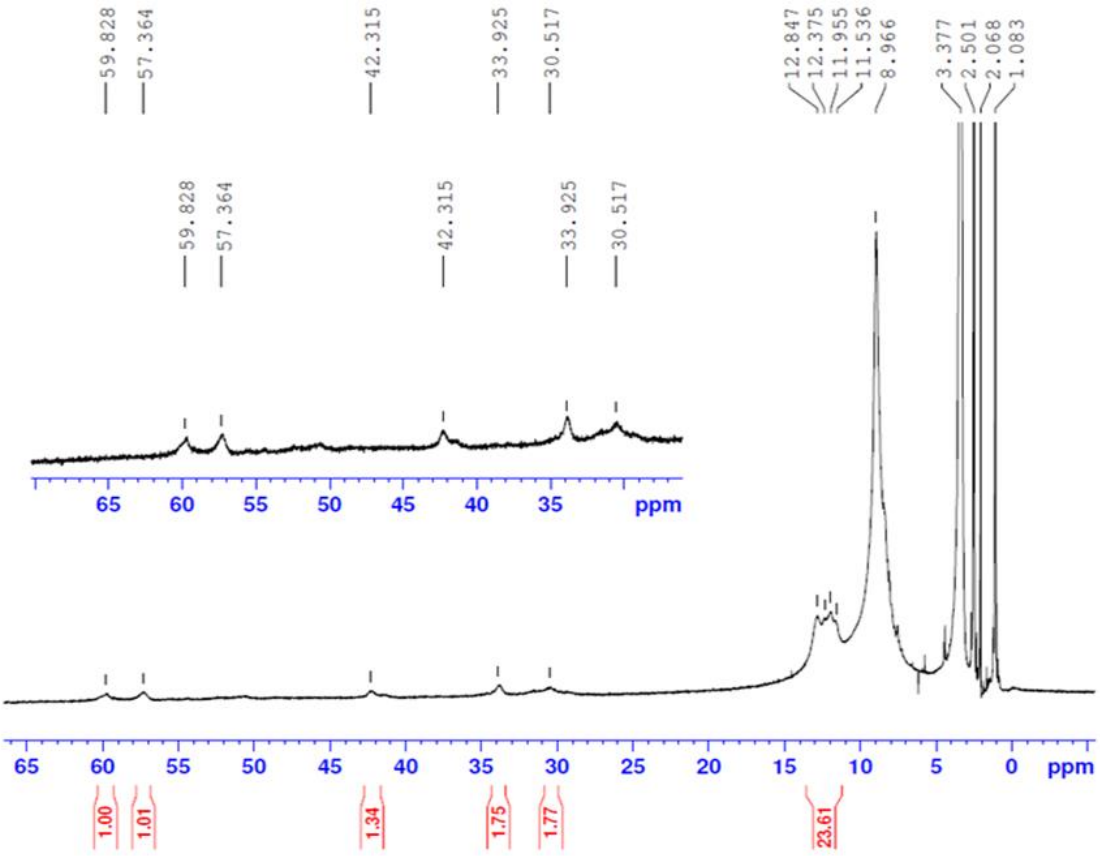

*Figure 26. ^{1}H-NMR spectrum (400 MHz, d_6-DMSO, ppm) of complex **3**.*

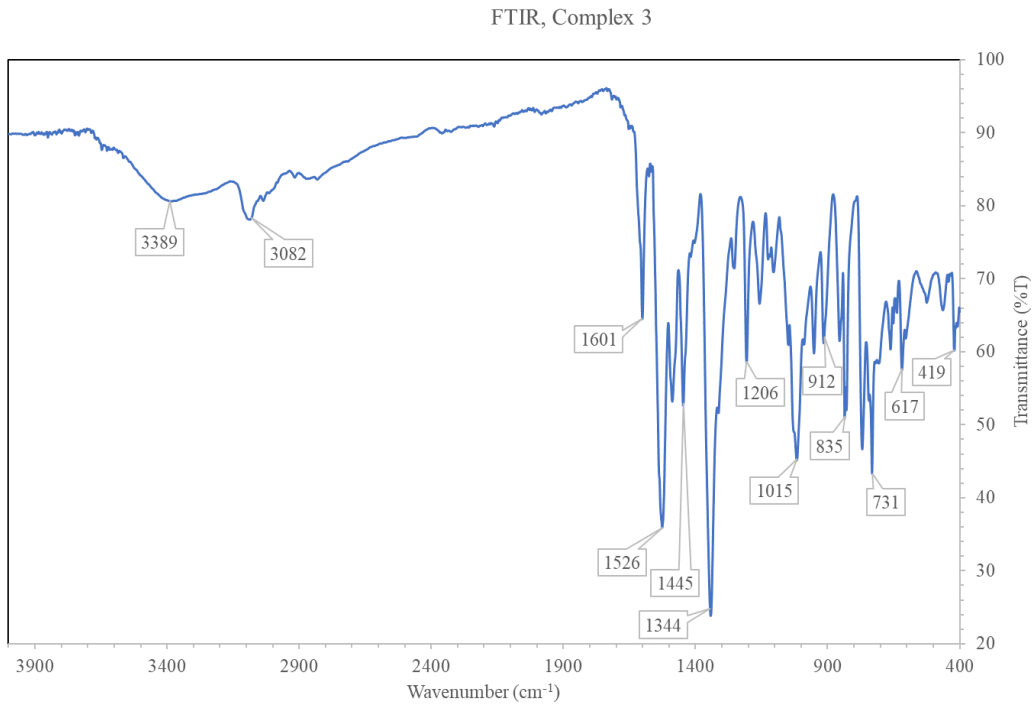

*Figure 27. FTIR spectrum (4 cm^{-1} resolution, ATR, crystalline sample) of complex **3**.*

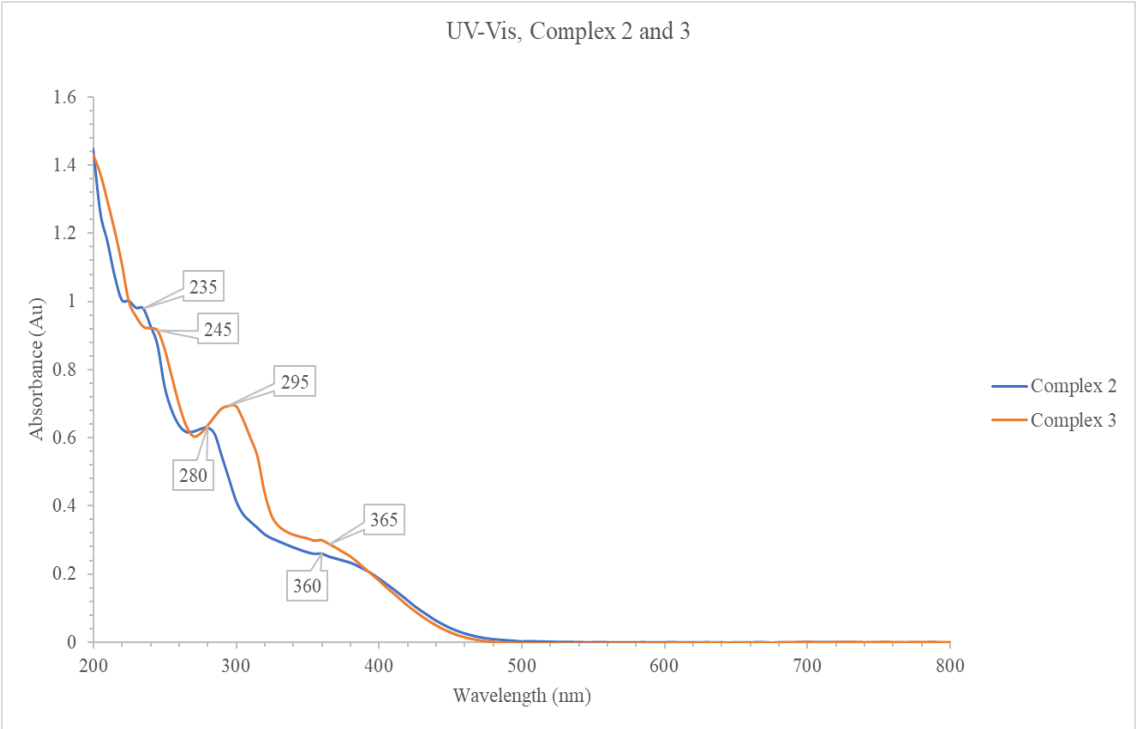

*Figure 28. UV-Vis spectrum of complexes **2** and **3** (1 mM/MeCN, quartz cuvette).*

Next in the series is the triple pyrazole bridged complex **4**, which can be made by using complex **2** as a starting material and reacting with benzoic acid copper(II) and excess PNpzH (Scheme 11). Figure 29 shows the line drawing of the complex. The benzoate is able to displace the auxiliary bipy ligands and a third bridging pyrazole is introduced into the system, the total charge of the system remains ambiguous, as no counterion was detected by SCXRD. The triply-bridged motif is unprecedented in Cu chemistry, except for copper(II) MOF's and polymers [122]. However, a firm determination of the oxidation state of the two Cu centers cannot be made without magnetic susceptibility measurements and/or an EPR spectrum. There are two possible interpretations based on the structural data alone: (a) this is a mixed-valent $Cu^{II}Cu^{III}$ species, or (b) it is a Cu^{II}_2 species with an invisible (to X-rays) H^+ somewhere on the ligands, possibly protonating one of the $-NO_2$ groups.

$$[Cu^{I}_2] + PNpzH + Cu(C_6H_5CO_2)_2 + Et_3N \xrightarrow[2)\ DCM]{1)\ MeCN,\ 24\ h} [Cu_2(\mu\text{-}PNpz)_3(O_2CH_5C_6)_2]$$

*Scheme 11. Reaction conditions for the synthesis of complex **4**.*

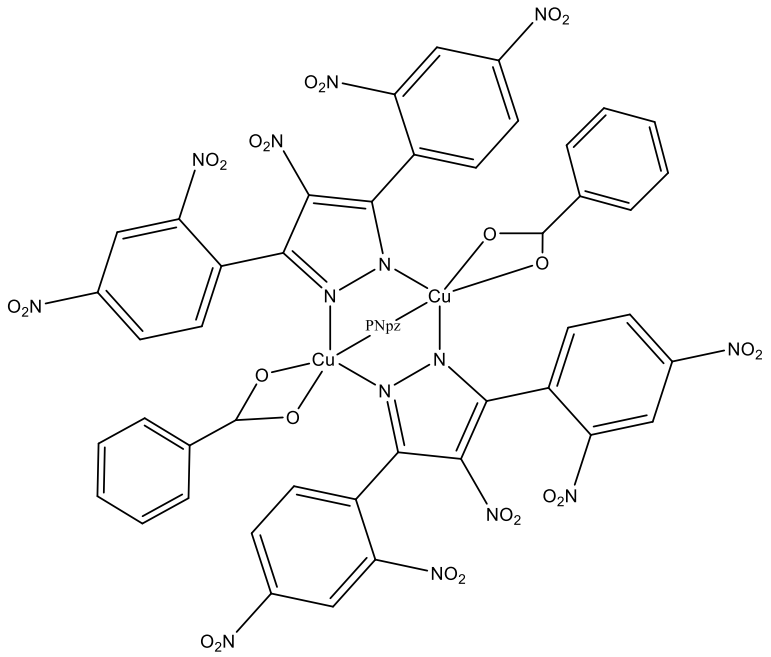

*Figure 29. Line Drawing of complex **4**.*

2.3.1.4: Copper(II) dimers with halogenated pyrazoles: Complexes 5-8.

In order to investigate the electrochemical properties of the bridging pyrazole ligand, several complexes were synthesized starting from the halogenated 4-X-3,5-Ph_2-pzH. The first in the series is complex **5**, using the brominated pyrazole, synthesis of a complex similar to **1** and/or **2** was expected, however this was not the case. The resulting complex was a copper(II) dimer with a similar skeleton to complex **2**, however, two non-bridging pz ligands coordinated to the Cu centers resulting in an inert system incapable of cycling between the Cu^{II} and Cu^{I} states (Scheme 12). Figure 30 shows the line drawing of complex **5**.

$$Cu(OH)_2 + \text{4-Br-3,5-Ph}_2\text{-pzH} + \text{2,2-bipy} \xrightarrow[24\ h]{MeCN} [Cu^{II}_2(\mu\text{-4-Br-3,5-Ph}_2\text{-pz})_2(\text{4-Br-3,5-Ph}_2\text{-pz})_2(\text{bipy})_2]$$

*Scheme 12. Reaction conditions for the synthesis of complex **5**.*

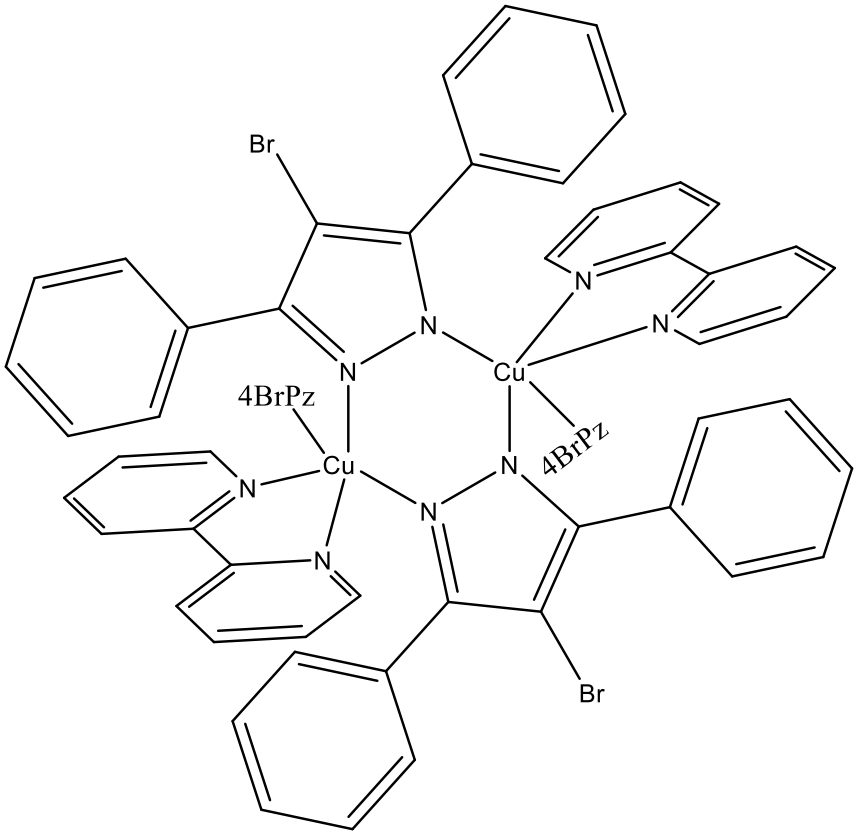

Figure 30. Line Drawing of Complex **5**.

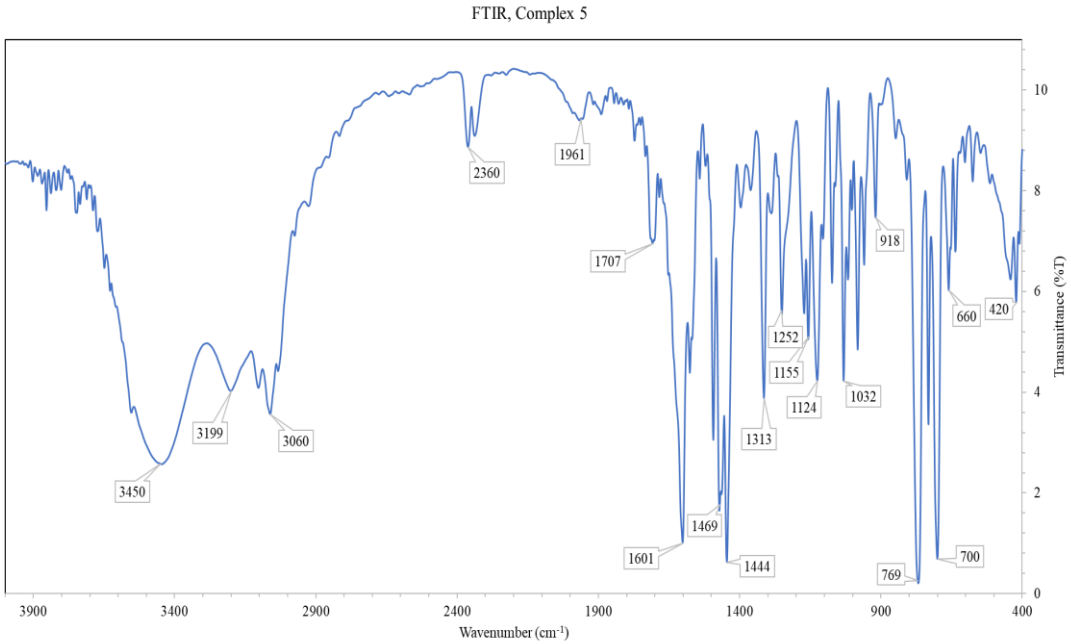

Figure 31. FTIR spectrum (4 cm^{-1} resolution, ATR, crystalline sample) of complex ***5.***

As the brominated pz did not produce the intended results, the more electronegative chlorinated analogue, 4-Cl-3,5-Ph_2-pzH was synthesized and employed. With the hopes of generating a catalytically active, oxo/hydroxo species, synthetic procedures of **2** were adapted to suit the new pz (Scheme 13). The resulting complex **6** was a welcomed surprise as it showed that synthesis of -oxo/hydroxo bridged copper(II) dimers was indeed possible with halogenated bulky pyrazoles. Complex **6** is structurally similar to the catalytically active species, complex **9**, however, some key differences lead to a stable, catalytically inert species. Assignment of the O-atom bridge is likely a hydroxo-bridge based on catalytic inertness, bond angle, and lack of secondary sphere interactions. Figure 32 shows the line drawing of the cationic portion of complex **6**.

$$CuI + 4\text{-Cl-3,5-}Ph_2\text{-pzH} + 2,2\text{-bipy} + Et_3N \xrightarrow[24\ h]{MeCN/DCM} [Cu^{II}{}_2(\mu\text{-OH})(\mu\text{-4-Cl-3,5-}Ph_2\text{-pz})_2(bipy)_2]I$$

Scheme 13. Reaction conditions for the synthesis of complex **6**.

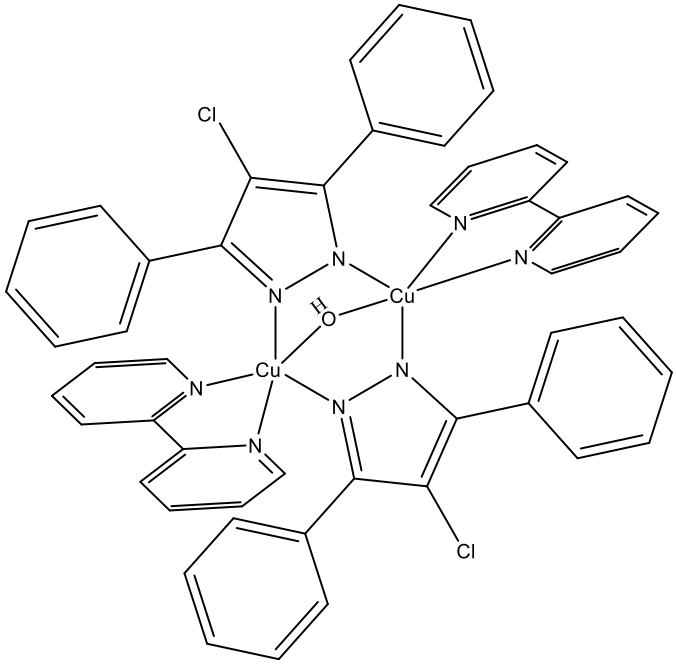

*Figure 32. Line drawing of complex **6**, showing the cation portion.*

Complex **6**, while important for establishing the importance of the secondary sphere effects, and their likely link towards catalytic oxidation, was itself inert, and as such the reaction conditions were modified in hopes of producing an active species. As in the case of the previous structure, an I^- counterion is present which is unable to mediate reactivity of the hydroxo bridging ligand, thus by employing a different starting material, that would avoid a halogen counterion altogether, it was our hope to produce a structural analogue of the Cu^I_2/Cu^{II}_2 couple. By swapping out CuI for $Cu(OH)_2$, and changing the solvent system, complex **7** was afforded (Scheme 14). Complex **7**, is again a structural analogue of complexes **6** and **9**, with the difference being that it is methoxy bridged. Complex **7** contains a total charge of +1 on the cationic proportion, with the -1 charge being supplied by an interstitial $[pz/MeOH]^-$ couple. At this time no methoxy-transfer chemistry has been shown by complex **7**, however it should not be ruled out without further studies. Figure 33 Shows the line drawing for complex **7**. Figure 34 shows the FTIR of **7**, which has been supportive in location of the Cu-O bond frequencies of more important Cu-oxo and Cu-hydroxo species.

$$Cu(OH)_2 + \text{4-Cl-3,5-Ph}_2\text{-pzH} + \text{2,2-bipy} \xrightarrow[24\ h]{\text{DCM/MeOH}} [Cu^{II}_2(\mu\text{-OMe})(\mu\text{-4-Cl-3,5-Ph}_2\text{-pz})_2(\text{bipy})_2]^+$$

Scheme 14. Reaction conditions for the synthesis of complex **7**.

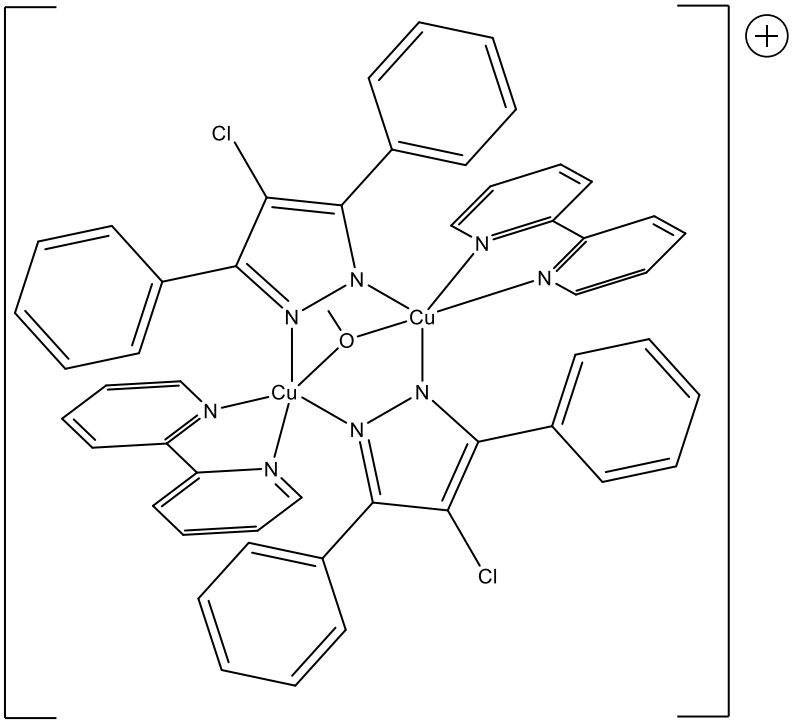

Figure 33. Line drawing of the cation portion of complex **7**.

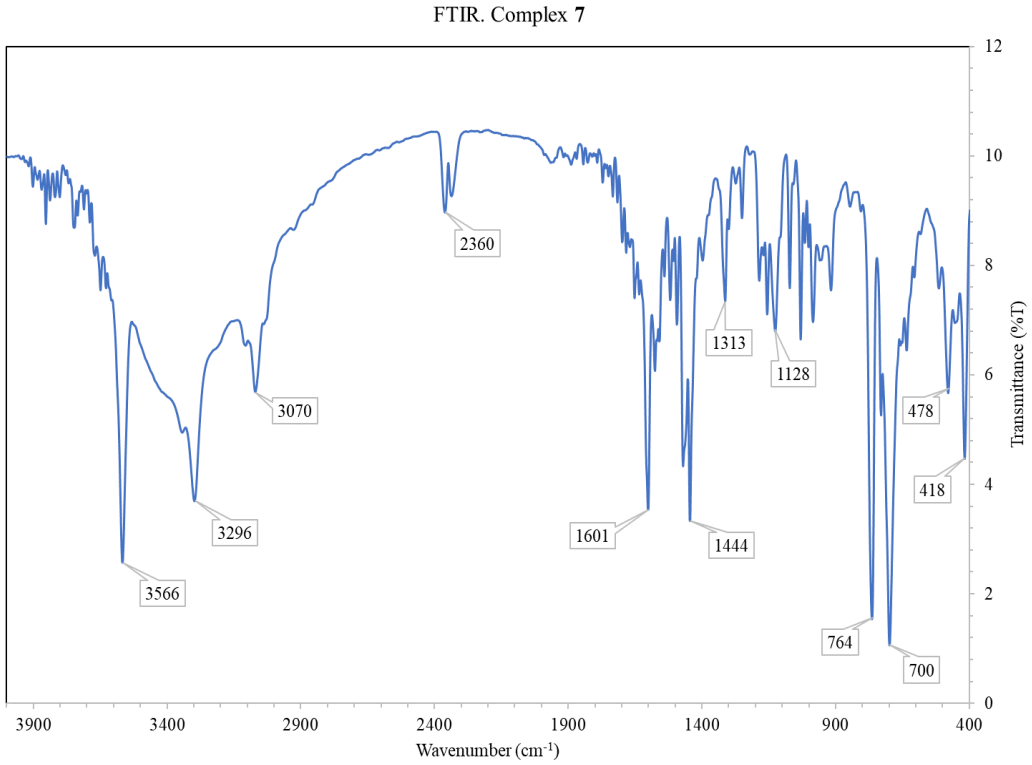

*Figure 34. FTIR spectrum (4 cm^{-1} resolution, ATR, crystalline sample) of complex **7**.*

Complex **8** is the last in the halogenated series, which highlights the flexibility and plasticity of copper complexes, as simplifying changing the order of the reagents, the solvent system, and/or the crystallization method, a host of new complexes are achievable. Scheme 15 shows the synthetic procedure employed, where MeOH is used to produce a methoxy bridged complex, however, unlike the previous one, only pz is bridging in this case, the other replaced by a μ-I (Figure 35). Complex **8**, has not shown any catalytic activity thus far, but it is useful in establishing the importance of secondary sphere interactions (absent in this case) and the malleability of copper(II) dimers.

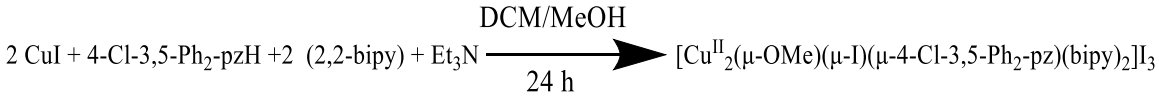

Scheme 15. Reaction conditions for the synthesis of complex **8**.

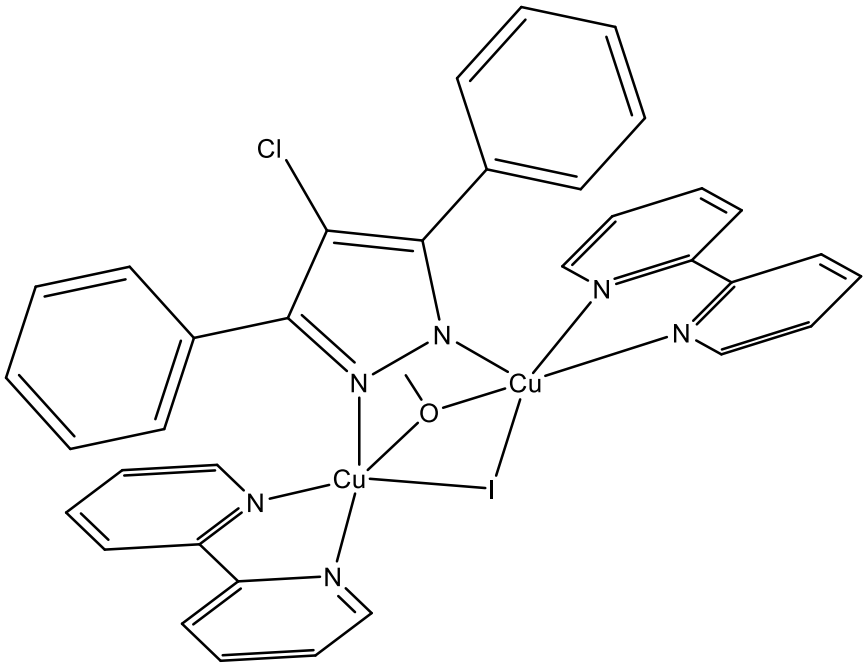

*Figure 35. Line Drawing of complex **8**; I_3^- counterion has been omitted.*

2.3.1.5: Copper(II) dimers with catalytic properties: Complexes 9-10*.

The most important complex in this series is complex **9**, with its unique secondary sphere interactions with a $PNpz^-$ molecule. Complex **9** can be synthezied by using crystals of complex **2**, or in a one pot synthesis using $Cu(OH)_2$ (Scheme 16). Figure 36 shows the line drawing of the cationic portion of the complex. The complex's coordination environment mimics that of biological metalloproteins whose chemistry is affected by interactions with species in their secondary coordination sphere. The complex features a bridging O-atom, with hydrogen bonding to a $PNpz^-$ molecule which imparts partial stability onto the complex. Crystallographically ambiguous, the more favorable assignment is μ-OH…$PNpz^-$, rather than μ-O…HPNpz, based on structural comparison with similar complexes whose molecular formula is unambiguously determined by crystallography (A summary of the motifs synthesized, and their properties is shown in **Table 11. By comparing the parameters of** motifs in this work, to those of similar complexes in the literature, a plot summarizing Cu-Cu distances vs Cu-O-Cu angles can be used to represent the correlation between these parameters and the assignment of oxo vs. hydroxo species (Figure 57*)*. What makes the catalytically active complex 9 unique is that it falls somewhere in-between an oxo/hydroxo species, where the resting state is more closely related to a hydroxo complex with a SSI to the anion, and when deprotonated, it results in a reactive, bent-oxo species. Scheme 18-Scheme 20 shows the summary of complexes synthesized in this work.

Table 11). The latter form, involving a bent Cu-O-Cu, is expected to be unstable and reactive. Examples of reactive copper(II) oxo complexes are not uncommon, however they

typically require a supporting zeolite, high temperatures/pressures, or coreductants. The critical role of the secondary sphere interactions is highlighted by the fact that the similar complex **6**, differing only in the peripheral substitution of the bridging pyrazolato ligands, does not show any of the catalytic activity of **9** (vide infra, Chapter 3).

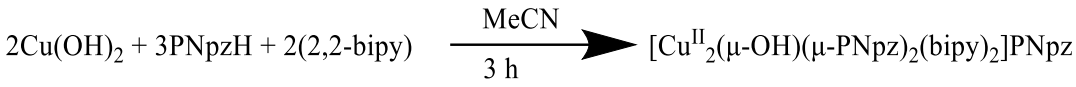

*Scheme 16. Reaction conditions for the synthesis of **9**.*

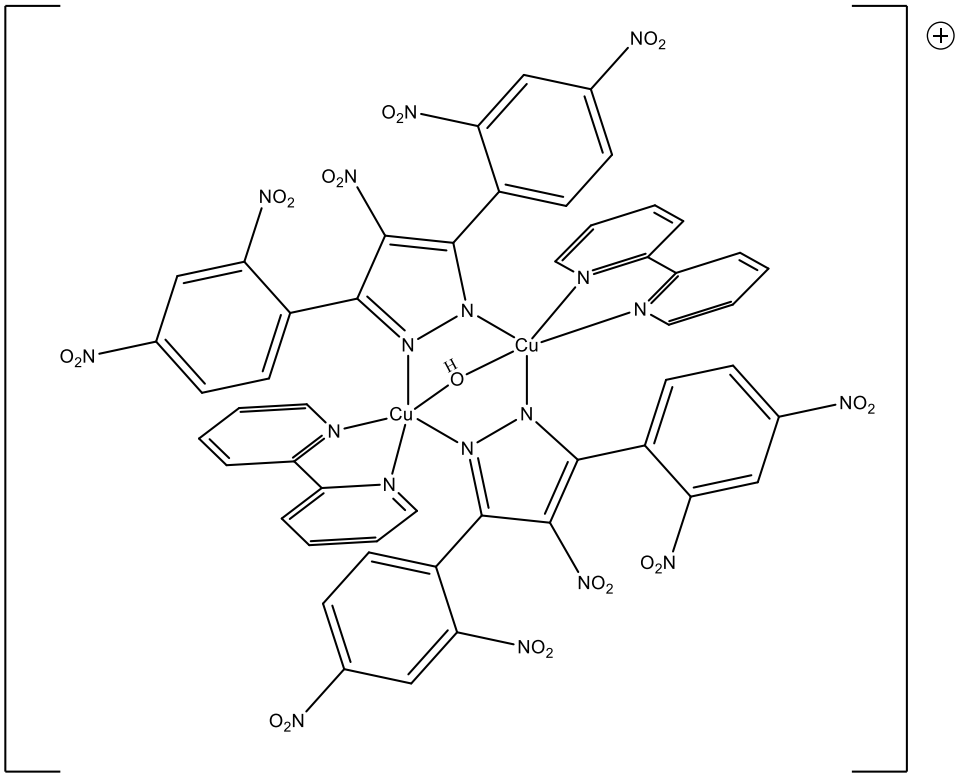

Figure 36. Line Drawing of the complex cation of **9**.

Figure 37 shows the FTIR spectrum of complex 9. In order to further investigate the bridging ligand of **9**, labeled O^{18} was employed. The complex was synthesized using method **A** and substituting Et_3N for $NaO^{18}H$. The peak at 472 cm^{-1} was shifted and broadened to 464 cm^{-1}, as expected of the isotopic shift of O^{16} *vs* O^{18} (*Figure 38*). Typical

$\tilde{\nu}_{Cu\text{-}O}$ expected for oxo-bridged species range from 400 to 700 cm^{-1}, and 700 to 950 cm^{-1} for hydroxo-bridged species. The h-bonded nature of **9** likely accounts for the shift towards higher energy as compared to both oxo and hydroxo species. Figure 39 shows the UV-Vis spectrum of complex 9.

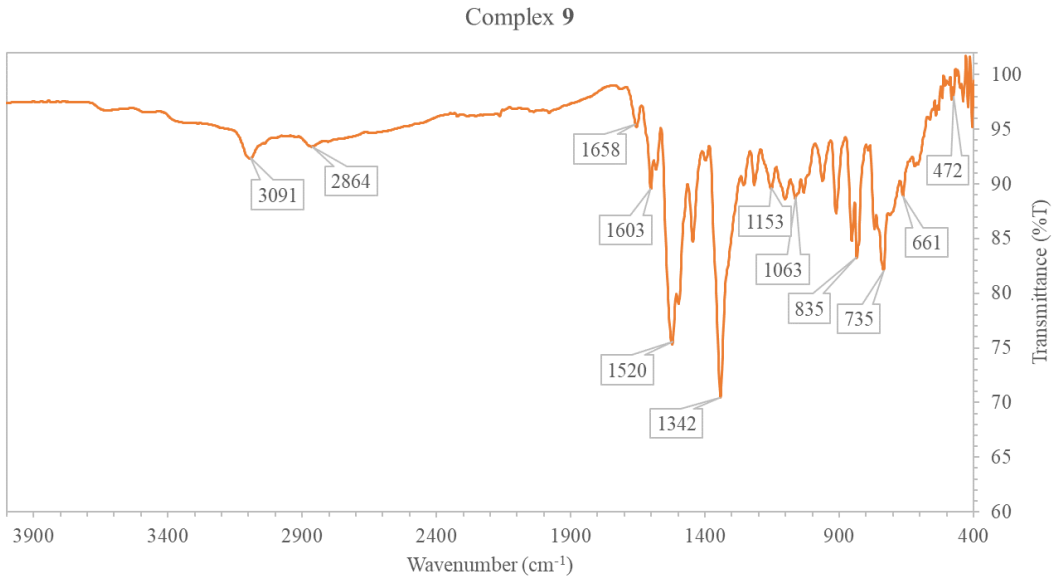

*Figure 37. FTIR spectrum (4 cm^{-1} resolution, CsI pellet) of complex **9**.*

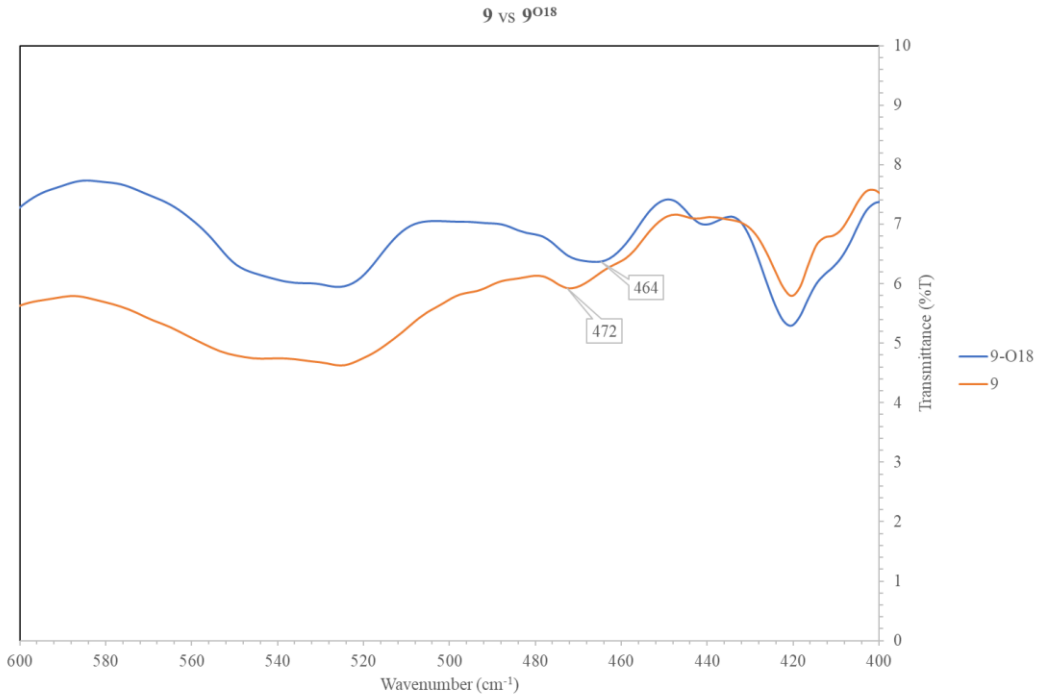

*Figure 38. FTIR spectrum (4 cm^{-1} resolution, CsI pellet) of O^{18} labeled experiment. Complex **9** (dark yellow) vs **9-O^{18}** (dark blue).*

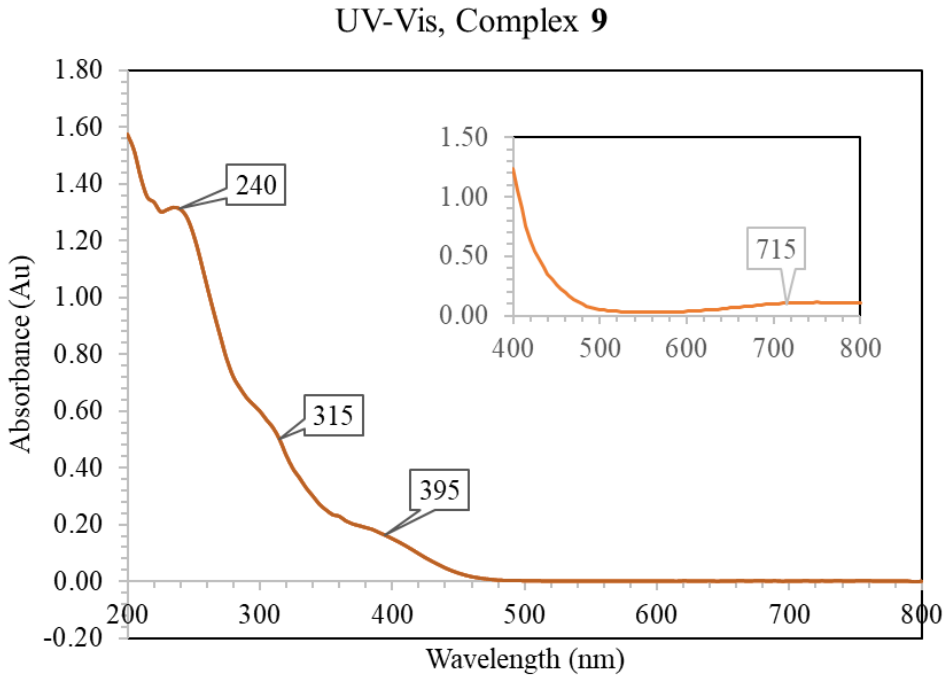

Figure 39. UV-Vis of complex **9** (1 mM in MeCN, quartz cuvette). Inset showing UV region (~10 mM in MeCN).

A secondary monomeric complex, **10**, co-crystallizes in the form of deep blue, rigid plate-like crystals, alongside the crystals of complex **9**. The blue crystals are typically removed as an undesired product by washing with methanol, in which they are highly soluble. Once dissolved in methanol, the deep blue crystals produce a dark green solution, however the green plate crystals of **9** are insoluble in methanol. Scheme 17 shows the optimized synthesis of the complex, Figure 40 shows the line drawing of the complex. Complex **10** is a monomeric copper(II) center, with one chelating bipy, two monodentate PNpz's, and one coordinated H_2O. A hydrogen bonded water molecule exists in the lattice much like in that of complex **9**. So far it has not been shown possible to form complex **9** from **10**, nor has any catalytic activity been detected thus far.

$$Cu(OH)_2 + 2PNpzH + (2,2\text{-bipy}) \xrightarrow[3\ h]{MeCN} [Cu^{II}(OH_2)(PNpz)_2(bipy)].H_2O$$

*Scheme 17. Reaction conditions for the synthesis of complex **10**.*

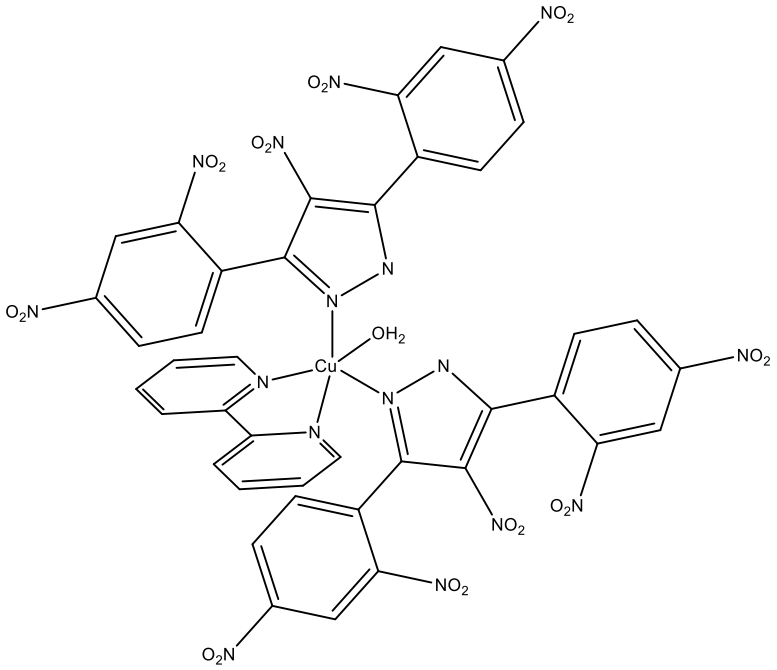

*Figure 40. Line Drawing of complex **10**.*

2.3.2 Crystal structural descriptions

2.3.2.1: Copper(I) dimers: Complexes 1, 2.

Complex **1** crystallizes in the monoclinic $P2_1/c$ space group with half the molecule in the asymmetric unit. The Cu(I) centers sit 3.372(1) Å apart, coordinated acetonitrile groups are at Cu-N distances of 1.933(4)/1.933(4) Å for Cu1and Cu2. Cu—N distances of bridging pyrazolato ligands are: 1.971(3) & 1.999(1) Å for Cu1; 1.999(1) & 1.971(3) Å for Cu2. Figure 41 shows the crystal structure of the complex.

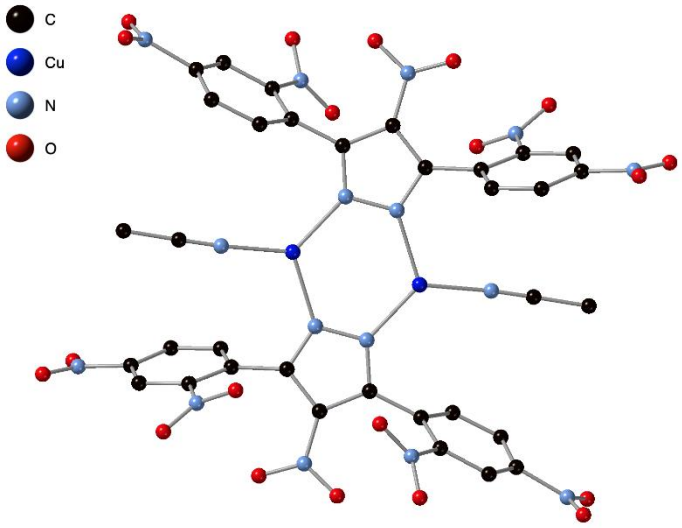

*Figure 41. Ball and stick representation of complex **1**. H-atoms omitted for clarity.*

Complex **2** crystallizes in the orthorhombic *Pccn* space group with half the molecule in the asymmetric unit. The Cu(I) centers sit 3.409(1) Å apart. 2,2'-bipy N-atoms are closer to the Cu centers, at 2.098(5) and 2.036(4) for Cu1 and 2.098(5) and 2.036(4) Å for Cu2. Cu—N distances of bridging pyrazolato ligands are: 1.963(4) & 1.975(4) Å for Cu1; 1.963(4) & 1.975(4) Å for Cu2. Figure 42 shows the crystal structure of the two complexes. Figure 43 shows the crystals under a microscope.

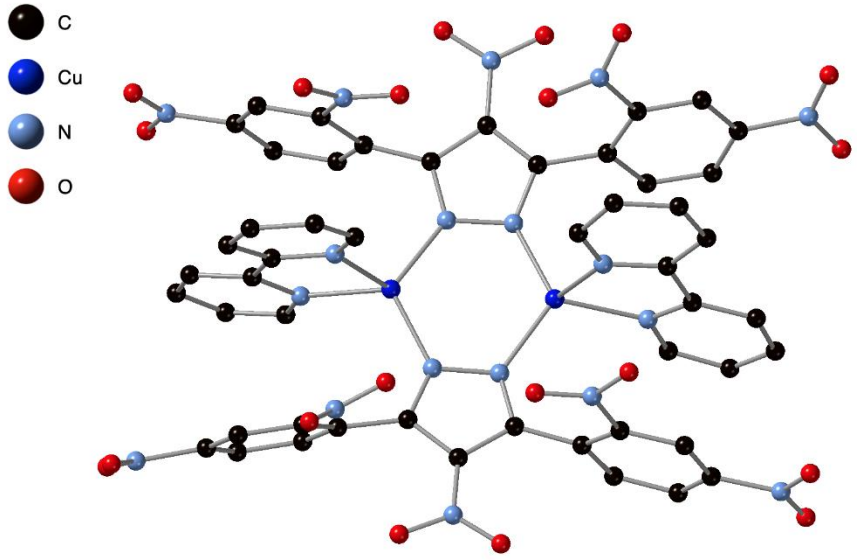

*Figure 42. Ball and stick representation of complex **2**. H-atoms omitted for clarity.*

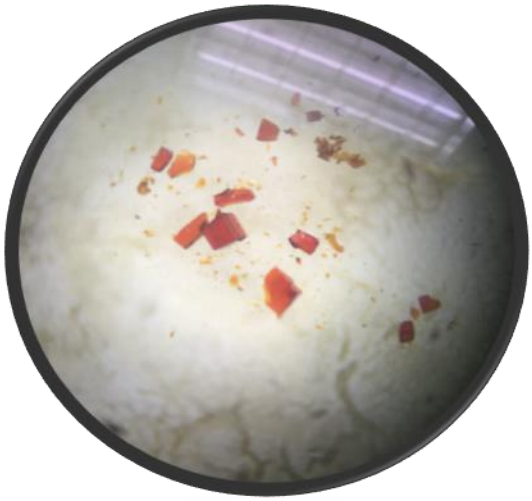

*Figure 43. Red crystals of complex **2** under a microscope.*

2.3.2.2: Copper(II) dimers with unique bridging ligand: Complexes 3, 4.

Complex **3** crystallizes in the monoclinic *C*2/*c* space group with a full molecule in the asymmetric unit. The Cu(II) centers are 3.617(2) Å apart. Bipy N-atoms are 2.043(9) and 1.986(1) Å for Cu1 and 2.028(1) and 2.012(1) Å for Cu2. Cu—N distances of bridging pyrazolato ligands are: 2.095(9), 2.074(9) Å for Cu1 and 2.064(9), 2.136(1) Å for Cu2. The Bridging oxygens distances are 1.896(9) Å for Cu1—O1 and for 1.894(1) Å Cu2—O2.

Figure 44 shows the crystal structure. Figure 45 shows the crystals of complex 3 under a microscope.

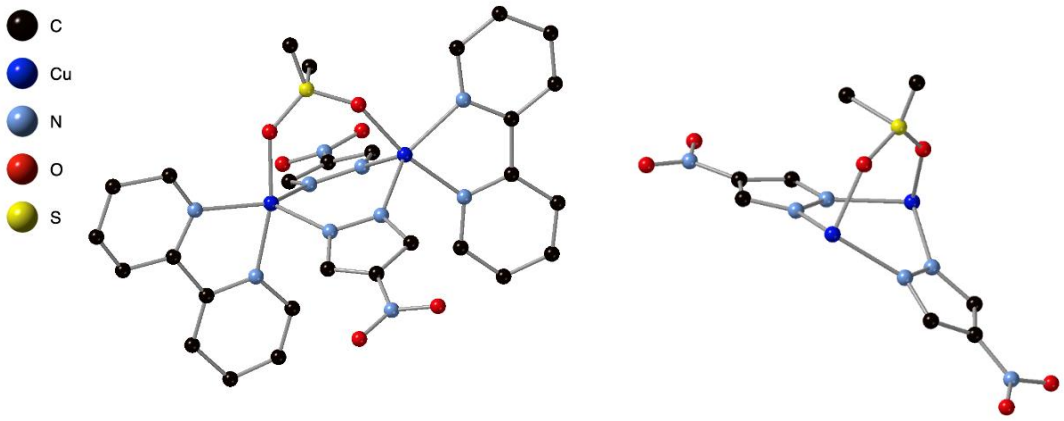

*Figure 44. Ball and stick representation of complex **3** (left); The 2,4-dinitrophenyl groups of the bridging PNpz$^-$ ligans have been omitted for clarity. Bipy rings and phenyl groups have been omitted to highlight the bridging $(DMSO_2)^{2-}$ ligand (right).*

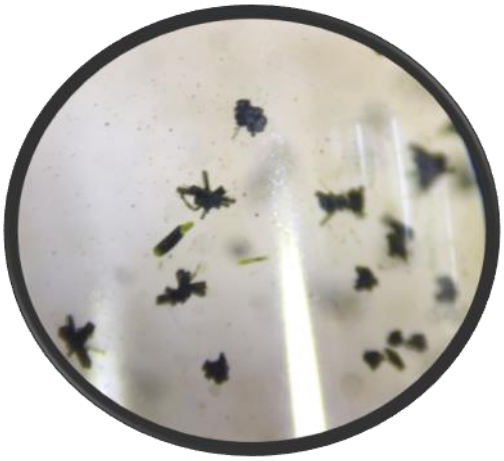

Figure 45. Crystals of complex 3 under a microscope.

Complex **4** crystallizes in the monoclinic *C2/c* space group with half the molecule in the asymmetric unit. The Cu centers are 3.298(1) Å apart. Benzoate O-atoms are 2.090(4) and 19.69(5) Å for Cu1 and 2.090(4) and 1.969(5) Å for Cu2. Cu—N distances of bridging pyrazolato ligands are: 1.963(5), 2.129(4), 2.012(5) Å for Cu1 and 1.963(5), 2.012(5),

2.129(4) Å for Cu2. Figure 46 shows the crystal structure. Figure 47 shows the crystals under a microscope.

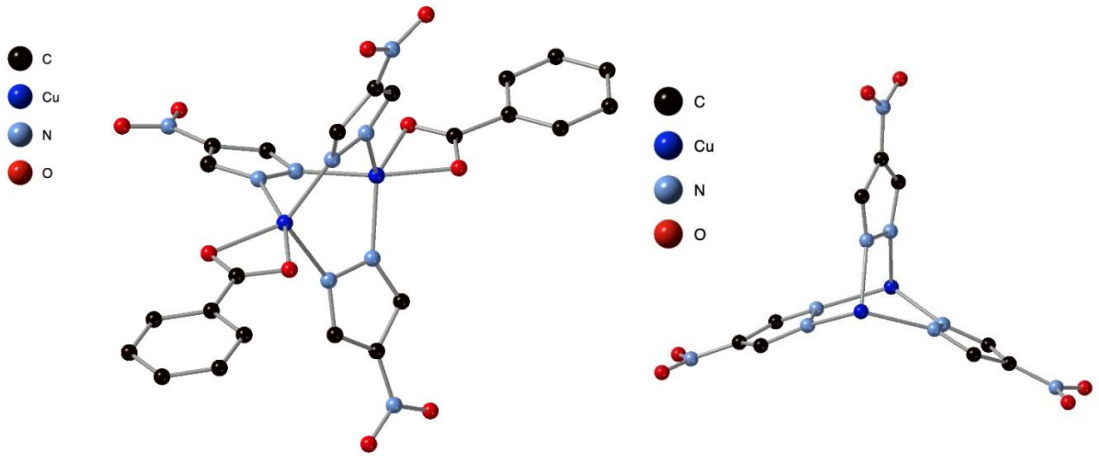

*Figure 46. Ball and stick representation of complex **4**. The 2,4-dinitrophenyl groups on the bridging PNpz⁻ ligands have been omitted for clarity (left). Close up of the triple bridged-nature of the complex, resembling a propeller (right).*

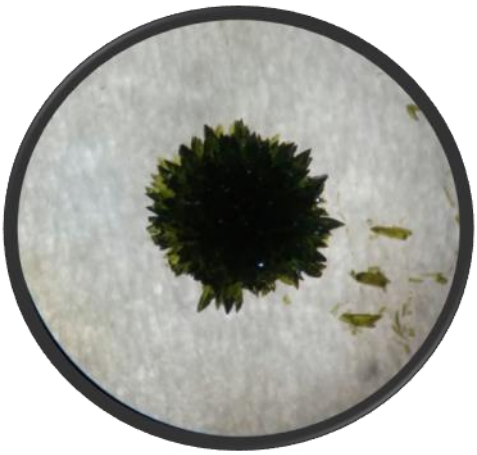

*Figure 47. Turquoise flower crystals of complex **4**.*

2.3.2.3: Copper(II) dimers with halogenated pyrazoles: Complexes 5-8.

Complex **5** crystallizes in the monoclinic $P2_1/n$ space group with half the molecule in the asymmetric unit. The Cu(II) centers sit 3.860(6) Å apart. 2,2'-bipy N-atoms are closer to

the Cu centers, at 2.024(2) and 2.095(2) for Cu1 and 2.095(2) and 2024(2) Å for Cu2. Cu—N distances of bridging pyrazolato ligands are: 2.221(2) & 2.017(1) Å for Cu1; 2.017(1) Å & 2.221(2) Å for Cu2. The Cu—N distances of the auxiliary pyrazoles are: 1.986(2) Å for Cu1; 1.986(2) Å for Cu2. Figure 48 shows the crystal structure.

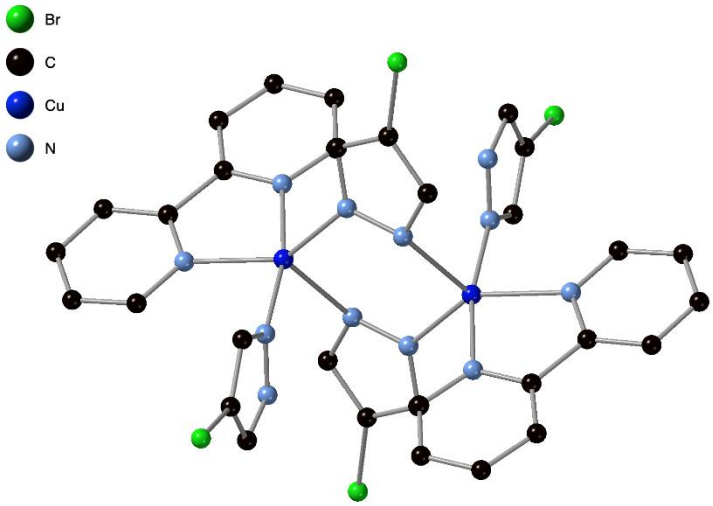

Figure 48. Ball and stick representation of complex **5**; H-atoms and the phenyl rings on the 4-Br-3,5-Ph_2-pz ligands have been omitted for clarity.

Complex **6** crystallizes in the monoclinic *C*2/*c* space group with the whole molecule in the asymmetric unit. The Cu(II) centers sit 2.978(3) Å apart. 2,2'-bipy N-atoms are closer to the Cu centers, at 2.057(6) and 2.000(7) for Cu1 and 2.050(9) and 1.979(8) Å for Cu2. Cu—N distances of bridging pyrazolato ligands are: 2.070(7) & 2.076(7) Å for Cu1; 2.075(8) Å & 2.067(7) Å for Cu2. The Cu—O distances are: 1.917(7) and 1.943(8) Å. The Cu-O-Cu bond angle is 101.0(4)°. Figure 49 shows the crystal structure for the complex. There is an I^- counterion. Figure 50 shows the crystals under a microscope.

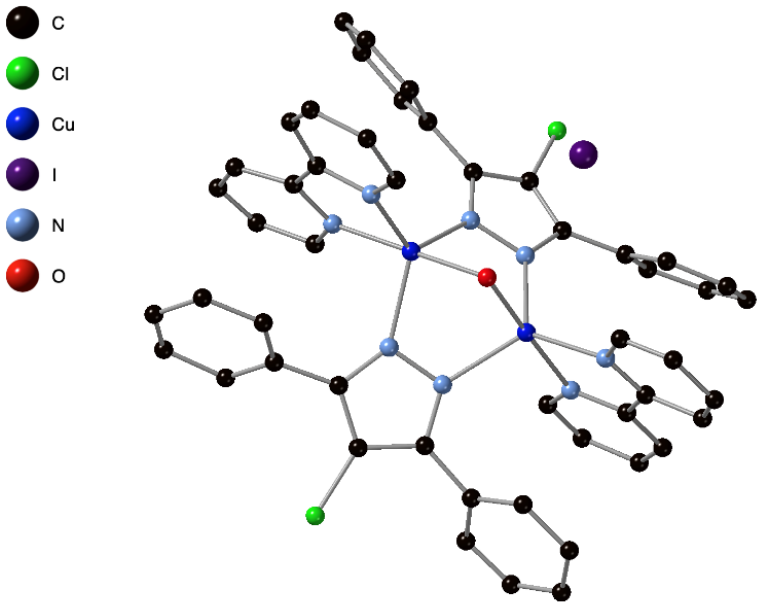

*Figure 49. Ball and stick representation of complex **6**; H-atoms omitted for clarity.*

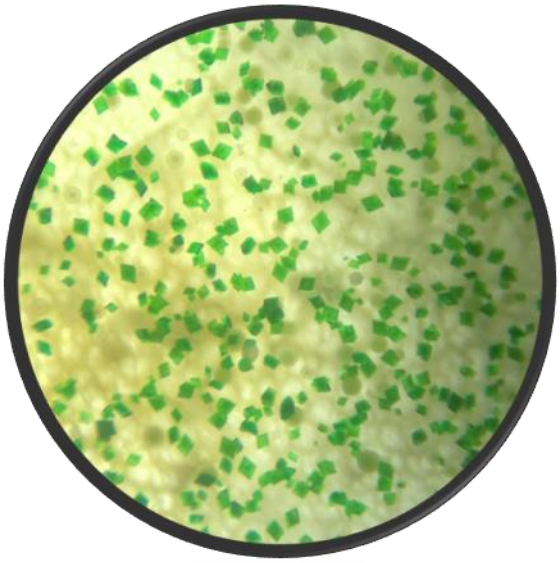

*Figure 50. Light green crystals of complex **6**.*

The crystals of complex **7** are long green needles in shape and tend to crystallize as clusters in the triclinic *P*-1 space group with the whole molecule in the asymmetric unit. The Cu centers are in an N_4O trigonal bipyramidal arrangement with N_2O making the trigonal plane. The Cu(II) centers sit 2.978(4) Å apart. 2,2'-bipy N-atoms are closer to the Cu

centers, at 2.093(2) and 1.989(1) for Cu1 and 2.112(2) and 1.978(1) Å for Cu2. Cu—N distances of bridging pyrazolato ligands are: 2.069(1) & 2.065(1) Å for Cu1; 2.079(2) Å & 2.079(1) Å for Cu2. The Cu—O distances are: 1.950(1) and 1.944(1) Å. The μ-OMe sits 1.255(1) Å from the Cu—Cu bond. The Cu-O-Cu bond angle is 99.72(7)°. There is also a hydrogen bond between the pyrazolate and a methanol solvent with a distance of 2.764(3) Å for the N—O bond. Figure 51 shows the crystal structure for the complex. Figure 52 shows the crystals of **7** under a microscope.

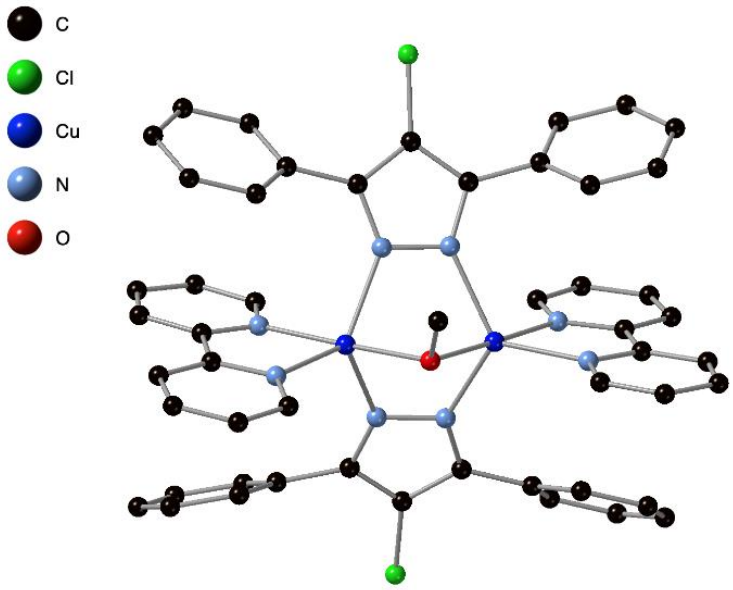

*Figure 51. Ball and stick representation of the cationic portion of complex **7**. H-atoms are omitted for clarity on the structure, pyrazolate/methanol counterion has been omitted.*

*Figure 52. Green crystals of complex **7**.*

Complex **8** crystallizes in the orthorhombic *Pnma* space group with half the molecule in the asymmetric unit. The Cu(II) centers sit 2.980(1) Å apart. 2,2'-bipy N-atoms are closer to the Cu centers, at 2.008(4) and 1.999(4) for Cu1 and 1.999(4) and 2.008(4) Å for Cu2. Cu—N distances of bridging pyrazolato ligand are 2.003(4) Å for Cu1 and 2.003(4) Å for Cu2. The Cu—O distances are: 1.944(3) and 1.944(3) Å. The Cu—I distances are: 2.880(8) and 2.880(8) Å. The μ-OMe sits 1.249(5) Å from the Cu—Cu bond plane, and the μ-I, 2.465(1). The Cu-O-Cu bond angle is 100.06(6)°, and 62.29(2)° for Cu-I-Cu. Figure 53 shows the crystal structure for the complex.

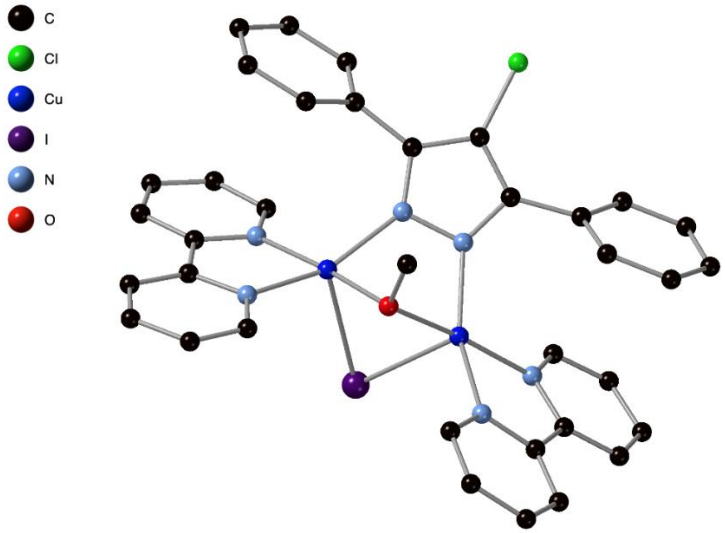

Figure 53. Ball and stick representation of the cationic portion of complex **8**. H-atoms and I_3^- counterion are omitted for clarity.

2.3.2.4: Copper(II) dimers with catalytic properties: Complexes 9-10*.

Complex **9** crystallizes in the triclinic *P*-1 space group with the whole molecule in the asymmetric unit. The Cu centers are in an N_4O trigonal bipyramidal arrangement with N_2O making up the trigonal plane. The Cu(II) centers sit 3.0034(2) Å apart. 2,2'-bipy N-atoms are closer to the Cu centers, at 2.048(3) and 1.985(3) for Cu1 and 1.988(2) and 2.030(2) Å for Cu2. Cu—N distances of bridging pyrazolato ligands are: 2.122(2) & 2.054(2) Å for Cu1; 2.065(2) & 2.115(2) Å for Cu2. The Cu—O distances are: 1.929(2) and 1.929(2) Å. The μ-O(H) sits 1.192(2) Å from the Cu—Cu plane. The Cu-O-Cu bond angle is 103.69(1)°. The crystal structure shows an H-bonded O···N distance of 2.797(4) Å with the counterion which resembles the environment of multinuclear copper metalloproteins with protein residues. Figure 54 shows the crystal structure. Figure 55 shows the crystals of **9** under a microscope.

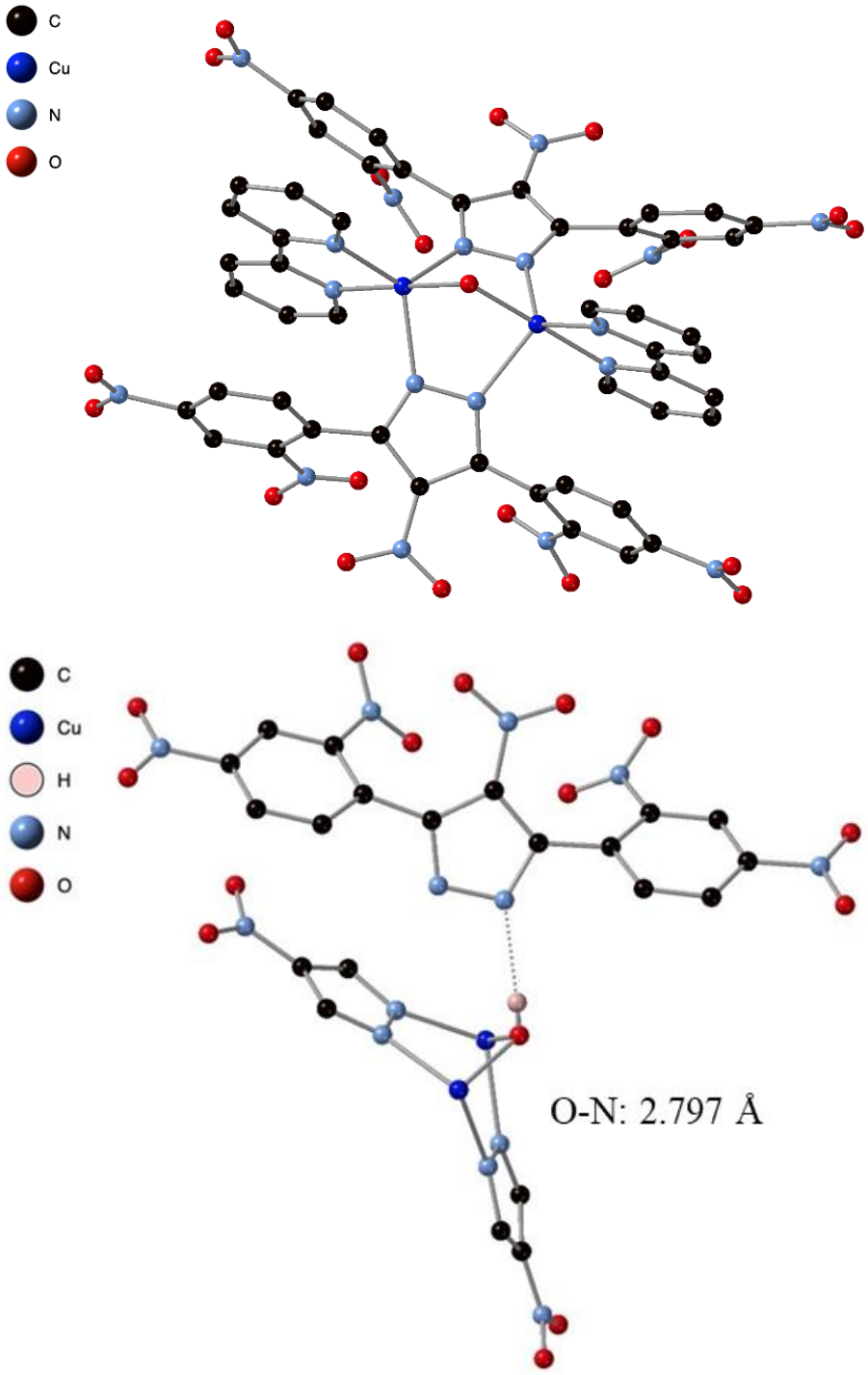

Figure 54. Ball and stick representation of the cationic portion of complex ***9****; H-atoms, and pyrazolate counterion are omitted for clarity (top). H-bonded interaction of complex cation with* $PNpz^-$ *counterion; chelating bipy ligands omitted for clarity (bottom).*

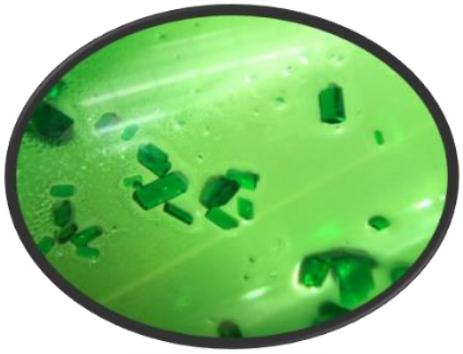

*Figure 55. Crystals of complex **9** under the microscope.*

Complex **10** crystallizes in the triclinic *P*-1 space group with the whole molecule in the asymmetric unit. Cu—N distances of the pyrazolates are 1.997(2) and 1.990(2) Å; 2.039(2) and 2.018(2) Å for the nitrogen atoms of the bipy ligand. The Cu—O distances of the coordinated H_2O are 2.210(2) Å with a hydrogen bond between the coordinated H_2O and a second free H_2O molecule of 2.776 Å. Figure 56 shows the crystal structure of the complex.

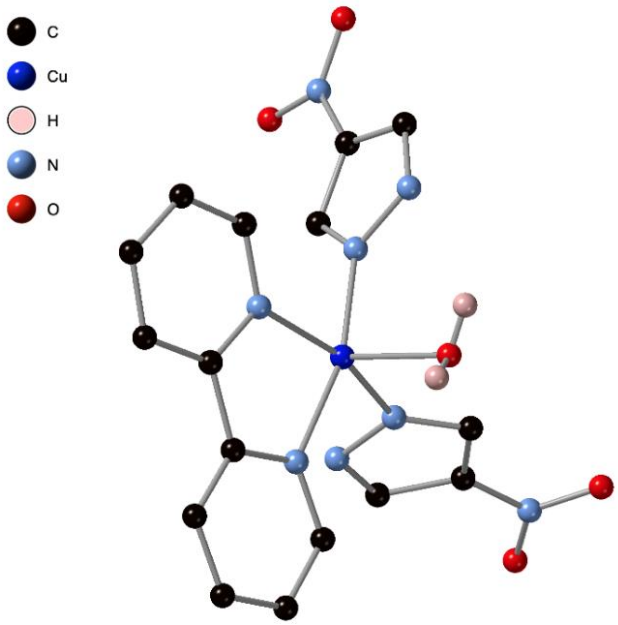

*Figure 56. Ball and stick representation of complex **10**. Phenyl rings on the PNpz$^-$ ligands have been omitted for clarity, hydrogen atoms on the coordinated water molecule have been explicitly shown.*

2.3.3: Summary

A summary of the motifs synthesized, and their properties is shown in Table 11. By comparing the parameters of motifs in this work, to those of similar complexes in the literature, a plot summarizing Cu-Cu distances vs Cu-O-Cu angles can be used to represent the correlation between these parameters and the assignment of oxo *vs.* hydroxo species (Figure 57). What makes the catalytically active complex **9** unique is that it falls somewhere in-between an oxo/hydroxo species, where the resting state is more closely related to a hydroxo complex with a SSI to the anion, and when deprotonated, it results in a reactive, bent-oxo species. Scheme 18-Scheme 20 shows the summary of complexes synthesized in this work.

Table 11. Comparison of select interatomic distance (Å) and angles (°) for the dimeric complexes with a $Cu_2(\mu\text{-}pz)_2$ skeleton in this study.

Entry	Motif	Cu-Cu	Cu-O	Cu-O-Cu	Cu-N (pyrazole)
1	Cu_2	3.372(1)	N/A	N/A	1.971(4)-1.999(3)
2	Cu_2	3.409(1)	N/A	N/A	1.963(4)-1.975(4)
3	$Cu_2(\mu\text{-}O_2DMS)$	3.617(2)	1.894(1), 1.896(9)	N/A	2.064(9)-2.136(1)
4	$Cu_2(\mu\text{-}PNpz)_3$	3.295(3)	N/A	N/A	1.963(8)-2.139(1)
5	Cu_2	3.860(6)	N/A	N/A	2.018(2)-2.221(2)
6	$Cu_2(\mu\text{-}OH)$	2.978(3)	1.943(8), 1.917(7)	100.94(2)	2.069(7)-2.078(7)
7	$Cu_2(\mu\text{-}OMe)$	2.978(4)	1.951(2), 1.944(2)	99.72(7)	2.065(1)-2.079(2)
8	$Cu_2(\mu\text{-}OMe)$	2.980(1)	1.944(2). 1.944(2)	100.06(6)	2.003(4)-2.003(4)
9	$Cu_2(\mu\text{-}OH)$	3.034(1)	1.929(2), 1.929(2)	103.69(1)	2.054(2)-2.122(2)

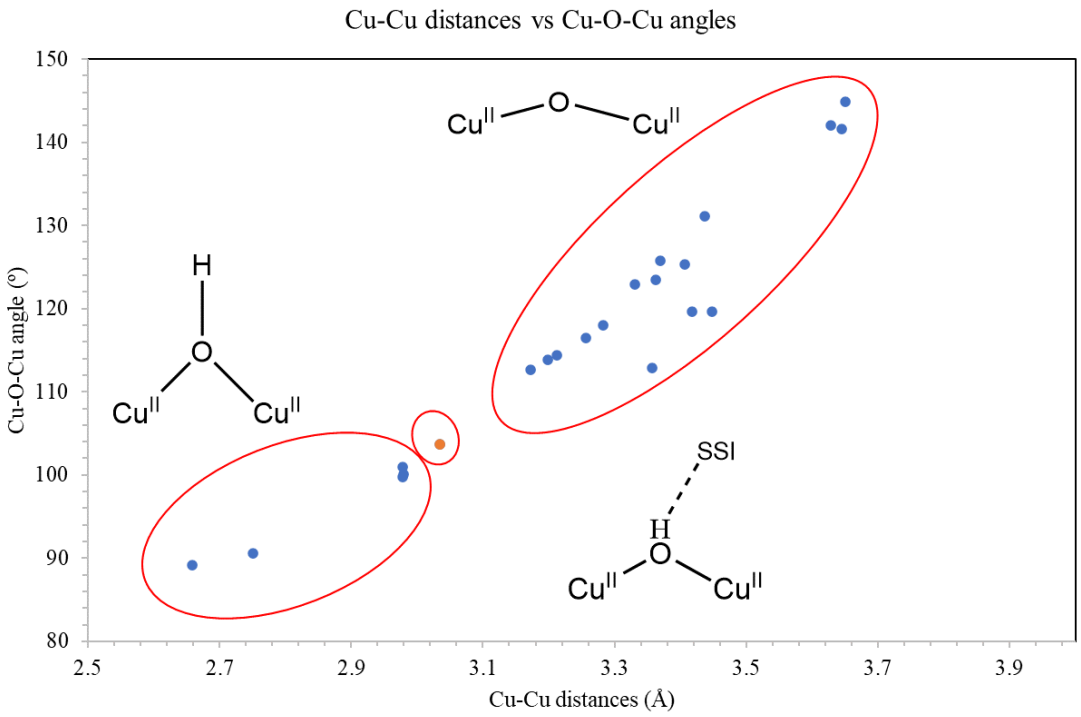

Figure 57. Comparison of oxo vs. hydroxo species. Data plotted from Table 3 (literature search) and Table 11 (this work).

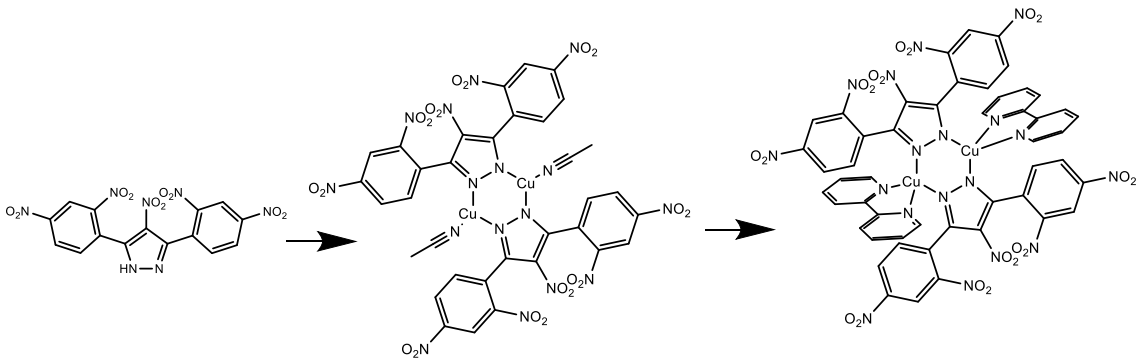

Scheme 18. Summary of complexes synthesized in this study from the PNpzH ligand.

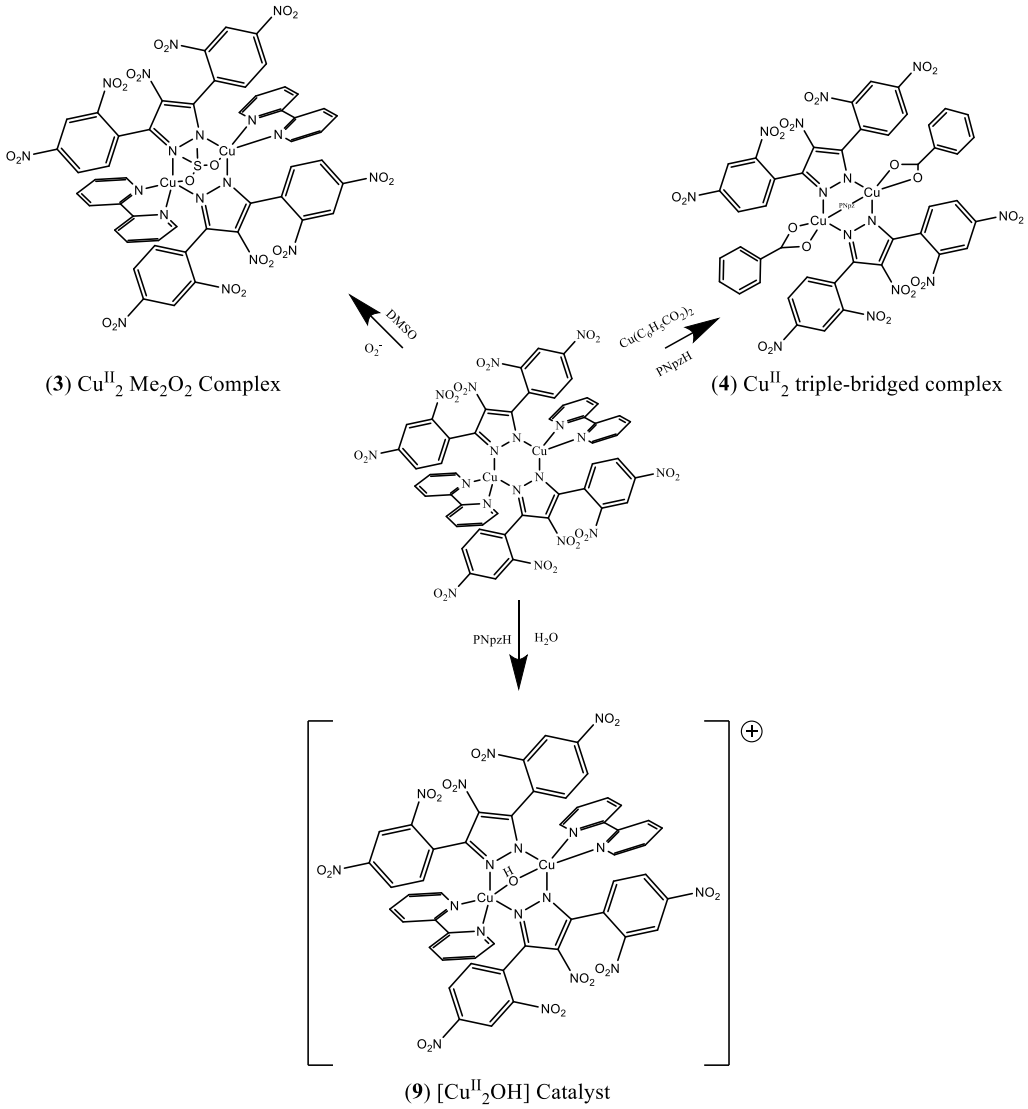

(**3**) Cu^{II}_2 Me_2O_2 Complex

(**4**) Cu^{II}_2 triple-bridged complex

(**9**) [Cu^{II}_2OH] Catalyst

*Scheme 19. Summary of complexes synthesized from complex **2** as a starting material.*

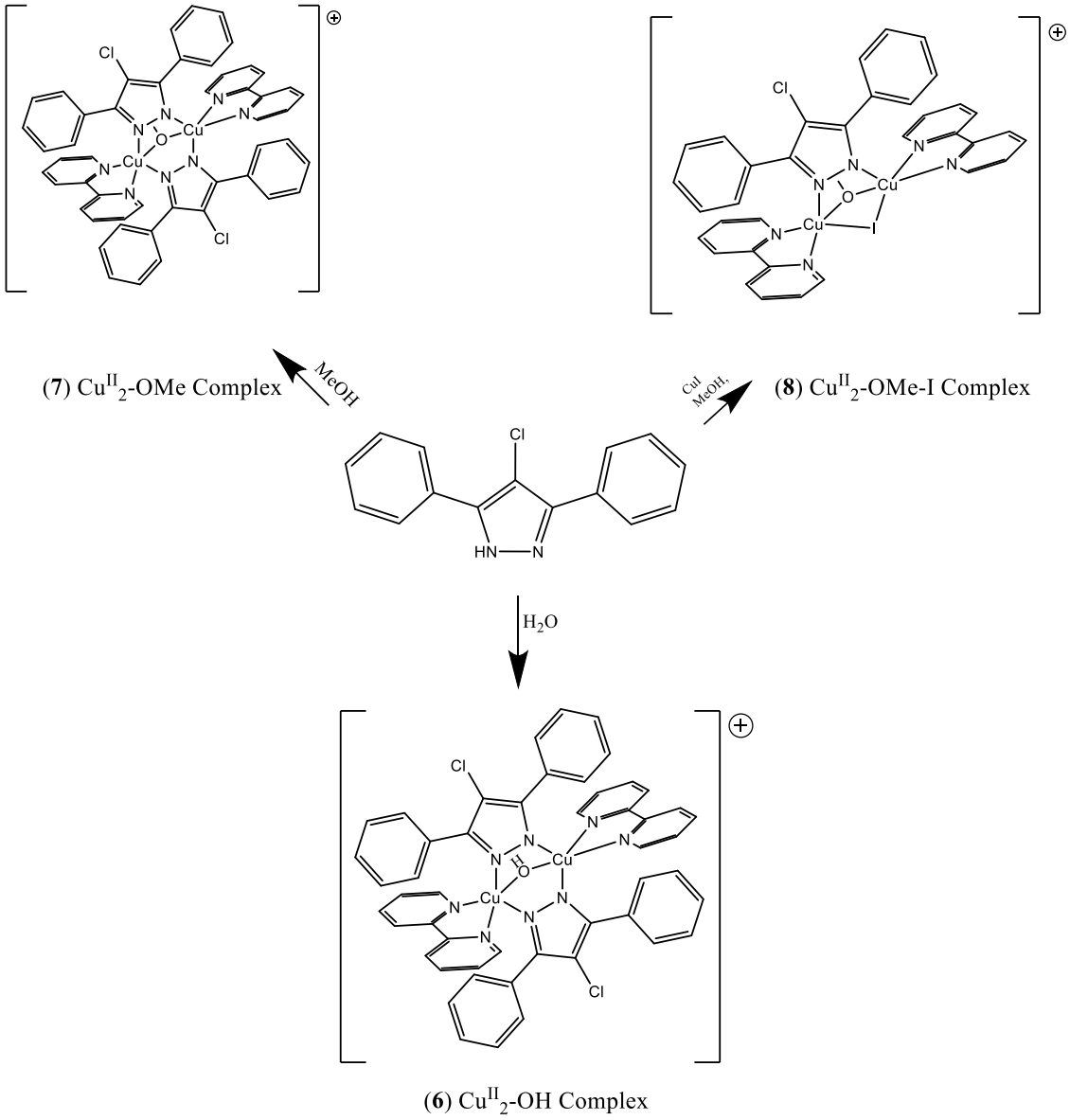

Scheme 20. Summary of complexes synthesized from the 4-Cl-3,5-Ph$_2$-pzH starting material.

2.4.1: Cyclic voltammetry

CV experiments conducted on the PNpzH ligand shows two reversible reduction events with $E_{1/2}$ = -1.32/-1.57 V (*vs.* Fc^+/Fc, Figure 58). The two reduction processes of the Cu^{I}_2 complex **2** at approximately the same redox potential (-1.32 V and -1.58 V, Figure 60), but now with different current intensities and larger separation between forward and reverse waves, are tentatively assigned to the same ligand-based processes as for free PNpzH. The Cu^{II}_2 complex **9** also shows two unequal reduction processes, now cathodically shifted to -1.62 V and -1.87 V (Figure 61), tentatively assigned to PNpz-based processes. In addition to reductions, complex **2** shows oxidation processes at -0.31 V, -0.05 V (irreversible) and 0.23 V, tentatively assigned to Cu-based oxidations (Figure 59). Further electrochemical and spectroscopic studies are required in order to properly probe and assign the electrochemical processes of PNpzH, **2** and **9**.

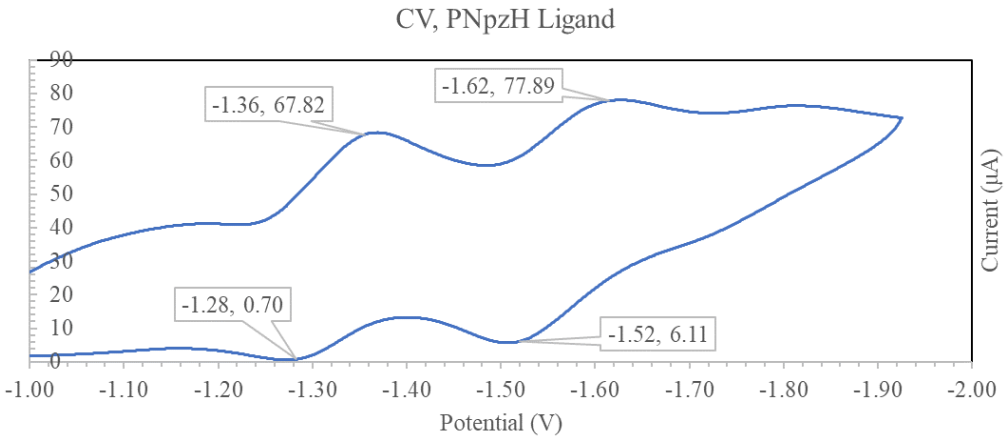

Figure 58. CV voltammogram of the PNpzH ligand (1 mM) in 0.5 M $TBAPF_6$/MeCN, glassy carbon working electrode), vs. Fc^+/Fc, 100 mV scan rate.

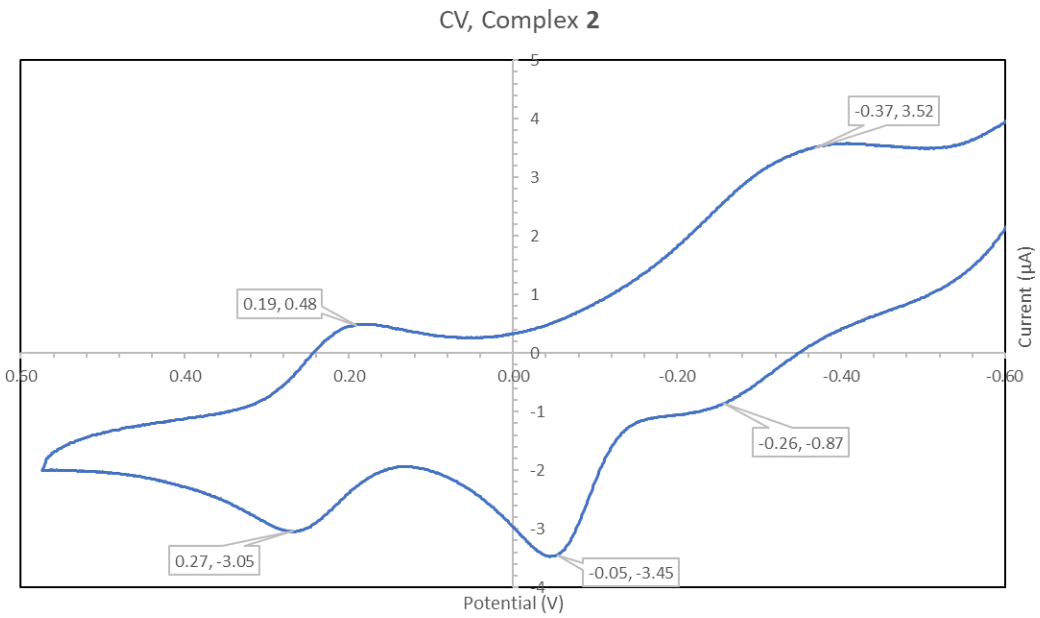

*Figure 59. CV voltammogram of complex **2** (1 mM) in 0.5 M $TBAPF_6$/MeCN, glassy carbon working electrode, vs. Fc^+/Fc), showing Cu-based oxidations, 100 mV scan rate.*

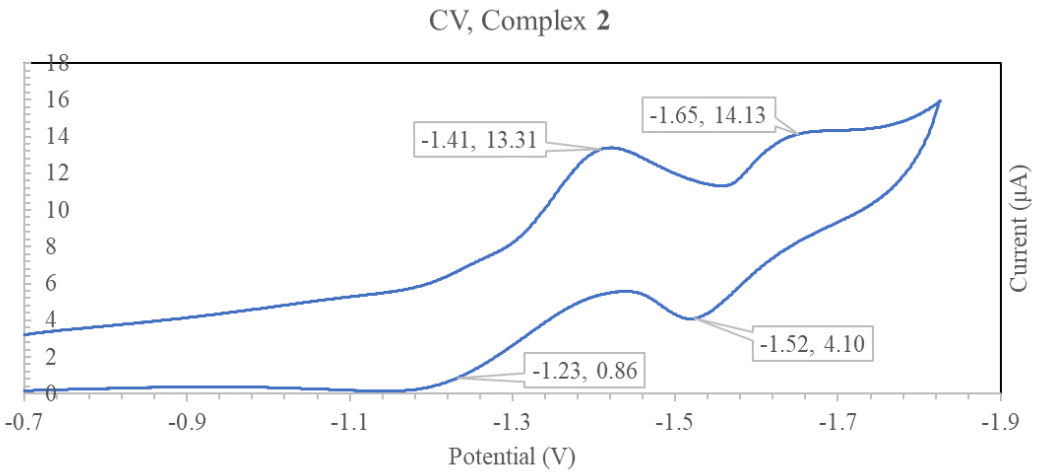

*Figure 60. CV voltammogram of complex **2** (1 mM) in 0.5 M $TBAPF_6$/MeCN, glassy carbon working electrode, vs. Fc^+/Fc), showing ligand-based reductions, 100 mV scan rate.*

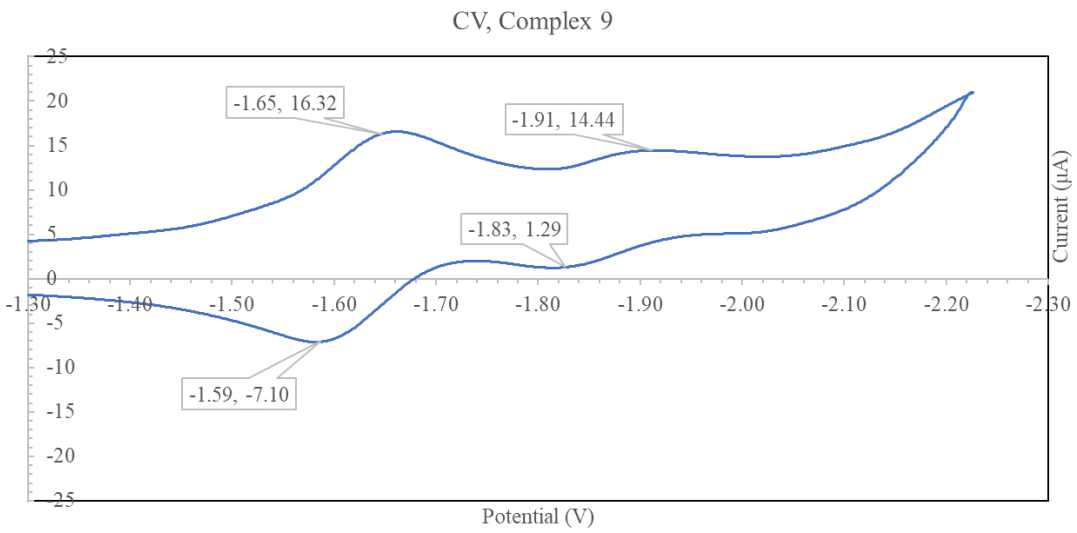

*Figure 61. CV voltammogram of complex **9** (1 mM) in 0.5 M $TBAPF_6$/MeCN, glassy carbon working electrode), vs. Fc^+/Fc, showing ligand-based reductions, 100 mV scan rate.*

Chapter 3: Catalytic oxidation and O-atom transfer studies

3.1: Introduction

Complex **9** was first discovered to be catalytically active by layering of its MeCN solution over toluene (for crystal growth), which resulted in the dark green solution to turn to a red color. The deep red crystals grown from this solution were characterized by SCXRD, matching the unit cell of **2**. Once redissolved in MeCN, the red solution of **2** was set to crystallize by layering over H_2O, where the color once again changed from red to green with deep green crystals of **9** (by unit cell determination) afforded within a week. To further investigate interconversion of **2** and **9**, three qualitative experiments were conducted: (i) To a solution of **9** was added Ph_3P (1:100 stoichiometric excess) in MeCN; within 24 h, a green to red color change was observed, and the presence of Ph_3PO was confirmed by IR (Scheme 21(i)). (ii) The second experiment involved solution of **9** and catechol (1:100 stochiometric excess) in MeCN, where another green to red color change was observed, and the oxidation product, benzoquinone, was confirmed by GC/MS (Scheme 21(ii)). (iii) A 100-fold molar excess of DHA was added to a 10 mL MeCN solution of **9** in sealed flask (i.e., finite oxygen supply) and the reaction was allowed to proceed under stirring at room temperature. Analogous experiments using the similar complexes **6** and **7** instead of **9** did not produce evidence of cycling between the Cu^{I} and Cu^{II} states. No further oxidation products were investigated for at this time, however, it is possible that other oxidation products, such as the corresponding catechol or ketone, could result as they are typical of these types of oxidations [123]. The above qualitative experiments suggested that the presence of the $PNpz^{-}$ counterion is necessary for the catalytic cycle and the pentanitro

substitution of the bridging pyrazolato ligands are also a requirement for the oxidizing properties of compound **9**.

(i)

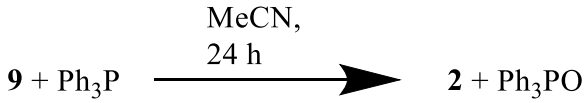

(ii)

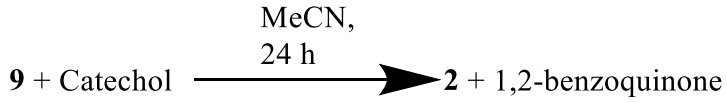

(iii)

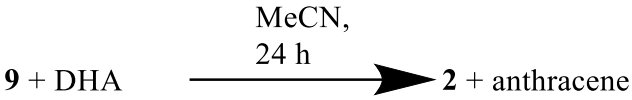

Scheme 21. Reaction conditions for the oxidation of simple substrates. Solvent: MeCN, substrate concentrations: 1 mM, cat. concentration: 0.01 mM.

Turnover numbers and turnover frequencies define a good catalyst, **9** has shown a propensity towards alkane oxidation, as evident by cycling from the green Cu^{II} state to the red Cu^{I} state when left in toluene. Quantitative studies involve stoichiometric experiments to determine TONs and TOFs; Determination of TON are based on known methods and include monitoring the conversion of substrate to product by GCMS/UV-Vis/NMR and adding stoichiometric amounts of substrate (DHA, toluene, etc.), to one molar equivalent of the complex until the reaction stops [124]. Once TON is determined, TOF can be determined by calculating how fast the catalyst works. The typical progression involves the use of easier to oxidize substrates, followed by moving towards harder to oxidize substrates with more complex products (Table 12).

Table 12. Typical substrate progression for oxidation of hydrocarbons.

Entry	Name	Structure	C-H BDE (kJ mol^{-1})
1	9,10-Dihydro-Anthracene	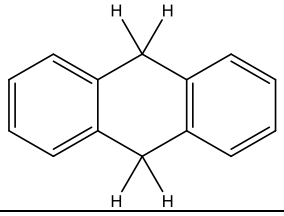	326
2	Toluene	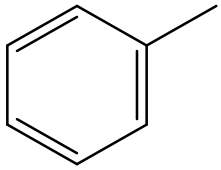	379
3	Cyclohexane	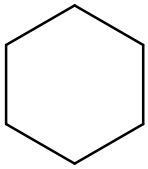	418
4	2,2,4-Trimethyl-Pentane	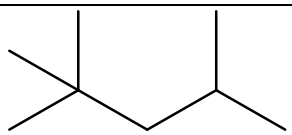	431
5	Methyl-cyclohexane	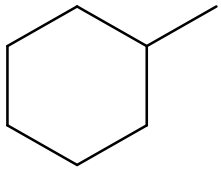	439
6	Methane	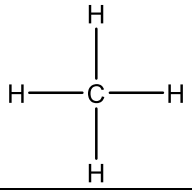	439

3.2: Experimental

3.2.1: Materials and instrumentation

All catalysis experiments were performed with commercially available solvents, purified, and dried according to standard procedures, commercially available substrates (98% pure), and crystals of complex **9**. Products were monitored and confirmed by GC/MS and by GC with standard references. Reactions were carried out under a fume hood in the open air or

under nitrogen in a closed system, as specified by case. GC/MS experiments were run by the advanced mass spec facility at Florida International University. GC-only experiments were run on an Agilent 7890B GC Gas Chromatograph equipped with a PAL DHR Autosampler and an HP5 30mx 0.32mm x 0.25um column.

3.2.2: Catalytic experiments

3.2.2.1: Oxidation of triphenylphosphine

Method A. A 20 mL scintillation vial is charged with 5.0 mg (0.0028 mmol) complex **9** and 73.40 mg (0.28 mmol) PPh_3 and dissolved, under stirring, in 10 mL MeCN. The vial is capped, and the mixture was stirred for 24 h. The solution goes from a light green color to a red color. The reaction mixture was filtered through celite and glass wool to remove unreacted material, and the filtrate set to rotary evaporate, and placed under vacuum for 24 h. FTIR is ran on the orange-red powder.

3.2.2.2: Oxidation of catechol

Method A. A 20 mL scintillation vial is charged with 5.0 mg (0.0028 mmol) complex **9** and 30.82 mg (0.28 mmol) $C_6H_4(OH)_2$ and dissolved, under stirring, in 10 mL MeCN. The vial is capped, and the mixture was stirred for 24 h. The solution goes from a light green color to a red color. The reaction mixture was filtered through celite and glass wool to remove unreacted material. A 1 mL aliquot of the sample is taken for GC/MS analysis.

3.2.2.3: Oxidation of 9,10-dihydroanthracene

Method A. A 20 mL scintillation vial is charged with 5.0 mg (0.0028 mmol) complex **9** and 50.47 mg (0.28 mmol) DHA and dissolved, under stirring, in 10 mL MeCN. The vial is capped, and the mixture was stirred for 48 h. The solution goes from a light green color to a red color. The solution is then opened to atmosphere and allowed to react for an additional 24 h. The reaction mixture was filtered through celite and glass wool to remove unreacted material. A 1 mL aliquot of the sample is taken for GC/MS analysis at t = 48 h and t = 72 h.

Method B. A 20 mL scintillation vial is charged with 5.0 mg (0.0028 mmol) complex **9** and 50.47 mg (0.28 mmol) DHA and dissolved, under stirring, in 10 mL MeCN. The vial is capped, and the mixture was stirred for 24 h. A 1 mL aliquot of the sample is taken for GC analysis at t =1.5 h and t = 24 h. The reaction mixture was filtered through celite and glass wool to remove unreacted material before running through the GC instrument.

3.2.2.4: Oxidation of toluene

Method A. A 20 mL scintillation vial is charged with 5.0 mg (0.0028 mmol) complex **9** and dissolved, under stirring, in 10 mL MeCN/Toluene at 50° C. The vial is capped, and the mixture was stirred for 24 h under reflux. The solution goes from a light green color to a cloudy green color. The reaction mixture was filtered through celite and glass wool to remove unreacted material. Addition of 10 mg (0.18 mmol) NH_4Cl in a separatory funnel result in two

layers, an aqueous and an organic layer. The aqueous layer is removed by conventional methods and a 1 mL aliquot of the sample is taken for GC/MS analysis.

Method B. A 20 mL scintillation vial is charged with 5.0 mg (0.0028 mmol) complex **9** and dissolved, under stirring, in 10 mL MeCN/Toluene at 50° C. The vial is capped, and the mixture was stirred for 24 h under reflux. The solution goes from a light green color to a cloudy green color. The reaction mixture was filtered through celite and glass wool to remove unreacted material. A 1 mL aliquot of the sample is taken for GC analysis.

3.2.2.5: Oxidation of cyclohexane

Method A. A 20 mL scintillation vial is charged with 5.0 mg (0.0028 mmol) complex **9** and dissolved, under stirring, in 10 mL MeCN/THF at rt. 2 mL cyclohexane is added to the solution. The vial is capped, and the mixture was stirred for 24 h. The solution goes from a light green color to a dark yellow color. The reaction mixture was filtered through celite and glass wool to remove unreacted material. A 1 mL aliquot of the sample is taken for GC/MS analysis.

3.2.2.6: Oxidation of cyclohexene

Method A. A 20 mL scintillation vial is charged with 5.0 mg (0.0028 mmol) complex **9** and dissolved, under stirring, in 10 mL MeCN/THF at rt. 2 mL cyclohexene is added to the solution. The vial is capped, and the mixture was stirred for 24 h. The solution goes from a light green color to a pale-

yellow color. The reaction mixture was filtered through celite and glass wool to remove unreacted material. A 1 mL aliquot of the sample is taken for GC/MS analysis.

3.3: Results and discussion

3.3.1: Oxidations of PPh_3 and catechol

Complex **9** has shown a propensity towards alkane oxidation and O-atom transfer chemistry as evident by the trivial oxidations of catechol and triphenyl phosphine towards benzoquinone and triphenyl phosphine oxide respectively. Catechol which has a BDE of 348 KJ mol^{-1}, was easily converted to the respective quinone and showed proof of concept that **9** is indeed capable of oxidation reactions analogous to those carried out in Nature by oxidases [125]. Likewise, the oxidation of triphenyl phosphine to triphenyl phosphine oxide showed that the catalyst is also capable of oxygenation reactions.

3.3.2: Oxidation of DHA

The oxidation of DHA to anthracene was investigated by reacting complex **9** with excess DHA in MeCN in a closed environment. As time progressed, the solution went from the dark green color of the Cu^{II} species **9** to the red color of the corresponding Cu^{I} (**2**), indicating that with no more oxygen available, oxidation has ceased, at this point a 1 mL aliquot sample was taken for GC/MS analysis. The flask was then opened to atmosphere, and the fresh supply of O_2 turned the solution from a red to a pale green color, indicating that the catalyst had been regenerated from the Cu^{I}_2 species back to the active Cu^{II}_2OH (Figure 62). After the reaction was allowed to progress for a further 24 h, a 1 mL aliquot was taken for GC analysis, confirming the formation of anthracene (Figure 63). A peak

matching the retention time and fragmentation pattern for anthracene was detected with a total of 96.3% certainty, showing that the catalyst is indeed capable of oxidizing DHA.

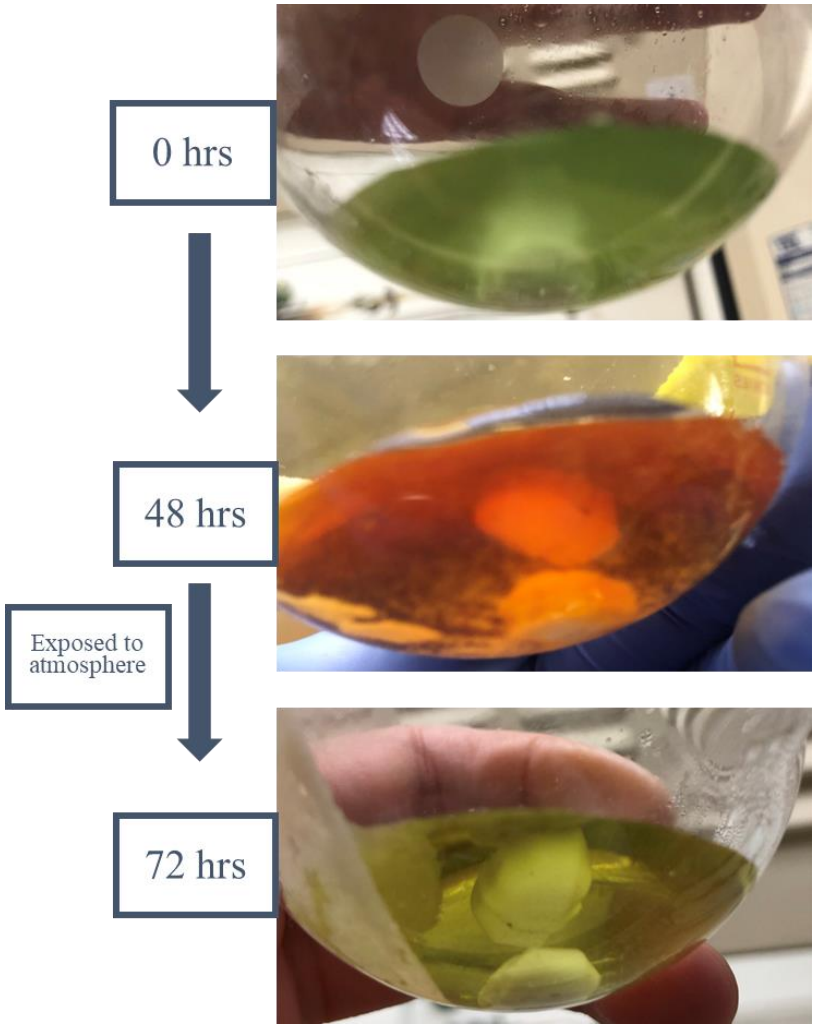

*Figure 62. Color progression of the reaction between complex **9** and substrate(s). Solvent: MeCN, substrate concentration: 1 mM, cat. concentration: 0.01 mM. The system was flushed with nitrogen followed by bubbling of the solution with nitrogen for 5 mins before being sealed off.*

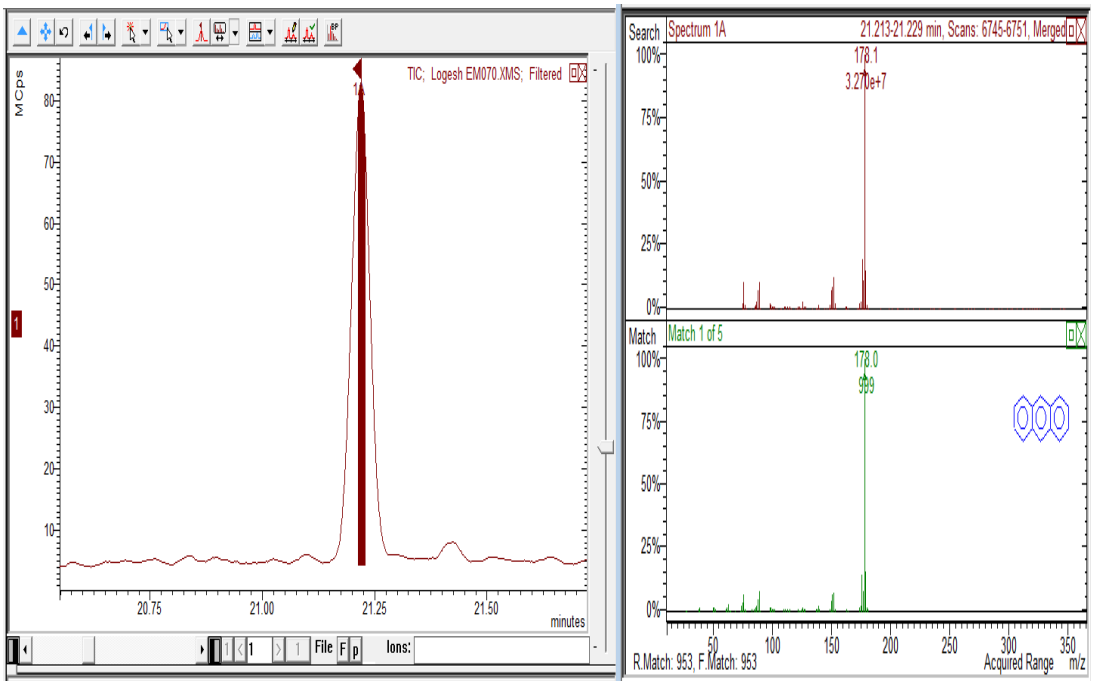

Figure 63. GC retention time for anthracene (1), MS pattern for anthracene (1A). Solvent: MeCN, substrate concentration: 1 mM, cat. concentration: 0.01 mM.

The oxidation of DHA to anthracene is a two-electron process which reduces complex **9** to complex **2**. The cycle requires an input of ½ O_2 molecule per molecule of DHA. Scheme 22 shows the proposed mechanism for the oxidation of anthracene.

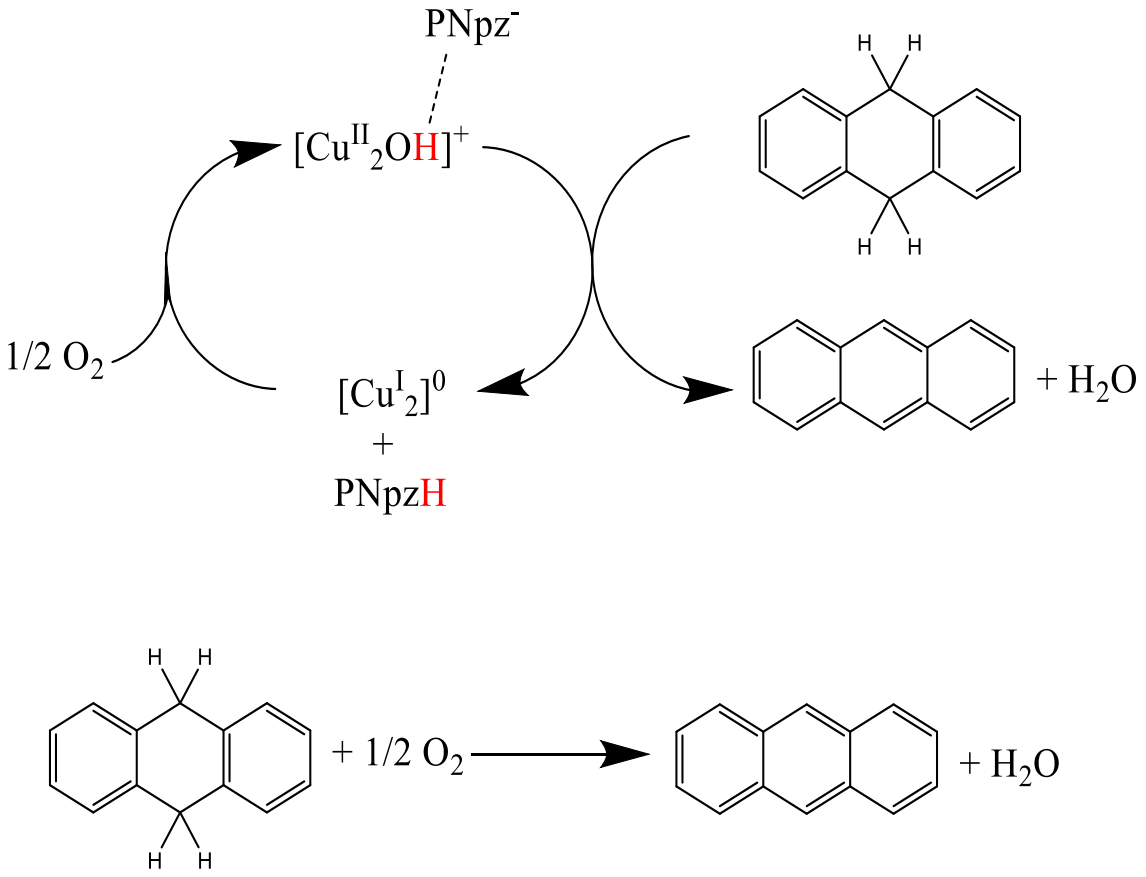

Scheme 22. Proposed catalytic cycle of ***9****, oxidation of DHA to anthracene.*

Literature research indicated that anthracene was capable of further oxidations, to the diquinone product. A second experiment with 100-fold excess of DHA was added to a flask containing 10 mL of MeCN and 1 equivalent of catalyst. The reaction was stirred at room temperature open to the atmosphere, with aliquots withdrawn at 1.5 and 24 h for GC measurements. At 24 hours, the ratio of the compounds detected was 49.94% (A): 26.67%

(B): 20.32% (D), totaling 96.93%. Scheme 23 shows the progression of oxidation products for DHA. The presence of products B and D were confirmed by their retention time and compared to matching standards. Product C was not detected by GC, as it likely undergoes oxidation quickly towards product D (the oxidation of B is the rate determining step), however it is an undisputable intermediate, as the reaction of B to D requires a four-electron transfer.

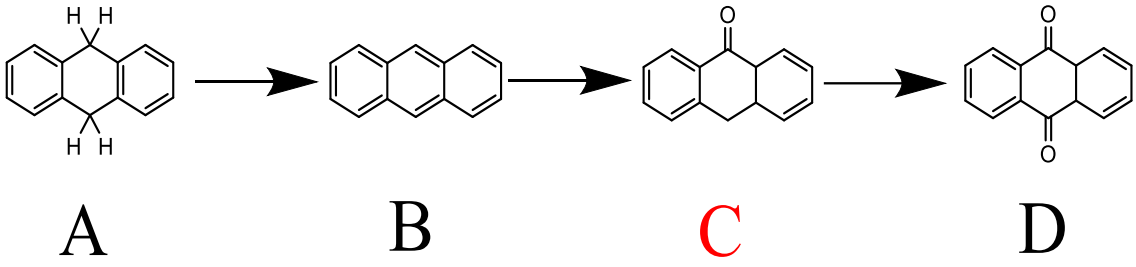

Scheme 23. Oxidation products for DHA substrate.

Turn-over-numbers in this reaction are calculated by Equation 1. From A to B, it is a one-cycle oxidation, from B to C it is a second one cycle-oxidation (two cycles total from A), and from C to D it is a last one-cycle oxidation (three cycles total from A).

Equation 1

$$TON = \frac{Mole\ (product)}{Mole\ [\mathbf{9}]}$$

As the reaction is not as simple as substrate → product(s) the determination of its TON assumes that the first turnover produces B, a second turnover produces C and a third one one generates the final product D. This means that the total number of cycles that produced $B_{initial}$ can be measured by $A_{inital} - A_{final}$ = ~50.1; the total number of cycles that produced $C_{initial} = B_{inital} - B_{final} = (A_{inital} - A_{final}) - B_{final}$ = ~23.4; and as no product C was detected in the product mixture, $D_{final} = C_{initial}$ = ~23.4. Equation 2 calculates the total TON for this

catalyst. The termination of the catalytic process is tentatively attributed to catalyst poisoning.

Equation 2

$$TON = \frac{Mole\ (A_i - A_f) + 2(B_i - B_f)}{Mole\ [\mathbf{9}]} = 96.9$$

3.3.3: Oxidation of toluene

The oxidation of toluene was revisited in greater detail, where complex **9** was reacted with toluene and successful oxidation to benzaldehyde and benzyl alcohol was achieved, as characterized by GCMS. Two peaks matching the retention times and molecular weight fragmentation patterns for the oxidized substrates were recorded. The peak observed at ~7 min matched benzaldehyde with an 85% certainty, and the peak at ~8.5 min corresponds to benzyl alcohol with an 87% match based on retention times and mass spectroscopic fragmentation pattern. Qualitatively, almost four times as much concentration of benzaldehyde was observed than benzyl alcohol. This implies that toluene is first oxidized to benzyl alcohol, after which further oxidation to the aldehyde proceeds faster. The even further oxidation of benzaldehyde to benzoic acid, however, was not detected [126]. As benzoic acid was not observed, it can be suggested that this system can selectively oxidize toluene into the corresponding aldehyde, an industrially significant precursor for various pharmaceuticals. Alternatively, the absence of benzoic acid can be attributed to reaction with the catalyst, forming (catalytically inert) copper benzoate, which is not detectable by GC.

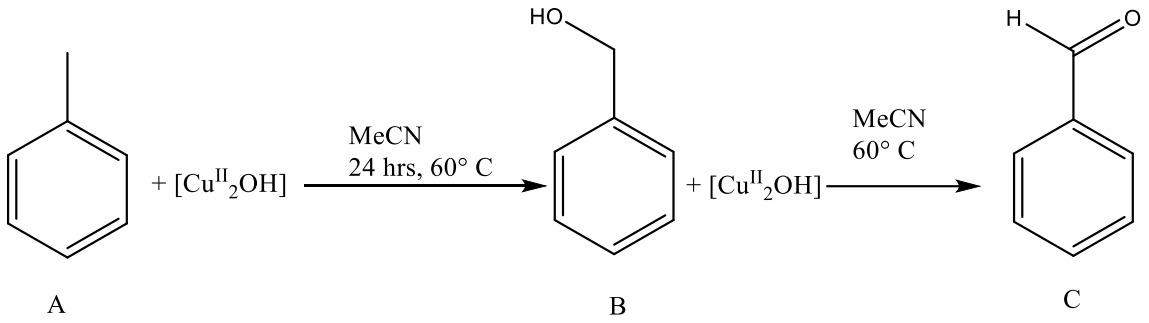

Scheme 24. Oxidation of toluene to benzyl alcohol and benzaldehyde.

The oxidation of toluene to benzyl alcohol and benzaldehyde follows a similar pattern to the oxidation of DHA, where the substrate is first oxidized to a product that is even more favorable towards oxidation by the catalyst and can cycle through towards a second oxidation product. Toluene's sp^3 C-H bond is oxygenated to a primary alcohol, which can then react with the catalyst to undergo a second oxidation to an aldehyde. Equation 1 can be applied to the oxidation of toluene to produce Equation 3, where substrate A is converted to product B, and product B is further converted to product C. As almost all of product B goes to product C (>90%), TON can be easily estimated by doubling the amount of product C.

Equation 3

$$TON = \frac{Mole\,(A_i - A_f) + (B_i - B_f)}{Mole\,[\mathbf{9}]} \qquad TON = \frac{Mole\,(2C)}{Mole\,[\mathbf{9}]}$$

Scheme 25 shows the proposed mechanism for the oxidation of toluene. When the H-bonded pyrazole moves from the catalyst, possibly by the introduction of the substrate [127], the catalyst enters the active state where toluene is oxidized via a two-electron pathway to benzyl alcohol, as the catalyst is regenerated from the Cu^{I}_2 species back to the Cu^{II}_2OH species by an input of ½ O_2, a second consecutive two-electron oxidation can

occur whereby benzyl alcohol is oxidized to its aldehyde counterpart. The overall reaction is thus toluene and oxygen being converted to benzaldehyde and water.

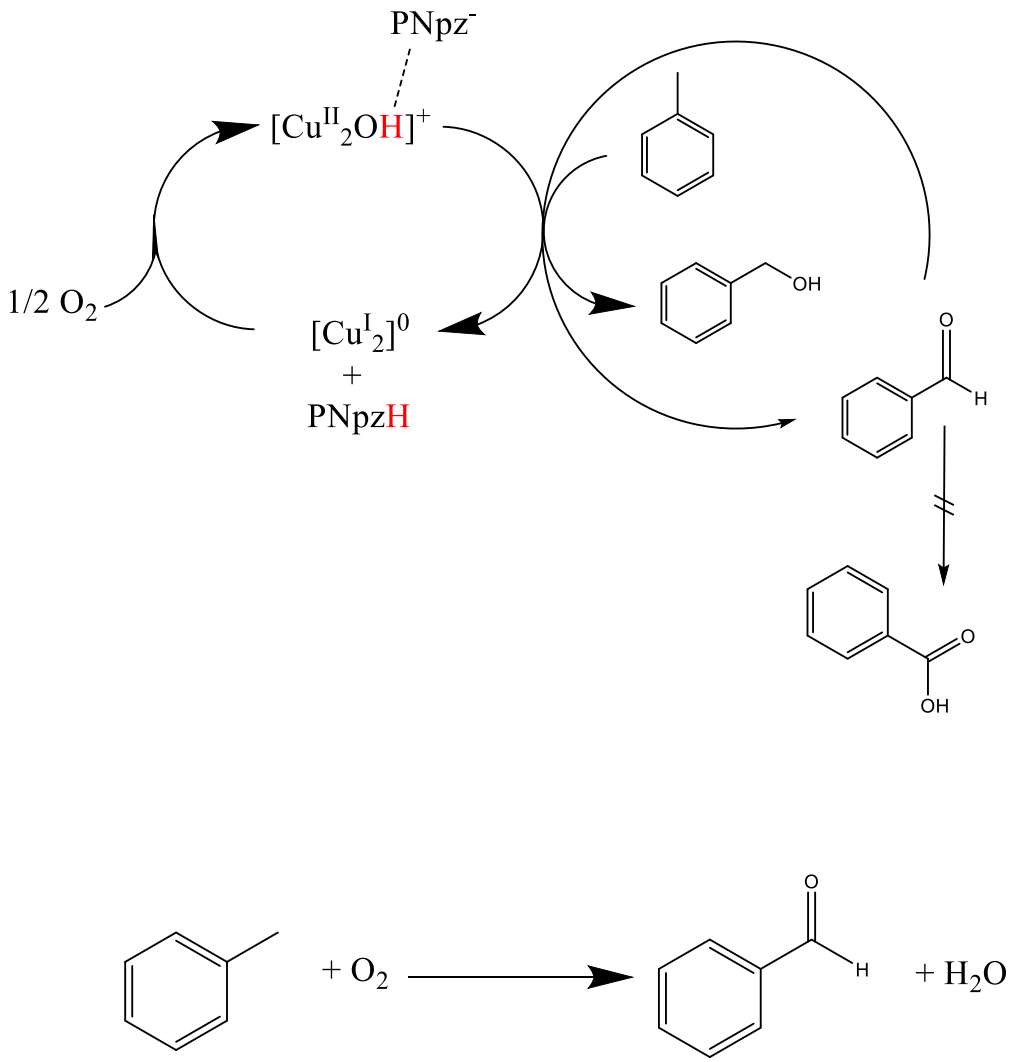

Scheme 25. Proposed catalytic oxidation scheme for toluene.

3.3.4: Oxidation of cyclohexane

The oxidation of cyclohexane (Scheme 20) proved to be more challenging than the previous two, due to the low solubility of the catalyst (in cyclohexane) and the immiscibility of MeCN and cyclohexene. This problem was overcome by the addition of a small amount of tetrahydrofuran. The sample submitted for GC/MS analysis found peaks

that matched cyclohexanol, proving that the complex was indeed capable of oxidation. However, several other oxidation products were found as well, including some products that can be attributed to the oxidation of THF. The list of peaks detected by GC/MS includes: cyclohexanol, cyclohexanone, 1,6-hexanediol, and 4-hydroxybutanoic acid. Cyclohexanol and cyclohexanone make sense as oxidation products of cyclohexane with the catalyst exhibiting similar behavior with toluene, however, 1,6-hexanediol and 4-hydroxybutanoic acid on the other hand, requires significant further investigation, as it is not only an oxygen transfer, but a C-C cleavage and ring opening event as well, with 4-hydroxybutanoic acid as a product of the oxidation of the THF solvent. Such ROEs are typically exclusive to more specialized catalysts of the second and third row transition metals, such as iridium [128]. The major products are the alcohol and the ketone, with the ROE's being the lesser products (<5%). Nevertheless, the successful oxidation of cyclohexene shows that this catalyst has the potential to oxidize methane, as the bond dissociation energies for the two are quite similar, with only a difference of 1 kcal/mol.

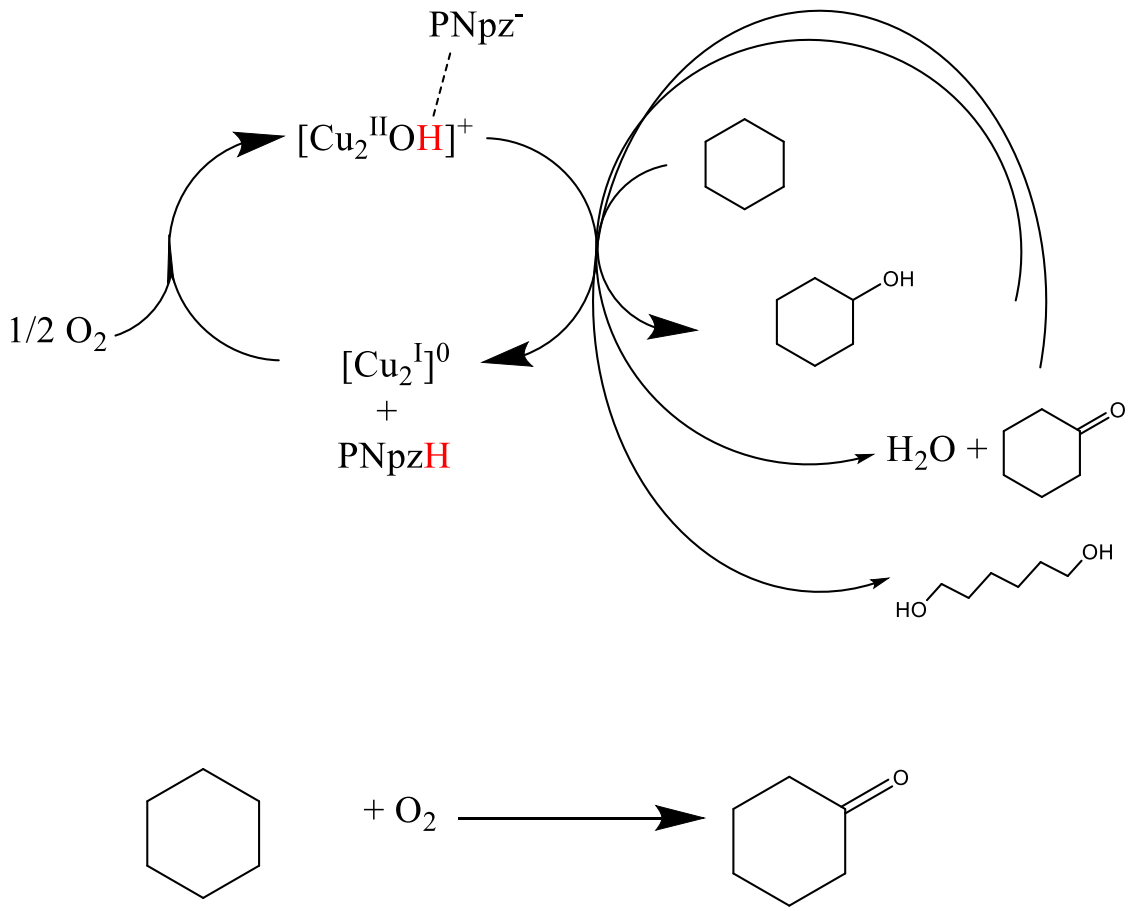

Scheme 26. Proposed catalytic oxidation scheme for cyclohexane.

The two major products, cyclohexanol and cyclohexanone, account for 95% of the oxidation products produced in this reaction (Scheme 27), as such Equation 1 can be applied to give Equation 4 to determine the TON of the desired products.

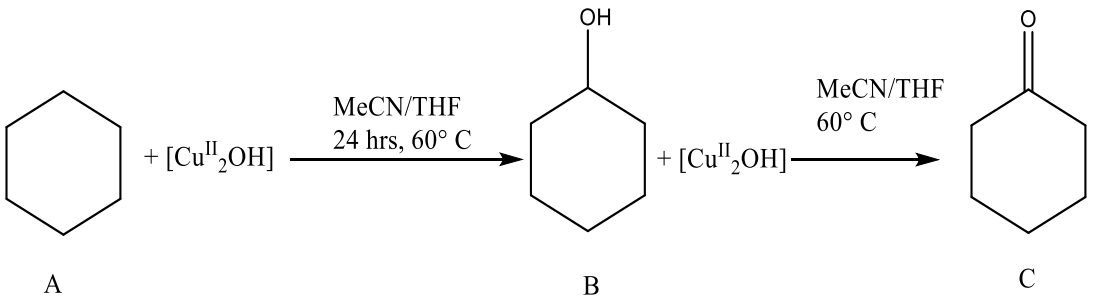

Scheme 27. Oxidation of cyclohexane to cyclohexanol and cyclohexanone, showing the two major products, cyclohexanol and cyclohexanone.

Equation 4

$$TON = \frac{Mole\ (A_i - A_f) + (B_i - B_f)}{Mole\ [\mathbf{9}]}$$

3.3.5: Oxidation of cyclohexene

The oxidation of cyclohexene also required THF to facilitate miscibility with complex **9** in MeCN. The catalyst was indeed able to oxidize cyclohexene, similarly to cyclohexane, with two products detected by GCMS, cyclohexen-1-ol, and cyclohexanone, both are a straightforward two-electron oxygenation reaction. However, it is likely that the substrate is first oxidized to the enol, which can undergo tautomerization to the ketone, as it is the more thermodynamically stable species, with the presence of the enol being detectable only by GC. This type of substrate is also known to undergo epoxidation to give cyclohexene oxide and should not be ruled out as a possible, undetected here, intermediate of the oxidation process [129]. Scheme 28 shows the proposed catalytic cycle where cyclohexene is oxidized to cyclohexenol/cyclohexanone as the catalyst is reduced to the $[Cu^{I}_2]$ state. Equation 1 can be applied to this reaction to give Equation 5, where it's a simple A → B + C TON calculation, as substrate A gives products B and C only.

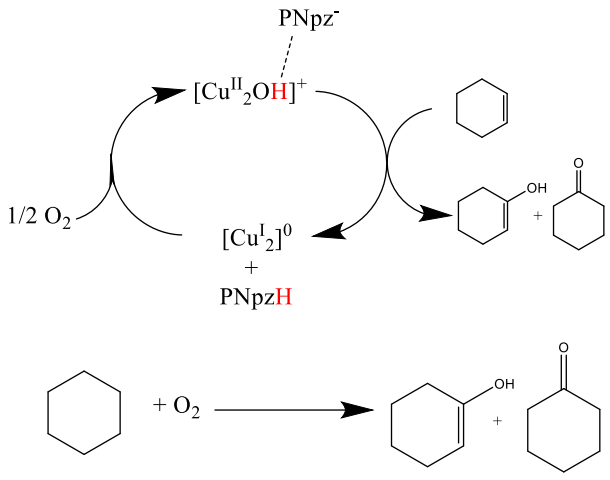

Scheme 28. Proposed catalytic oxidation scheme for cyclohexene.

Equation 5

$$TON = \frac{Mole(B) + Mole(C)}{Mole}$$ [9]

3.3.6: Summary

Table 13 shows the substrates employed in this study, in order of increasing BDE's and their consecutive oxidation products.

Table 13. Substrates used in this study and oxidation products observed. Products were monitored by GCMS.

Entry	First Oxidation	Second Oxidation	Third Oxidation
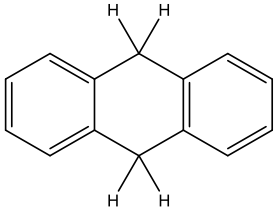 9,10-Dihydro-Anthracene	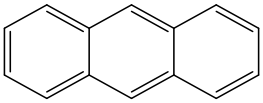 Anthracene	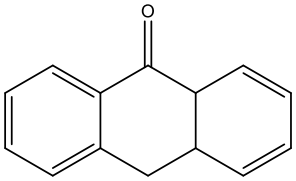 Anthrone	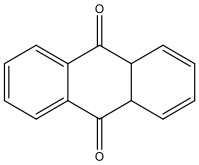 Benzoquinone
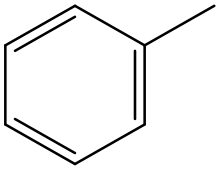 Toluene	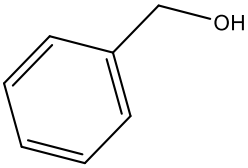 Benzyl alcohol	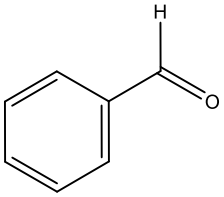 Benzaldehyde	
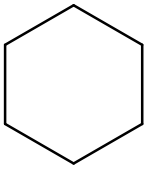 Cyclohexane	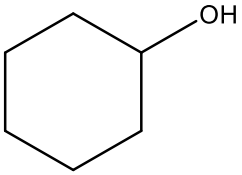 Cyclohexanol	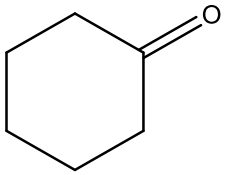 Cyclohexanone	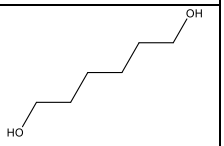 1,6-hexanediol
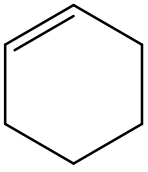 Cyclohexene	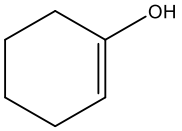 Cyclohexen-1-ol 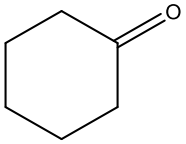 Cyclohexanone		

3.4: Catalytic mechanism

In general, there are two major mechanisms by which catalysis by metal complexes is initiated: a radical induced mechanism, or through a coordination mechanism [130]. In order to investigate the possibility of a radical mechanism, a free radical trap, like (2,2,6,6-tetramethylpiperidin-1-yl)oxidanyl (TEMPO), or the stable aminoxyl radical (best known as a radical marker for EPR), can be used. TEMPO also plays a crucial role as a radical scavenger capable of marking radicals in mass spectrometry [131]. By reacting **9** with substrate and adding in a small amount of TEMPO, a radical reaction should not proceed. This was not the case in the experiment conducted, as the expected oxidation products were indeed confirmed by GC/MS. A second experiment was also conducted with the use of terephthalic acid (TPA) as an OH radical scavenger as proposed by Pintar *et. al* [132]. By reacting **9** with substrate and adding in TPA, if OH radicals were indeed being generated, TPA would become 2-hydroxyterephthalic acid (TPAOH) and can easily be confirmed by fluorescence spectroscopy. Once again, however, the reaction proceeded towards completion and no fluorescent compounds were detected. With the results of the two simple experiments conducted, it was hypothesized that **9** likely proceeds through the coordination mechanism. Therefore, the following mechanism is hypothesized: In the resting state, the catalyst is stabilized by the pyrazolato counterion H-bonded to the hydroxide bridge. The dynamic equilibrium between the μ-OH and reactive μ-O initiates the process by allowing the activation of a C-H bond via interaction with Cu-O to produce an intermediate species, followed by O-atom transfer to the substrate and reoxidation of

the Cu^{I}_2 by dioxygen. A similar cycle is hypothesized for the subsequent oxidation steps. The $PNpz^-$ anion serves as a H^+ storage site during the process (Scheme 29).

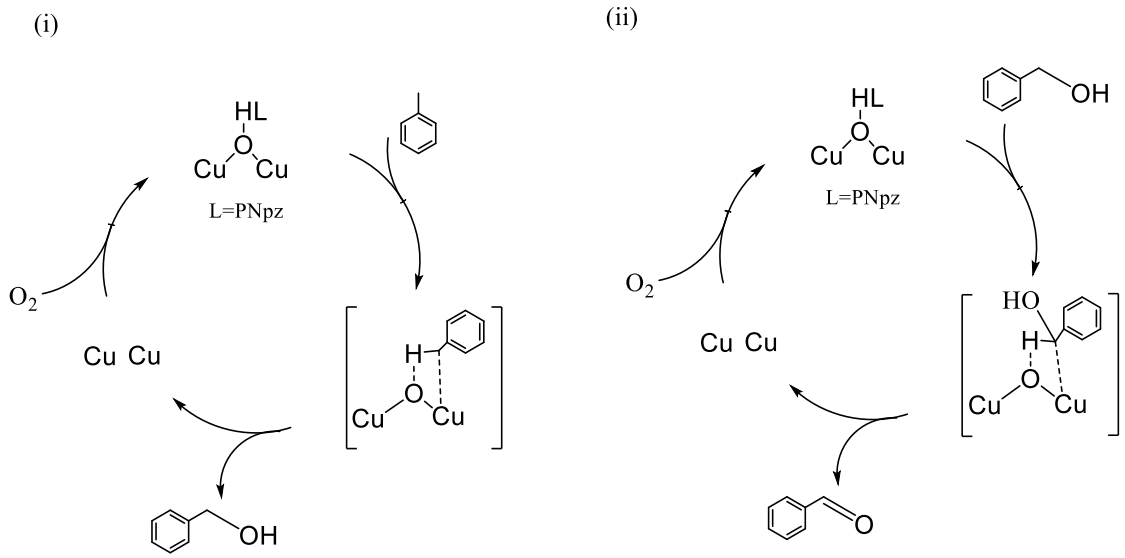

Scheme 29. Working hypothesis for the mechanism of the oxidation of toluene to benzyl alcohol (i) and benzaldehyde (ii).

3.5: Kinetics studies

Kinetics studies conducted on the **9** with DHA have shone light into the reaction mechanism and dynamics of the system. A 1 mM solution of DHA in acetonitrile was charged with 10 μM complex **9** (100:1) under stirring and the UV-Vis absorptions at 264 nm (corresponding to DHA), 364 nm (corresponding to anthracene) and 520 nm (likely further oxidized products) were recorded every 5 s for 10 min. Figure 64 shows the possible products, with purpurin and alizarin specifically have absorbance maximums between 500-600 nm, and are a result of further oxidations of anthraquinone, making them prime suspects [133].

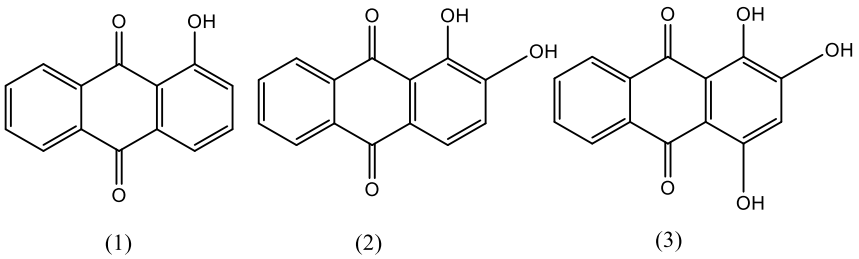

Figure 64. Possible oxidation products of anthraquinone, (1), 2-hydroxo-9,10-anthrquinone, (2) Alizarin, (3) Purpurin.

The absorbance vs. time plots (Figure 65) show the concentrations of A and B decreasing, as substrates are converted into products, and the first oxidation product undergoes further oxidation. Under the constraints of the experiment employed, it is likely that some amount of initial substrate was already converted to anthracene at t = 0, as the initial concentration of anthracene was not zero. The expected rate law for the reaction is a pseudo-first order rate law where the rate is dependent on the concentration of substrate, however, the true rate law for the reaction should be a second order one, dependent on both the concentration of the substrate and catalyst.

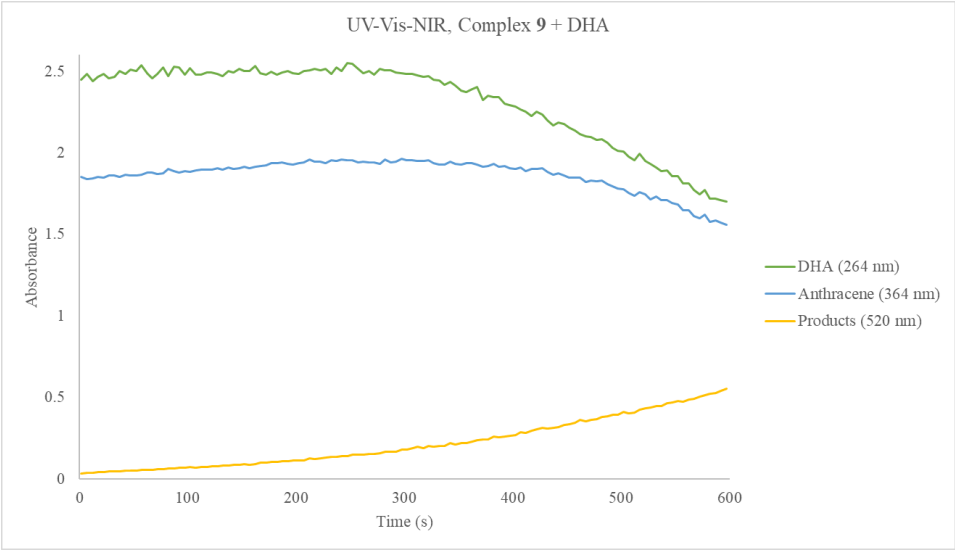

*Figure 65.UV-Vis kinetics of the reaction of complex **9** and DHA (1 mM/MeCN DHA, 0.01 mM/MeCN cat., quartz cuvette).*

Stopped-flow spectroscopy can be employed to gain insights into the first few seconds of the reaction and provide a much more accurate window into the initial rate laws. The reaction should also be conducted under ideal settings: (1) a pure O_2 atmosphere to remove possible interference from moisture in the air, (2) under dry solvents and high purity substrate/catalyst, and (3) under different pressure/heat conditions to investigate the equilibrium of the reaction through Le Chatelier's principle.

3.6: Conclusions

The substrates in this work include varying degrees of sp hybridization, increasingly higher BDE's, and industrial significance. DHA's two C-H bonds at the 9,10 positions with BDE's that are 20% weaker than typical alkane C-H bonds (326 kJ/mol, 78 kcal/mol), coupled with the relative easiness of characterization of the oxidation products, made it an ideal starting point to map out the catalytic processes of complex **9**. The oxidations of DHA and its products are industrially significant (as precursors to larger macromolecules) and have been studied vigorously, providing a font of literature data to analyze. The first oxidation product, anthracene, was easily detectable by the differences in boiling points, polarity, and molecular mass in GC/MS experiments. Anthracene, while being a relatively stable aromatic species, can undergo nucleophilic substitution (O-atom transfer in this case) to form anthrone, the second oxidation product (319 kJ/mol, 76.4 kcal/mol) [134]. Anthrone, while not detected by GC experiments in this study, is certainly easier to oxidize to the diquinone product. It is likely that the first oxidation event (DHA → anthracene), is the rate limiting step. The major conclusions that can be drawn from the catalytic oxidation of DHA by complex **9** are: (1) oxidation of both aliphatic and aromatic C-H bonds is

possible, (2) **9** is capable of both oxygenation (O^{2-} transfer) and oxidation catalysis, (3) insights into the kinetics and mechanisms of **9**. The second substrate, toluene, is a more industrially significant application due to (1) the inertness of terminal C-H bonds, and (2) the pharmaceutical importance of the oxidation products (benzyl alcohol and benzaldehyde) as starting materials. The major conclusions from the oxidation of toluene are: (1) complex **9** can tackle more difficult substrates (379 vs 326 kJ/mol; 16% increase in BDE) at mild conditions, (2) some degree of selectivity is observed as the overoxidation to benzoic acid was not detected, (3) insights into the mechanism by which the complex operates. The current working theory is that complexation of the terminal C-atom to one of the Cu centers leads to an agnostic interaction between the deprotonated bent μ-oxo of the complex and an α-H-atom on the substrate, leads to O^{2-} transfer to the substrate, and a reduction of the Cu^{II} centers to Cu^{I}. Lastly, there are the substrates cyclohexane and cyclohexene, which represent BDEs of 418 and 438 kJ/mol (100, 104 kcal/mol), the toughest C-H bonds to overcome in this study. The oxidation products included some fascinating results, where a ROE was observed at low yields to produce 1,6-hexanediol.

Chapter 4: Copper oxalate complex

4.1: Introduction

Carbon dioxide (CO_2) is an abundant, natural product which plays an important role in the photosynthesis of plants and some microorganisms [135]. Despite the critical role CO_2 plays for life on Earth, it also has an adverse effect on climate change and global warming, with anthropogenic sources such as industrial processes, livestock, and transportation, linked directly to overall human wellness and nutrition [136]. Reduction of CO_2 to a more industrially useful form remains a challenge due to the high thermal and kinetic stability of the C=O bond. Figure 66 shows the molecular orbital diagram of CO_2 containing sp-c hybridization. In a lab setting, reduction of CO_2 is typically achievable via electrochemical reduction in the presence of transition metal catalysts [137]. This requires large amounts of energy and/or powerful reducing agents, and as such, are not yet an economically feasible option for largescale efforts.

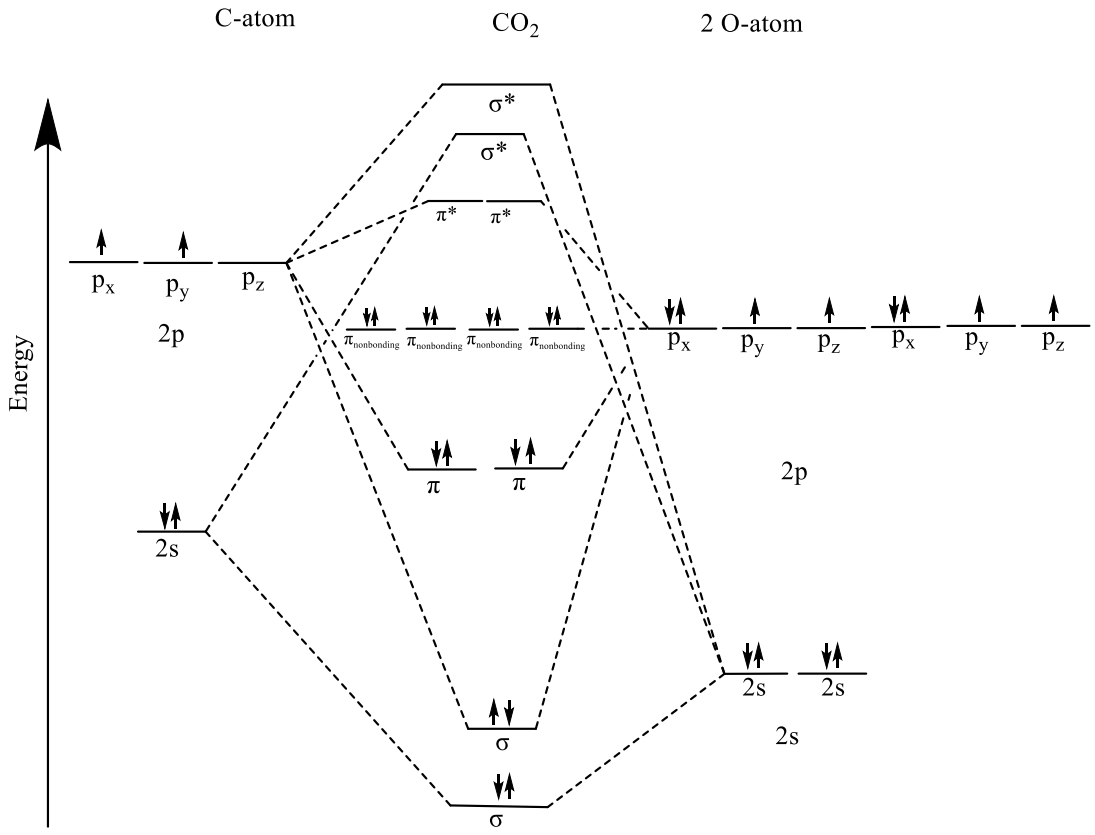

Figure 66. Molecular orbital diagram for the formation of CO_2.

CO_2 emissions, specifically with regards to human activity have been a hot topic for debate, as the accumulation of the greenhouse gas has been a primary driver for climate change and global warming since the start of the industrial revolution [138]. Removal of CO_2 is typically accomplished by three routes: (1) decarbonization, (2) carbon sequestration, and (3) carbon recycling. Despite the advances achieved in the renewables sector, there remain significant challenges to reach full decarbonization, especially within the transport sector, where there currently is no convenient, feasible alternative as of yet. Lastly, while possible in the energy and transport sector, as much as 12% of global emissions are results of indirect industrial processes, manufacturing key products; cement, plastics, steel, ammonia, etc., and while certainly possible to decarbonize (some of) these key industries,

it is unlikely that net-zero emissions will be reached in the near future [139]. Carbon sequestration, on the other hand, is a viable strategy to combat non-net-zero emissions from these types of industrial processes, where the basic principle is the prevention of CO_2 release into the atmosphere, typically by storing it underground [140]. Unfortunately, this area remains largely untapped, as it is currently not a financially viable business model. The last method, carbon recycling, involves the formal conversion of CO_2 to a more energetic, useful product (i.e., alcohols). This is not an easy endeavor, as CO_2 exists in the formal oxidation state of +4, the most oxidized form of carbon, requiring the transfer of electrons to achieve a more reduced product. In Nature, this is achievable by some biocatalysts in plant photosynthesis systems and cyanobacteria through a process called carbon fixation, which has been the source of inspiration for a myriad of biomimetic synthetic catalysts [141]. Traditionally, CO_2 hydrogenation has been used to produce syngas, a mixture of H_2 and CO, which itself is an important feedstock, and a precursor to key industrial processes such as the Fischer-Tropsch reaction and the generation of methane gas via methanation [142]. Recent studies have also looked at the electrochemical reduction of CO2, which presents several advantages including: (1) combining electrochemical water splitting and thermal hydrogenation into a single process, (2) facilitating the formation of products that are not thermally driven, and (3) typically these reactions can occur at or near room temperatures and ambient pressures [143]. However, to date, only heterogenous copper containing catalysts have exhibited feasible reactivity towards CO_2 to produce more valuable hydrocarbons/alcohols (i.e., ethylene and ethanol), via electrochemical CO_2 reduction; and while certainly this field has come a long way since the 1980's, there is still much left to unearth. While there has been a vast increase on the

literature with regards to the reduction of CO_2 to single carbon species in the past decades, reductions to multi-carbon species remains vastly underwhelming, with limited examples reported [144], [145]. Notably, formation of oxalate species from CO_2 fixation have been observed by both d and f-block metal complexes, however, these reactions typically require powerful reducing agents, such as potassium graphite (KC_8) and supporting electrolytes such as lithium perchlorate ($LiClO_4$) [146], [147]. As such, the synthesis of a complex capable of conducting these reactions under milder conditions is desirable.

4.1.1: Carbon fixation by copper-pyrazole complexes

Carbon dioxide has experienced a surge in atmospheric concentrations since the start of the industrial revolution, as a result of continued reliance on fossil fuels for energy, has typically been considered an undesirable greenhouse gas [148]. More recently, however, it has been realized that CO_2 has the potential to be an inexpensive feedstock chemical that is an abundant, nontoxic source of renewable C1 building blocks with an executive report detailing possible applications of the 200+ million tons produced each year from emissions [149].

4.2: Experimental

4.2.1: Synthesis of $[Cu^{II}_2(\mu\text{-}\kappa^2,\kappa^2\text{-}C_2O_4)(bipy)_2I_2]$.DMSO (11)

Method A: A 20 mL scintillation vial is charged with 38.0 mg (0.20 mmol) CuI, 100 mg (0.20 mmol) PNpzH, and dissolved under stirring, in 5 mL DMSO. To the solution, 40 μL (0.40 mmol) of Et_3N is added dropwise. The solution turned from a dark greenish yellow to a dark red color. After stirring for 15 min, 31.0 mg (0.20 mmol) 2,2'-bipy was added. The solution intensifies in

color to deep red. The reaction mixture is stirred for 24 h, gradually turning to deep green color. The reaction mixture was filtered through celite and glass wool to remove unreacted material, and the filtrate is set to slow diffuse in an Et_2O chamber. Dark green, plate-shaped crystals suitable for SCXRD are obtained after approximately 2 weeks. Yield: 18.5 mg, 20%. Chemical formula, $C_{13}H_{14}CuIN_2O_3S$; molecular weight, 462.71 g/mol.

$\tilde{\nu}_{CO}$ for bound oxalate is 1639 cm^{-1}

4.2.2: Crystal structure data table

*Table 14. Crystallographic tables for complex **11**.DMSO*

Identification code	**11**
Empirical formula	$C_{13}H_{14}CuIN_2O_3S$
Formula weight	462.71
Temperature/K	273.15
Crystal system	monoclinic
Space group	$P2_1/c$
a/Å	10.5329(8)
b/Å	17.508(1)
c/Å	9.3017(7)
α/°	90
β/°	100.602(1)
γ/°	90
Volume/Å^3	1686.0(2)
Z	2
ρ_{calc}g/cm^3	1.823
μ/mm^{-1}	3.258
F(000)	888.0
Crystal size/mm^3	0.274 × 0.181 × 0.145
Radiation	MoKα (λ = 0.71073)
2Θ range for data collection/°	5.026 to 68.772
Index ranges	$-16 \leq h \leq 16$, $-27 \leq k \leq 27$, $-14 \leq l \leq 14$
Reflections collected	37749
Independent reflections	7085 [R_{int} = 0.0399, R_{sigma} = 0.0259]
Data/restraints/parameters	7085/3/203
Goodness-of-fit on F^2	1.083
Final R indexes [I>=2σ (I)]	R_1 = 0.0472, wR_2 = 0.1141
Final R indexes [all data]	R_1 = 0.0921, wR_2 = 0.1530
Largest diff. peak/hole / e Å^{-3}	0.60/-0.98

4.3: Results and discussion

4.3.1: Synthesis and characterization

While attempting to optimize the synthesis of complex **3**, which suffers from solvent loss and disorder at rt, a new complex was formed serendipitously, which features an oxalate bridge. Scheme 30 shows the synthesis and line drawing of Complex **11**. CuI and PNpzH

were mixed in DMSO solvent and the base, Et_3N, was added, while holding off on addition of the auxiliary ligand, bipy. The reasoning behind this change was to facilitate the deprotonation and binding of $PNpz^-$ to the Cu center in a manner similar to complex **1**. Afterwards the addition of bipy would complete the reaction, and the desired product, complex **3** was expected, and set to crystallize in an Et_2O chamber where it remained for weeks. As Et_2O and DMSO are not miscible, the Et2O simply sat on top of the DMSO, and slowly evaporated. To our surprise, the green crystals obtained for SCXRD turned out to be an oxalate-bridged complex. As no other reagents were introduced in the system, it is speculated that the oxalate bridge came from atmospheric capture of CO_2. This, however, requires significant further investigations as the reduction of CO_2 to $C_2O_4^{2-}$ is potentially industrially and environmentally significant.

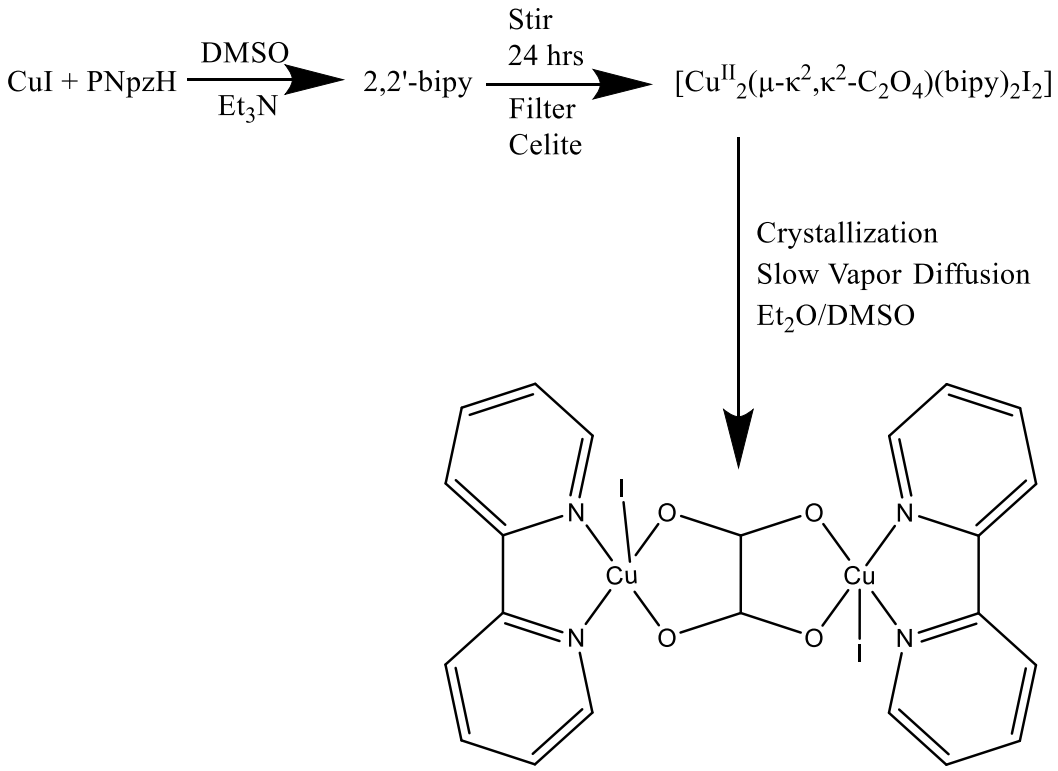

*Scheme 30. Reaction conditions for the formation of the oxalate evolution complex **11**.*

We envision further reaction of **11** with HI, releasing oxalic acid and reducing Cu(II) to Cu(I), converting the stoichiometric reduction of CO_2 into catalytic.

4.3.2: Crystal structural descriptions: Copper(II) dimer Complex 11.

Complex **11** crystallizes in the *P2₁/c* space group with one-half the molecule and one-half interstitial DMSO in the asymmetric unit (Figure 67). The Cu(II) centers sit 5.1519(1) Å apart. Table 14 shows the crystallographic table for complex **11**.

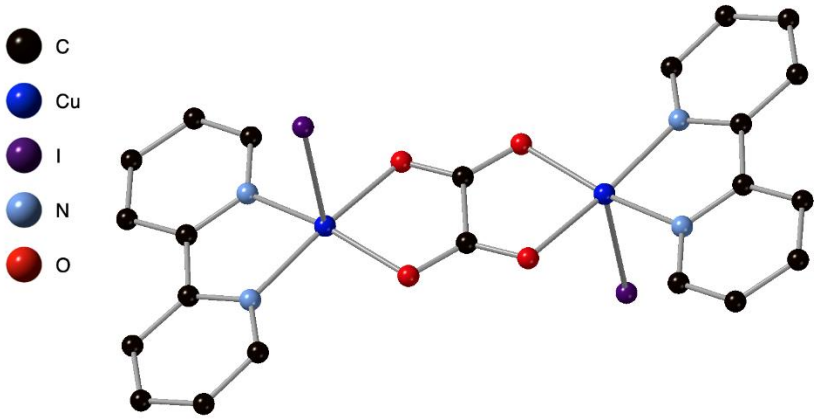

*Figure 67. Crystal structure for complex **11**, interstitial DMSO molecule has been omitted.*

Chapter 5: Conclusions and future work

5.1: Conclusions

Of the complexes studied in this project, only complex **9** has been shown to mediate oxidation/oxygenation transfer chemistry. We believe this is because of the secondary sphere interactions present in the complex, which are remarkably similar to the interactions of biological metalloproteins active cores and protein residues. Complex **9** has shown a propensity and viability towards O^{2-} transfer chemistry and alkane oxidations, being able to carry out reactions analogous to those of both oxygenases and oxidases. Oxidations performed on increasingly tougher substrates have been successful in achieving both oxidation products. Comparisons of the topological parameters of the $Cu_2(\mu\text{-}O)$ active center, both with the literature and other complexes in this study, has suggested the assignment of $Cu_2(\mu\text{-}OH)$ as the resting state, and bent $Cu_2(\mu\text{-}O)$ as the active species. Work done on similar complexes in this study have solidified the importance of the stability imparted onto the complex by the hydrogen-bonded counterion enabling the oxide-hydroxide equilibrium, as none of the other complexes possess such an interaction and to the best of our knowledge, have led to no catalytic activity. The oxidation of cyclohexane to 1,6-hexanediol, an important industrial feedstock in the production of polyester, polyurethane and specialty chemicals. The absence of carboxylic acids in the reaction product mixture is attributed to either selectivity of the catalyst, or failure to detect this product. In turn, the failure to detect carboxylic acids can be attributed either to the experimental method employed (GC-MS), or to coordination of carboxylates to Cu^{II}, poisoning the catalyst. The characterization of the mononuclear aqua-complex **10**, formed

along with **9**, suggests that excess water (a product of alkane oxidation) might also terminate the catalytic cycle by forming **10**. Lastly, the oxidation of saturated alkanes with high C-H bond energies suggests that catalytic oxidation of methane might also be achievable using compound **9**, under appropriate conditions.

5.2: Future work

Future work on this study will apply the synthetic procedures that afforded complex **9** to produce various other complexes with the same motif, a reactive bent-oxo bridge that is hydrogen bonded to a liable proton acceptor. For example, by substituting PNpzH with a 4-X-3,5-Ph_2-pyrazole. Likewise, tuning the electrochemical properties of the complex can be accomplished by substitution on the diphenyl rings of the pyrazole. A nitrated, halogenated pyrazole species should be producible in good quantities. Use of substituted 2,2'-bipy ligands may further tune the redox properties. Further studies into the magnetic properties of the complexes by both EPR and magnetic susceptibility should be investigated on existing complexes, and any new ones synthesized. Investigation of catalyst poisoning should also be conducted to determine what causes the death of the catalyst, as currently no obvious answers have been found. The oxidation of cyclohexene should also be investigated further as the cyclic alkenes tend to undergo epoxidation upon oxygen transfer. Further studies include investigation of site selectivity in the oxidation of complex substrates, such as natural products and pharmaceuticals, and degradation of organic/synthetic polymers via catalytic oxidation/oxygenation. Lastly, to wrap up this story, more intensive catalytic and kinetics studies should be completed on the existing complex, and any new catalytically active ones produced. Methane oxidation studies in

heterogenous/homogenous conditions should be explored as well as mechanistic and DFT studies to elucidate the structure and energy of the transition state. For heterogenous catalysis, super critical CO_2 can be employed, with the catalyst in solution. All in all the outlook for the project has demonstrated the ability of copper(II) dimers stabilized by secondary sphere interactions to successfully mediate biomimetic catalysis with multiple avenues available to explore and study in more detail.

References

[1] J. F. Collins and L. M. Klevay, "Copper," *Adv. Nutr.,* vol. 2, no. 6, pp. 520-522, 2011.

[2] R. Patel and M. Aschner, "Commonalities between Copper Neurotoxicity and Alzheimer's Disease.," *Toxics,* vol. 9, no. 4, 2021.

[3] C. Santini, M. Pellei, V. Gandin, M. Porchia, F. Tisato and C. Marzano, "Advances in Copper Complexes as Anticancer Agents," *Chem. Rev.,* vol. 114, no. 1, pp. 815-862, 2014.

[4] E. S. G. Barrón, R. H. Demeio and F. Kemmerer, "Studies on biological oxidations: V. Copper and hemochromogens as catalysts for the oxidation of ascorbic acid. The mechanism of the reaction.," *J. Biol. Chem.,* vol. 112(2), pp. 625-640, 1936.

[5] L. N. Lewis, J. Stein, Y. Gao, R. E. Colborn and G. Hutchins, "Platinum Catalysts Used in the Silicones Industry.," *Platinum Metal. Rev.,* vol. 41(2), pp. 66-75, 1997.

[6] P. d. J. Krijin, Synthesis of Solid Catalysts, Weinheim: Wiley-VCH, 2009.

[7] J. C. Vedrine, "Metal Oxides in Heterogeneous Oxidation Catalysis: State of the Art and Challenges for a More Sustainable World," *ChemSusChem,* vol. 12, pp. 577-588, 2019.

[8] B. Wels and D. C. Johnson, "Electro-catalysis of Anodic Oxygen Transfer Reactions: Oxidation of Cyanide at Electrodepos-ited Copper Oxide Electrodes in Alkaline Media.," *J. Electrochem. Soc.,* vol. 137(9), pp. 2785-2791, 1990.

[9] J. Haber and M. Witko, "Oxidation catalysis—electronic theory revisited," *Journal of Catalysis,* vol. 216, pp. 416-424, 2003.

[10] R. Sharma, H. Poelman, G. B. Marin and V. V. Galvita, "Approaches for Selective Oxidation of Methane to Mehthanol," *Catalysts,* vol. 10, pp. 194-220, 2020.

[11] A. Gunay and K. H. Theopold, "C−H Bond Activations by Metal Oxo Compounds.," *Chem. Rev.,* vol. 110(2), pp. 1060-1081, 2010.

[12] D. M. Kurtz, "Oxo- and hydroxo-bridged diiron complexes: a chemical perspective on a biological unit.," *Chem. Rev.,* vol. 90(4), pp. 585-606, 1990.

[13] S. D. McCann and S. S. Stahl, "Copper-Catalyzed Aerobic Oxidations of Organic Molecules: Pathways for Two-Electron Oxi-dation with a Four-Electron Oxidant and a One-Electron Redox-Active Catalyst.," *Accounts of Chemical Research,* vol. 48(6), pp. 1756-1766, 2015.

[14] G. M. Whitesides and C. H. Wong, "Enzymes as Catalysts in Synthetic Organic Chemistry [New Synthetic Methods (53)]," *Angew. Chem. Int. Ed. Engl.,* vol. 24, pp. 617-638, 1985.

[15] A. M. McDonnell and C. H. Dang, "Basic Review of the Cytochrome P450 System," *J. Adv. Pract. Oncol.,* vol. 4(4), pp. 263-268, 2013.

[16] R. Banerjee, J. C. Jones and J. D. Lipscomb, "Soluble Methane Monooxygenase," *Annual Review of Biochemistry,* vol. 88(1), pp. 409-431, 2019.

[17] S. E. Allen, R. R. Walvoord, R. Padilla-Salinas and M. C. Kozlowski, "Aerobic Copper-Catalyzed Organic Reactions.," *Chem. Rev.,* vol. 113(8), pp. 6234-6458, 2013.

[18] D. L. Nelson, M. M. Cox and A. L. Lehninger, Principles of Biochemistry., New York: W.H. Freeman, 2008.

[19] C. Kaintz, S. G. Mauracher and A. Rompel, Advances in Protein Chemistry and Structural Biology, vol. 97, Academic Press, 2014, pp. 1-35.

[20] A. Messerschmidt, Comprehensive Natural Products II, Elsevier, 2010, pp. 489-545.

[21] K. J. Koebke, L. Ruckthong, J. L. Meagher, E. Mathieu, J. Harland, A. Deb, N. Lehnert, C. Policar, C. Tard, J. E. Penner-Hahn, J. A. Stuckey and V. L. Pecoraro, "Clarifying the Copper Coordination Environment in a de Novo Designed Red Copper Protein," *Inorg. Chem.,* vol. 57, pp. 12291-12302, 2018.

[22] E. I. Solomon, D. E. Heppner, E. M. Johnston, J. W. Ginsbach, J. Cirera, M. Qayyum, M. T. Kieber-Emmons, C. H. Kjaergaard, R. G. Hadt and L. Tian, "Copper Active Sites in Biology," *Chem. Rev.,* vol. 114(7), pp. 3659-3853, 2014.

[23] K. I. Tishchenko, E. K. Beloglazkina, A. G. Mazhuga and N. V. Zyk, *Ref. J. Chem.,* vol. 6, pp. 49-82, 2016.

[24] M. Rolff, J. Schottenheim, H. Decker and F. Tuczek, "Copper–O2 reactivity of tyrosinase models towards ex-ternal monophenolic substrates: molecular mechanism and comparison with the en-zyme," *Chem. Soc. Rev.,* vol. 40, pp. 4077-4098, 2011.

[25] A. G. Blackman and W. B. Tolman, "Copper-Dioxygen and Copper-Oxo Species Relevant to Copper Oxygenases and Oxidases," in *Metal-Oxo and Metal-Peroxo Species in Catalytic Oxidations*, Springer, Berlin, Heidelberg, 2001, pp. 179-211.

[26] S. Sahu, L. R. Widger, M. G. Quesne, S. P. De Visser, H. Matsumura, P. Moënne-Loccoz, M. A. Siegler and D. P. Goldberg, "Secondary Coordination Sphere

Influence on the Reactivity of Nonheme Iron(II) Complexes: An Experimental and DFT Approach," *J. Am. Chem. Soc.*, vol. 135(29), pp. 10590-10593, 2013.

[27] B. P. Fedoretz-Maxwell, C. H. Shin, G. A. MacNeil, L. J. Worrall, R. Park, N. C. J. Strynadka, C. J. Walsby and J. J. Warren, "The Impact of Second Coordination Sphere Me-thionine-Aromatic Interactions in Copper Proteins," *Inorganic Chemistry*, vol. 61(14), pp. 5563-5571, 2022.

[28] L. M. Mirica, X. Ottenwaelder and T. D. P. Stack, "Structure and Spectroscopy of Copper−Dioxygen Complexes.," *Chem. Rev.*, vol. 104(2), pp. 1013-1046, 2004.

[29] M. R. Halvagar, P. V. Solntsev, H. Lim, B. Hedman, K. O. Hodgson, E. I. Solomon, C. J. Cramer and W. B. Tolman, "Hydroxo-Bridged Dicopper(II, III) and -(III, III) Complexes: Models for Putative Intermediates in Oxidation Catalysis.," *J. Am. Chem. Soc.*, vol. 136(20), pp. 7269-7272, 2014.

[30] K. D. Demadis, C. M. Hartshorn and T. J. Meyer, "The Localized-to-Delocalized Transition in Mixed-Valence Chemistry.," *Chem. Rev.*, vol. 101(9), pp. 2655-2686, 2001.

[31] D. Widmann and R. J. Behm, "Activation of Molecular Oxygen and the Nature of the Active Oxygen Species for CO Oxidation on Oxide Supported Au Catalysts.," *Acc. Chem. Res.*, vol. 47(3), pp. 740-749, 2014.

[32] R. Neumann and A. M. Khenkin, "Molecular oxygen and oxidation catalysis by phosphovanadomolybdates.," *Chem. Commun.*, vol. 24, pp. 2529-2538, 2006.

[33] C. Zuccaccia, G. Bellachioma, O. Bortolini, A. Bucci, A. Savini and A. Macchioni, "Transformation of a Cp*-Iridium(III) Precatalyst for Water Oxidation when Exposed to Oxidative Stress.," *Chem. -Eur. J.*, vol. 20, p. 3446, 2014.

[34] C. E. Elwell, N. L. Gagnon, B. D. Neisen, D. Dhar, A. D. Spaeth, G. M. Yee and W. B. Tolman, "Copper–Oxygen Complexes Revisited: Structures, Spectroscopy, and Reactivity.," *Chem. Rev.*, vol. 117(3), pp. 2059-2107, 2017.

[35] C.-C. Liu, Y.-F. Tsai, C.-Y. Mou, S. S. F. Yu and S. I. Chan, "Dicopper Dioxygenase Model Immobilized in Mesoporous Silica Nanoparticles for Toluene Oxidation: A Mechanism to Harness Both O Atoms of O2 for Catalysis.," *J. Phys. Chem.*, vol. 123(17), pp. 11032-11043, 2019.

[36] M. Miyanishi, T. Abe, Y. Hori, Y. Shiota and K. Yoshizawa, "Role of Amino Acid Residues for Dioxygen Activation in the Second Coordination Sphere of the Dicopper Site of pMMO.," *Inorg. Chem.*, vol. 58(18), p. 12280–12288, 2019.

[37] X. Feng, Y. Song, J. S. Chen, Z. Xu, S. J. Dunn and W. Lin, "Rational construction of an Artificial Binuclear Copper Monooxygenase in a Metal-Organic Framework.," *J. Am. Chem. Soc.*, Vols. 1107-1118, p. 143, 2021.

[38] R. Trammell, K. Rajabimoghadam and I. Garcia-Bosch, "Copper-Promoted Functionalization of Organic Molecules: from Biologically Relevant Cu/O2 Model Systems to Organometallic Transformations.," *Chem. Rev.*, vol. 119(4), pp. 2954-3031, 2019.

[39] S. Sirajuddin and A. C. Rosenzweig, "Enzymatic Oxidation of Methane.," *Biochem.*, vol. 54(14), pp. 2283-2294, 2015.

[40] L. Tahsini, H. Kotani, Y.-M. Lee, J. Cho, W. Nam, D. K. Karlin and S. Fukuzum, "Electron-Transfer Reduction of Dinuclear Copper Peroxo and Bis-μ-oxo Complexes Leading to the Catalytic Four-Electron Reduction of Dioxygen to Water.," *Chem. Eur. J.*, vol. 18(4), pp. 1084-1093.

[41] M. Jacoby, "Copper Dimers Reduce NOx," *C&EN*, vol. 95, no. 34, p. 8, 2017.

[42] P. Gamez, I. A. Koval and J. Reedijk, " Bio-mimicking galactose oxidase and hemocyanin, two dioxygen-processing copper proteins," *Dalton Trans.*, pp. 4079-4088, 2004.

[43] K. Knittel and A. Boetius, "Anaerobic Oxidation of Methane: Progress with an Unknown Process," *Annu. Rev. Microbiol.*, vol. 63, pp. 311-334, 2009.

[44] H. Bürgmann, "Methane Oxidation (Aerobic)," in *Encyclopedia of Geobiology*, Springer, 2011.

[45] J. Gijs Kuenen, "Anammox bacteria: from discovery," *Nat. Rev. Microbiol.*, vol. 6, pp. 320-326, 2008.

[46] M. S. M. Jetten, M. Strous, K. T. van de Pas-Schoonen, J. Schalk, U. G. J. M. van Dongen, A. A. van de Graaf, S. Logemann, G. Muyzer, M. C. M. van Loosdrecht and J. Gijis Kuenen, "The anaerobic oxidation of ammonium," *FEMS Microbiology Reviews*, vol. 22, no. 5, pp. 421-437, 1998.

[47] F. V. M. Silva and A. Sulaiman, Encyclopedia of Food Chemistry, Academic Press, 2019, pp. 287-301.

[48] A. M. Mayer and E. Harel, "Polyphenol oxidases in plants.," *Phytochemistry*, vol. 18, pp. 193-215, 1979.

[49] T. Klabunde, C. Eicken, J. C. Sacchettini and B. Krebs, "Crystal structure of a plant catechol oxidase containing a dicopper center.," *Nat Struct Biol.*, vol. 5(12), pp. 1084-1090, 1998.

[50] C. Eicken, B. Krebs and J. C. Sacchettini, "Catechol oxidase — structure and activity," *Current Opinion in Structural Biology*, vol. 9, pp. 677-683, 1999.

[51] E. I. Solomon, U. M. Sundaram and T. E. Machonkin, "Multicopper Oxidases and Oxygenases," *Chem. Rev.*, vol. 96(7), pp. 2563-2606, 1996.

[52] P. E. M. Siegbahn, "The catalytic cycle of catechol oxidase.," *J Biol Inorg Chem*, vol. 9, pp. 577-590, 2004.

[53] L. G. Fenoll, M. J. Peñalver, J. N. Rodríguez-López, P. A. García-Ruiz, F. García-Cánovas and J. Tudela, "Deuterium isotope effect on the oxidation of monophenols and o-diphenols by tyrosinase.," *Biochemical Journal*, vol. 380, pp. 643-650, 2004.

[54] K. Narsimhan, K. Iyoki, K. Dinh and Y. Roman-Leshkov, "Catalytic Oxidation of Methane into Methanol over Copper-Exchanged Zeolites with Oxygen at Low Temperature," *ACS Cent. Sci.*, vol. 2, pp. 424-429, 2016.

[55] G. A. Olah, "Beyond Oil and Gas: The Methanol Economy.," *Angewandte Chemie International Edition*, vol. 44, pp. 2636-2639, 2005.

[56] B. Girod, D. P. Vuuren and E. Hertwich, "Climate policy through changing consumption choices: Options and obstacles for reducing greenhouse gas emissions.," *Glob Environ*, vol. 25, pp. 5-15, 2014.

[57] H. Kaserer, "Ueber die Oxydation des Wasserstofes und des Methane durch Mikroorganismen.," *Z. landv. Versuchsw. Deut. Oesterr.*, vol. 8, p. 789, 195.

[58] N. L. Söhngen, "Uber Bakterien, welche methan als Kohlenstoffnahrung Energiequelle gebrauchen.," *Zentr. Bakt. Parasitenk.*, vol. 2, pp. 513-517, 1906.

[59] R. L. Lieberman and A. C. Rosenzweig, "Crystal structure of a membrane-bound metalloenzyme that catalyses the biological oxidation of methane," *Nature*, pp. 177-182, 2005.

[60] S. M. Smith, S. Rawat, J. Telser, B. M. Hoffman, T. L. Stemmler and A. C. Rosenzweig, "Crystal Structure and Characterization of Particulate Methane Monooxygenase from Methylocystis species Strain M," *Biochemistry* , vol. 50(47), pp. 10231-10240, 2011.

[61] R. Balasubramanian, S. M. Smith, S. Rawat, L. A. Yatsunyk, T. L. Stemmler and A. C. Rosenzweig, "Oxidation of methane by a biological dicopper centre," *Nature*, vol. 465, pp. 115-119, 2010.

[62] X. Xie, S. I. Gorelsky, R. Sarangi, D. K. Garner, H. J. Hwang, K. O. Hodgson, B. Hedman, Y. Lu and E. I. Solomon, "Perturbations to the geometric and electronic structure of the Cua site: factors that influence delocalization and their contributions to electron transfer.," *J. Am. Chem. Soc.*, vol. 130, pp. 5194-5205, 2008.

[63] K. Yoshizawa and Y. Shiota, "Conversion of methane to methanol at the mononuclear and dinuclear copper sites of particulate methane monooxygenase

(pMMO): a DFT and QM/MM study.," *J. Am. Chem. Soc,* vol. 128, pp. 9873-9881, 2006.

[64] Y. Shiota and K. Yoshizawa, "Comparison of the reactivity of bis(μ-oxo)Cu II Cu III and Cu III Cu III species to methane.," *Inorg. Chem.,* vol. 48, pp. 838-845, 2009.

[65] Y. Shiota, G. Juhasz and K. Yoshizawa, "Role of tyrosine residue in methane activation at the dicopper site of particulate methane monooxygenase: a density functional theory study.," *Inorg. Chem.,* vol. 52, pp. 7907-7917, 2013.

[66] M. O. Ross, F. MacMillian, J. Wang, A. Nisthal, T. J. Lawton, B. D. Olafson, S. L. Mayo, A. C. Rosenzweig and B. M. Hoffman, "Particulate methane monooxygenase contains only mononuclear copper centers," *Sience,* vol. 364, pp. 566-570, 2019.

[67] L. Cao, O. Caldararu, A. C. Rosenzweig and U. Ryde, "Quantum Refinement Does Not Support Dinuclear Copper Sites in Crystal Structures of Particulate Methane Monooxygenase," *Angew. Chem. Int. Ed.,* vol. 57, pp. 162-166, 2018.

[68] R. R. Grinstead, "Metal-catalyzed Oxidation of 3,5-di-t-Butyl Pyrocatechol, and Its Significance in the Mechanism of Pyrocatechase Action," *Biochemistry* , vol. 3(9), pp. 1308-1314, 1964.

[69] I. A. Koval, M. Huisman, A. F. Stassen, P. Gamez, O. Roibeau, C. Belle, J.-L. Pierre, E. Saint-Aman, M. Lüken, B. Krebs, M. Lutz, A. L. Spek and J. Reedijk, "Dinuclear CuII Complexes with a New Phenol-Based Ligand Bearing Pyridine and Thiophene Substituents: Synthesis, Characterization and Interaction with Catechol Substrates.," *Eur. J. Inorg. Chem.,* pp. 4036-4045, 2004.

[70] S. K. R. Dey and A. Mukherjee, "Catechol oxidase and phenoxazinone synthase: Biomimetic functional models and mechanistic studies," *Coordination Chemistry Reviews,* vol. 310, pp. 80-115, 2016.

[71] M. O. Ross and A. C. Rosenzweig, "A tale of two methane monooxygenases.," *J. Biol. Inorg. Chem.,* vol. 22, pp. 307-319, 2017.

[72] H. M. Rhoda, A. J. Heyer, B. E. R. Snyder, D. Plessers, M. L. Bols, R. A. Schoonheydt, B. F. Sels and E. I. Solomon, "Second-Sphere Lattice Effects in Copper and Iron Zeolite Catalysis," *Chem. Rev.,* vol. 122(14), pp. 12207-12243, 2022.

[73] M. R. Halvagar, P. V. Solnstev, H. Lim, B. Hedman, K. O. Hodgson, E. I. Solomon, C. J. Cramer and W. B. Tolman, "Hydroxo-Bridged Dicopper(II,III) and -(III,III) Complexes: Models for Putative Intermediates in Oxidation Catalysis," *J. Am. Chem. Soc.,* vol. 136, no. 20, pp. 7269-7272, 2014.

[74] T. Tsuji, A. A. Zaoputra, Y. Hitomi, K. Mieda, T. Ogura, Y. Shiota, K. Yoshizawa, H. Sato and M. Kodera, "Specific Enhancement of Catalytic Activity by a Dicopper

Core: Selective Hydroxylation of Benzene to Phenol with Hydrogen Peroxide," *Angew. Chem. Int. Ed.,* vol. 56, pp. 7779-7782, 2017.

[75] X. Zhang, Y.-Y. Li, J. Jiang, R. Zhang, R.-Z. Liao and M. Wang, "A Dinuclear Copper Complex Featuring a Flexible Linker as Water Oxidation Catalyst with an Activity Far Superior to Its Mononuclear Counterpart," *Inorg. Chem.,* vol. 59, no. 8, pp. 5424-5432, 2020.

[76] J. A. Isaac, A. Thibon-Pourret, A. Durand, C. Philouze, N. Le Poul and C. Belle, "High-valence CuIICuIII species in action: demonstration of aliphatic C–H bond activation at room temperature," *Chem. Comm.,* vol. 55, pp. 12711-12714, 2019.

[77] C.-C. Liu, Y.-F. Tsai, C.-Y. Mou, S. S. F. Yu and S. I. Chan, "Dicopper Dioxygenase Model Immobilized in Mesoporous Silica Nanoparticles for Toluene Oxidation: A Mechanism to Harness Both O Atoms of O2 for Catalysis," *J. Phys. Chem. C.,* vol. 123, no. 17, pp. 11032-11043, 2019.

[78] G. Ali, P. E. Van Natta, D. A. Ramirez, K. M. Light and M. T. Kieber-Emmons, "Thermodynamics of a μ-oxo Dicopper(II) Complex for Hydrogen Atom Abstraction," *J. Am. Chem. Soc.,* vol. 139, no. 51, pp. 18448-18451, 2017.

[79] M. D. Vaira, F. Mani and P. Stoppioni, "A general and very straightforward route to the selective N-functionalization of 1,4,7-triazacyclononane with imidazole groups. Crystal structure determinations of nickel(II), copper(II) and zinc(II) complexes," *Inorg. Chim. Acta,* vol. 15, no. 1, pp. 61-69, 2000.

[80] A. K. Patra, M. Ray and R. Mukherjee, "Magneto–structural studies of monohydroxo-bridged dicopper(II) complexes M[Cu2L2(OH)]·2H2O (M=Na+ (1) and K+ (2); H2L=2,6-bis[N-(phenyl)carbamoyl]pyridine). Effect of Cu□OH□Cu bridge angle on antiferromagnetic coupling," *Polyhedron,* vol. 19, no. 12, pp. 1423-1428, 2000.

[81] M. S. Haddad, S. R. Wilson, D. J. Hodgson and D. N. Hendrickson, "Magnetic Exchange Interactions in Binuclear Copper(II) Complexes with Only a Single Hydroxo Bridge: The x-Ray Structure of.Mu.-Hydroxo-Tetrakis(2,2'-Bipyridine)Dicopper(II) Perchlorate.," *J. Am. Chem. Soc.,* vol. 103, no. 2, pp. 384-391, 1981.

[82] A. Thibon-Pourret, F. Gennarini, R. David, J. A. Isaac, I. Lopez, G. Gellon, F. Molton, L. Wojcik, C. Philouze, D. Flot, Y. Le Mest, M. Reglier, N. Le Poul, H. Jamet and C. Belle, "Effect of Monoelectronic Oxidation of an Unsymmetrical Phenoxido-Hydroxido Bridged Dicopper(II) Complex," *Inorg. Chem.,* vol. 57, no. 19, pp. 12364-12375, 2018.

[83] Y. Matoba, T. Kumagai, A. Yamamoto, H. Yoshitsu and M. Sugiyama, "Crystallographic evidence that the dinuclear copper center of tyrosinase is flexible during catalysis," *J. Biol. Chem.*, vol. 281, no. 13, pp. 8981-8990, 2006.

[84] T. Klabunde, C. Eicken, J. C. Sacchettini and B. Krebs, "Crystal structure of a plant catechol oxidase containing a dicopper center," *Nat. Struct. Biol.*.

[85] V. M. Virador, J. P. Reyes Grajeda, A. Blanco-Labra, E. Mendiola-Olaya, G. M. Smith, A. Moreno and J. R. Whitaker, "Cloning, sequencing, purification, and crystal structure of Grenache (Vitis vinifera) polyphenol oxidase," *J. Agric. Food Chem.*, vol. 58, no. 2, pp. 1189-11201, 2010.

[86] W.-Z. Shen, D. Gupta and B. Lippert, "Cyclic Trimer versus Head−Tail Dimer in Metal−Nucleobase Complexes: Importance of Relative Orientation (Syn, Anti) of the Metal Entities and Relevance as a Metallaazacrown Compound.," *Inorg. Chem.*, vol. 44(23), pp. 8249-8258, 2005.

[87] P. J. Zinn, D. R. Powell, V. W. Day, M. P. Hendrich, T. N. Sorrell and A. S. Borovik, "Pyrazolate-Bridging Dinucleating Ligands Containing Hydrogen-Bond Donors: Synthesis and Structure of Their Cobalt Analogues," *Inorg. Chem.*, vol. 45(9), pp. 3484-3486, 2006.

[88] S.-M. Jung, M. Yang and W. J. Song, "Symmetry-Adapted Synthesis of Dicopper Oxidases with Divergent Dioxygen Reactivity," *Inorg. Chem.*, vol. 61, no. 31, pp. 12433-12441, 2022.

[89] A. Brinkmeier, K. E. Dalle, L. D'Amore, R. A. Schulz, S. Dechert, S. Demeshko, M. Swart and F. Meyer, "Modulation of a μ-1,2-Peroxo Dicopper(II) Intermediate by Strong Interaction with Alkali Metal Ions," *J. Am. Chem. Soc.*, vol. 143, no. 42, pp. 17751-17760, 2021.

[90] L. O. Fuentes-Lara, J. Medrano-Macias, F. Perez-Labrada, E. N. Rivas-Martinez, E. L. Garcia-Enciso, S. Gonzalez-Morales, A. Juarez-Maldonado, F. Rincon-Sanchez and A. Benavides-Mendoza, "From Elemental Sulfur to Hydrogen Sulfide in Agricultural Soils and Plants," *Molecules*, vol. 24, p. 2282, 2019.

[91] L. Bharathi, Encyclopedia of Ecology, 3424-3431, 2008.

[92] E. L. S. Hinckley, J. T. Crawford, H. Fakhraei and C. T. Driscoll, "A shift in sulfur-cycle manipulation from atmospheric emissions to agricultural additons," *Nat. Geosci.*, pp. 1-8, 2020.

[93] J. Campos-Martin, M. Capel-Sanchez, P. Perez-Presas and J. Fierro, "Oxidative Processes of Desulfurization of Liquid Fuels," *J. Chem. Tech. & Biotech*, vol. 85, no. 7, pp. 879-890, 2010.

[94] N. Kostopoulos, C. Achaibou, J.-M. Noel, F. Kanoufi, M. Robert, C. Fave and E. Anxolabehere-Mallart, "Electrocatalytic O2 Activation by Fe Tetrakis(pentafluorophenyl)porphyrin in Acidic Organic Media. Evidence of High-Valent Fe Oxo Species," *Inorg. Chem. ,* vol. 59, pp. 11577-11583, 2020.

[95] A. L. Kohl and R. B. Nielsen, "Sulfur Recovery Processes," in *Gas Purification*, Gulf Professional Publishing, 1997, pp. 670-730.

[96] C. Song and X. Ma, "New design approaches to ultra-clean diesel fuels by deep desulfurization and deep dearomatization.," *Appl. Catal. B: Enviromental,* vol. 41, no. 1-2, pp. 207-238, 2003.

[97] F. Kamali, M. M. Eskandari, A. Rashidi, M. Baghalha, M. Hasanisadi and T. Hamzehlouyan, "Nanorod carbon nitride as a carbo catalyst for selective oxidation of hydrogen sulfide to sulfur," *J. Hazard. Mater.,* vol. 364, pp. 218-226, 2019.

[98] G. Lei, W. Zhao, L. Shen, S. Liang, C. Au and L. Jiang, "Isolated iron sites embedded in graphitic carbon nitride (g-C3N4) for efficent oxiadtive desulfurization," *Applied Catalysis B. Enviromental,* vol. 267, p. 118663, 2020.

[99] J. A. Cecilia, M. D. Soriano, L. M. Correia, E. Rodriguez-Castellon, J. M. Lopez-Nieto and R. S. Vieira, "Fe2O3 supported on hollow micro/mesospheres silica for the catalytic partial oxidation of H2S to sulfur," *Microporous and Mesoporous Materials,* vol. 294, p. 109875, 2020.

[100] X. Zhang, G. Dou, Z. WAng, L. Li, Y. Wang, H. Wang and Z. Hao, "Selective catalytic oxidation of H2S over iron oxide supported on alumina-intercalated laponite caly catalysts," *J. Hazard. Mater,* vol. 260, pp. 104-111, 2013.

[101] X. Zheng, L. Zhang, Z. Fan, Y. Cao, L. Shen, C. Au and Jiang L., "Enhanced catalytic activity over MIL-100 (Fe) with coordinatively unsaturated Fe2/Fe3 sites for selective oxidation of H2S to sulfur," *Chem. Eng. J.,* vol. 374, pp. 793-801, 2019.

[102] G. Y. Kreitman, J. C. Danilewicz, D. W. Jeffery and R. J. Elias, "Reaction Mechanisms of Metals with Hydrogen Sulfide and Thiols in Model Wine. Part 1: Copper-Catalyzed Oxidation," *J. Agric. Food Chem.,* vol. 64, no. 20, pp. 4095-4101, 2016.

[103] K. L. Rao, M. P. Rao, B. Sethuram and T. N. Rao, "Oxidations by iron(VI). Kinetic study of uncatalysed and osmium (VIII) catalysed oxidations of dimethyl sulphoxide in alkaline medium.," *Trans. Met. Chem.,* vol. 14, no. 3, pp. 165-168, 1989.

[104] L. F. Veiros, C. A. Gamelas, M. J. Calhorda and C. C. Romao, "Chemoselective sulfide and suloxide oxidations by CpMo-(CO)3-Cl/HOOR: a DFT mechanistic study.," *Organometallics,* vol. 30, no. 6, pp. 1454-1465, 2011.

[105] A. Sartorel, P. Miro, M. Carraro, S. Berardi, O. Bortolini, A. Bagno, C. Bo and M. Bonchio, "Oxygenation by Ruthenium Monosubstituted Polyoxotungstates in Aqueous Solution: Experimetnal and Computational Dissection of a Ru (III)-Ru (V) Catalytic Cycle," *Chem. - Eur. J.*, vol. 20, no. 35, pp. 10932-10943, 2014.

[106] G. Brychkova, Z. Xia, G. Yang, Z. Yesbergenova, Z. Zhang, O. Davydov, R. Fluhr and M. Sagi, "Sulfite oxidase protects plants against sulfur dioxide toxicity," *The Plant Journal*, vol. 50, pp. 696-709, 2007.

[107] D. W. Gammon, T. B. Moore and M. A. O'Malley, "A toxicological assessment of sulfur as a pesticide," in *Hayes'HandbookofPesticideToxicology*, New York, NY, Academic Press, 2010, pp. 1889-1901.

[108] C. M. Griffith, J. E. Woodrow and J. N. Seiber, "Environmental behavior and analysis of agricultural sulfur," *Pest Manag. Sci.*, vol. 71, pp. 1486-1496, 2015.

[109] O. V. Dolomanov, L. J. Bourhis, R. J. Gildea, J. A. K. Howard and H. Puschmann, "OLEX2: A Complete Structure Solution, Refinement and Analysis Program," *J. Appl. Cryst.*, vol. 42, pp. 339-341, 2009.

[110] L. Pandolf and C. Portinari, "Trinuclear copper(ii) pyrazolate compounds: a long story of serendipitous discoveries and rational design.," *Cryst. Eng. Comm.*, vol. 19(13), pp. 1701-1720, 2017.

[111] B. Kupcewicz, K. Sobiesiak, K. Malinowska, K. Koprowska, M. Czyz, B. Keppler and E. Budziszl, "Copper(II) complexes with derivatives of pyrazole as potential antioxidant enzyme mimics.," *Med Chem Res.*, vol. 22(5), pp. 2395-2402, 2013.

[112] M. L., "3,5-Bis(2,4-dinitro¬phen¬yl)-4-nitro-1H-pyrazole acetone monosolvate," *Acta Cryst.*, vol. E68, p. o4, 2012.

[113] Z.-G. Zhao and Z.-X. Wang, "Halogenation of Pyrazoles Using N-Halosuccinimides in CCl4 and in Water," *Synthetic Communications*, vol. 37(1), pp. 137-147, 2007.

[114] J. R. Kastner, Q. Buquoi, R. Ganagavaram and K. C. Das, "Catalytic ozonation of gaseous reduced sulfur compounds using wood fly ash," *Environ Sci. Technol.*, vol. 39, no. 6, pp. 1835-1842, 2005.

[115] J. M. Ramirez-Anguita, A. Gonzalez-Lafont and J. M. Lluch, "Formation pathways of DMSO2 in the addition channel of the OH-initiated DMS oxidation: a theoretical study," *J. Comput. Chem.*, vol. 30, no. 9, pp. 1477-1489, 2009.

[116] D. Zhang, J. Dutasta, V. Dufaud, L. Guy and A. Martinez, "Sulfoxidation inside a C3-vanadium(V) bowl-shaped catalyst.," *ACS Catalysis*, vol. 7, pp. 7340-7345, 2017.

[117] S. Zakavi, Z. Kayhomayoon and S. Rayati, "Substrate-dependent order of catalytic activity for a series of Fe(III) and Mn(III) porphyrins in the oxidation of orangic sulfides and olefins with periodate.," *J. Iran Chem. Soc.*, vol. 12, pp. 863-872, 2015.

[118] D. W. Lahti and J. H. Espenson, "Oxidation of Sulfoxides by Hydrogen Peroxide, Catalyzed by Methyltrioxorhenium(VII).," *Inorg. Chem.*, vol. 39, no. 10, pp. 2164-2167, 2000.

[119] P. Moreau, V. Hulea, S. Gomez, D. Brunel and F. Di Renzo, "Oxidation of suloxides to sulfones by hydrogen peroxide over Ti-containing zeolites.," *Applied Catalysis A: General*, vol. 155, pp. 253-263, 1997.

[120] A. Chellamani and S. Harikengaram, "Mechanism of Oxidation of Aryl Methyl Sulfoxides with Sodium Hypochlorite Catalyzed by (Salen)Mn(III) complexes," *J. Mol. Catal. A.*, vol. 247, pp. 260-267, 2006.

[121] E. V. Dikarev, R. Y. Becker, E. Block, Z. Shan, R. C. Haltiwanger and M. A. Petrukhina, "The First Coordination Complexes of Selenones: A Structural Comparison with Complexes of Sulfones," *Inorg. Chem.*, vol. 42, no. 22, pp. 7098-7105, 2003.

[122] P. E. Kruger, "Coordination Polymers and Metal–Organic-Frameworks Derived from 4,4'-Dicarboxy-2,2'-bipyridine and 4,4',6,6'-Tetracarboxy-2,2'-bipyridine Ligands: A Personal Perspective," *CHIMIA International Journal for Chemistry* , vol. 67, pp. 403-410, 2013.

[123] C. A. Paddona, C. E. Banks, I. G. Davies and R. G. Comptona, "Oxidation of anthracene on platinum macro- and micro-electrodes: Sonoelectrochemical, cryoelectrochemical and sonocryoelectrochemical studies.," *Ultrasonics Sonochemistry*, vol. 13(2), pp. 126-132, 2006.

[124] I.-E. Parigoridi, G. J. Corban, S. K. Hadjikakou, N. Hadjiliadis, N. Kourkoumelis, G. Kostakis, V. Psycharis, C. P. Raptopoulouc and M. Kubicki, "Structural motifs of diiodine complexes with amides and thioamides.," *Dalton Trans.*, vol. 38, pp. 5159-5165, 2008.

[125] X.-Q. Zhu, C.-H. Wang and H. Liang, "Scales of Oxidation Potentials, pKa, and BDE of Various Hydroquinones and Catechols in DMSO.," *J. Org. Chem.*, vol. 75, no. 21, pp. 7240-7257, 2021.

[126] S. Xu, "Selective Catalytic Oxidation of Benzyl Alcohol to Benzaldehyde by Nitrates.," *Front. Chem.*, vol. 8(151), 2020.

[127] S. Xu, J. Wu, P. Huang, C. Lao, H. Lai, Y. Wang, Z. Wang, G. Xhong, X. Fu and F. Peng, "Rational Construction of an Artificial Binuclear Copper Monooxygenase

in a Metal–Organic Framework.," *Journal of the American Chemical Society,* vol. 143(2), pp. 1107-1118, 2021.

[128] S. Fang, X. Liang, Y. Long, X. Li, D. Yang, S. Wang and C. Li, "Iridium-Catalyzed Asymmetric Ring-Opening of Azabicyclic Alkenes with Phenols.," *Organometallics*, vol. 31(8), pp. 3113-3118, 2012.

[129] H. Q. Pham and M. J. Marks, "Epoxy Resins," *Kirk-Othmer Encyclopedia of Chemical Technology,* pp. 347-469, 2004.

[130] K. K. Singh, M. K. Tiwari, B. B. Dhar, K. Vanka and S. Sen Gupta, "Mechanism of Oxygen Atom Transfer from Fe V (O) to Olefins at Room Temperature," *Inorg. Chem.,* vol. 54, pp. 6112-6121, 2015.

[131] P. J. Wright and A. M. English, "Scavenging with TEMPO• To Identify Peptide- and Protein-Based Radicals by Mass Spectrometry: Advantages of Spin Scavenging over Spin Trapping," *J. Am. Chem. Soc.,* vol. 125, no. 28, pp. 8655-8665, 2003.

[132] G. Zerjav, A. Albreht, I. Vovk and A. Pintar, "Revisiting terephthalic acid and coumarin as probes for photoluminescent determination of hydroxyl radical formation rate in heterogeneous photocatalysis," *Applied Catalysis A: General*, vol. 598, p. 117566, 2020.

[133] Z. Machatova, Z. Barbierikova, P. Poliak, V. Jancovicova, V. Lukes and V. Brezova, "Study of natural anthraquinone colorants by EPR and UV/vis spectroscopy," *Dyes and Pigments,* vol. 132, pp. 79-93, 2016.

[134] H.-G. Korth and P. Mulder, "Phenolic Hydrogen Transfer by Molecular Oxygen and Hydroperoxyl Radicals. Insights into the Mechanism of the Anthraquinone Process," *J. Org. Chem.,* vol. 85, pp. 2560-2574, 2020.

[135] F. W. Martin, D. A. Bryant and T. J. Beatty, "A physiological perspective on the origin and evolution of photosynthesis," *FEMS Microbiology Reviews*, vol. 42, no. 2, pp. 205-231, 2018.

[136] M. R. Smith and S. S. Myers, "Impact of anthropogenic CO2 emissions on global human nutrition.," *Nature Clim. Change,* vol. 8, pp. 834-839, 2018.

[137] C. Finn., S. Schnittger, L. J. Yellowless and J. B. Love, "Molecular approaches to the electrochemical reduction of carbon dioxide.," *Chem. Commun.,* vol. 48, pp. 1392-1399, 2012.

[138] R. K. Pachauri and L. A. Leyer, "Climate Change 2014: Synthesis Report.," IPCC, Geneva, 2014.

[139] S. J. Davis, N. S. Lewis, M. Shaner, S. Aggarwal, D. Arent, I. L. Azevedo, S. M. Benson, T. Bradley, J. Brouwer and Y.-M. Chiang, "Zet-Zero Emissions Energy Systems," *Science,* vol. 360, p. No. eaas9793, 2018.

[140] A. Majumdar, J. Deutch, R. Bras, S. Benson, E. Carter, D. Ort., M. Ramage, R. Socolow, E. Toone and G. Whitesides, "Task Force on the RD&D Strategy for CO2 Utilization and/or Negative Emissions at the Gigatonne Scale," SECRETARY OF ENERGY ADVISORY BOARD, 2016.

[141] A. M. Appel, J. E. Bercaw, A. B. Bocarsly, H. Dobbek, D. L. DuBois, M. Dupuis, J. G. Ferry, E. Fujita, R. Hille and P. J. Kenis, "Frontiers, Opportunities, and Challenges in Biochemical and Chemical Catalysis of CO2 Fixation.," *Chem. Rev.,* vol. 113, pp. 6621-6658, 2013.

[142] S. Ronsch, J. Schneider, S. Matthischke, M. Schlulter, M. Gotz, J. Lefebvre, P. Prabhakaran and S. Bajohr, "Review on Methanation - From Fundamentals to Current Projects.," *Fuels,* vol. 166, pp. 276-296, 2016.

[143] S. Nitopi, E. Bertheussen, S. B. Scott, X. Liu, A. K. Engstfeld, S. Horch, B. Seger, I. E. L. Stephens, K. Chan, C. Hahn, J. K. Norskov, T. F. Jaramillo and I. Chorkendorff, "Progress and Perspectives of Electrochemical CO2 Reduction on Copper in Aqueous Electrolyte," *Chem. Rev.,* vol. 119, pp. 7610-7672, 2019.

[144] B. J. Cook, G. N. Di Francesco, K. A. Abbound and L. J. Murray, "Countercations and solvent influence CO 2 reduction to oxalate by chalcogen-bridged tricopper cyclophanates.," *J. Am. Chem. Soc.,* vol. 140, pp. 5696-5700, 2018.

[145] R. Angamuthu, P. Beyers, M. Lutz, A. L. Spek and E. Bouwman, "Electrocatalytic CO 2 conversion to oxalate by a copper complex.," *Science,* vol. 327, pp. 313-315, 2010.

[146] L. J. Farrugia, S. Lopinski, P. A. Lovatt and R. D. Peacock, "Fixing carbon dioxide with copper: crystal structure of [LCu(m-C2O 4)CuL][Ph 4 B]2 (L ¼ N,N',N''-triallyl-1,4,7-triazacyclononane)," *Inorg. Chem.,* vol. 40, pp. 558-559, 2001.

[147] D. M. Barrett Adams, I. A. Kahwa and J. T. Mague, " One-pot atmospheric carbon ioxide fixation and 'nitric acid' inclusion in the cylindrical micro-pores of the resulting lanthanide(III) oxalates.," *New J. Chem.,* vol. 22, pp. 919-921, 1998.

[148] N. d. M. Neto, H. Evangelista, T. Condom, A. Rabatael and P. Ginot, "Amazonian Biomass Burning enhances tropical Andean Glaciers Melting," *Sci. Rep.,* vol. 9, p. 16914, 2019.

[149] International Energy Agency, "Putting CO2 to Use; Creating value from emissions.," IEA Publications, 2019.

[150] J. A. Farrar, R. Grinter, F. Neese, J. Nelson and A. J. Thomson, "The electronic structure of the mixed-valence copper dimer [Cu2{N(CH2CH2N=CHCH=NCH2CH2)3N}]3+.," *J. Chem. Soc., Dalton Trans.,* vol. 21, pp. 4083-4088, 1997.

[151] D. M. D'Alessandro and F. R. Keene, "Stereochemical effects on intervalence charge transfer," *Pure Appl. Chem.,* vol. 80(1), pp. 1-16, 2009.

[152] R. L. Lucas, M. K. Zart, J. Murkerjee, T. N. Sorrell, D. R. Powell and A. S. Borovik, "A Modular Approach toward Regulating the Secondary Coordination Sphere of Metal Ions: Differential Dioxygen Activation Assisted by Intramolecular Hydrogen Bonds," *J. Am. Chem. Soc.,* vol. 128, no. 48, pp. 15476-15489, 2006.

Appendix

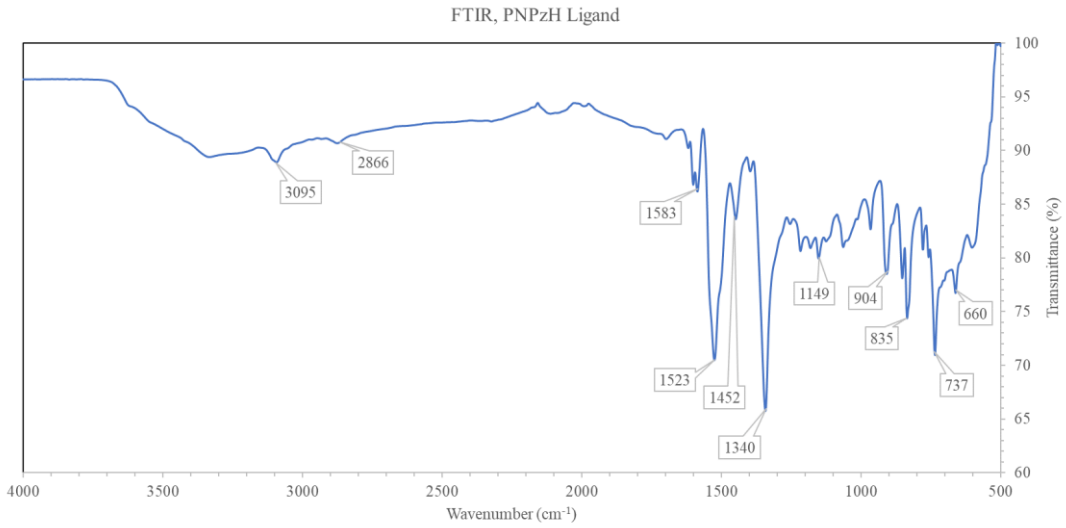

Figure A. 1. FTIR spectrum (4 cm^{-1} resolution, ATR, crystalline sample) of the PNpzH ligand.

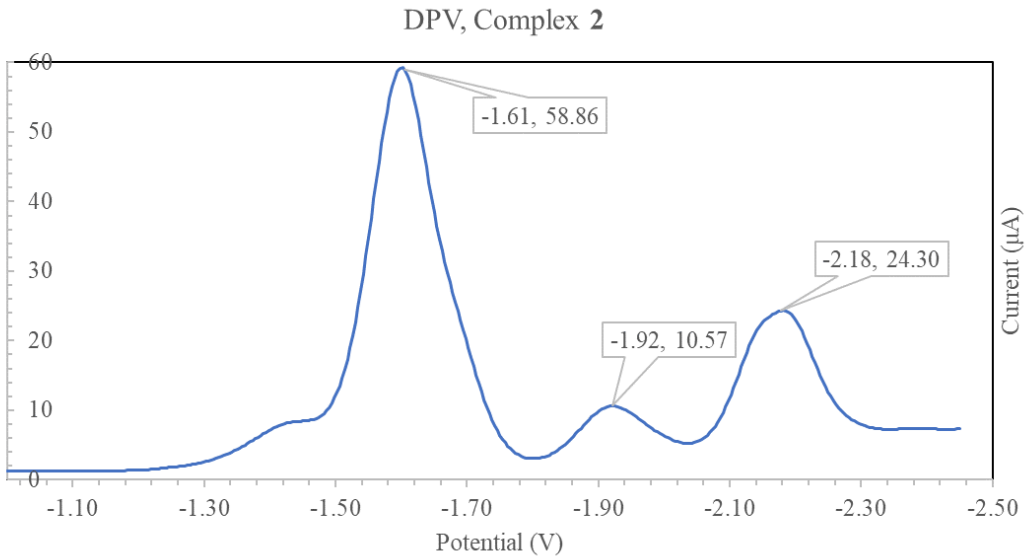

*Figure A. 2. DPV voltammogram of complex **2** (1 mM) in 0.5 M $TBAPF_6$/MeCN, glassy carbon working electrode, vs. Fc^+/Fc), showing ligand-based reductions, 100 mV scan rate.*

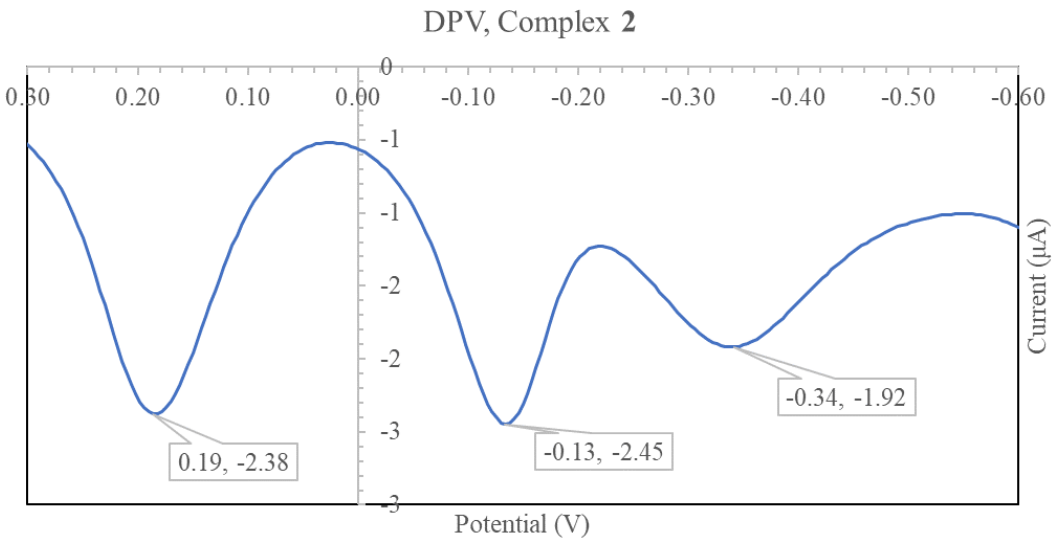

*Figure A. 3. DPV voltammogram of complex **2** (1 mM) in 0.5 M $TBAPF_6$/MeCN, glassy carbon working electrode, vs. Fc^+/Fc), showing Cu-based oxidations, 100 mV scan rate.*

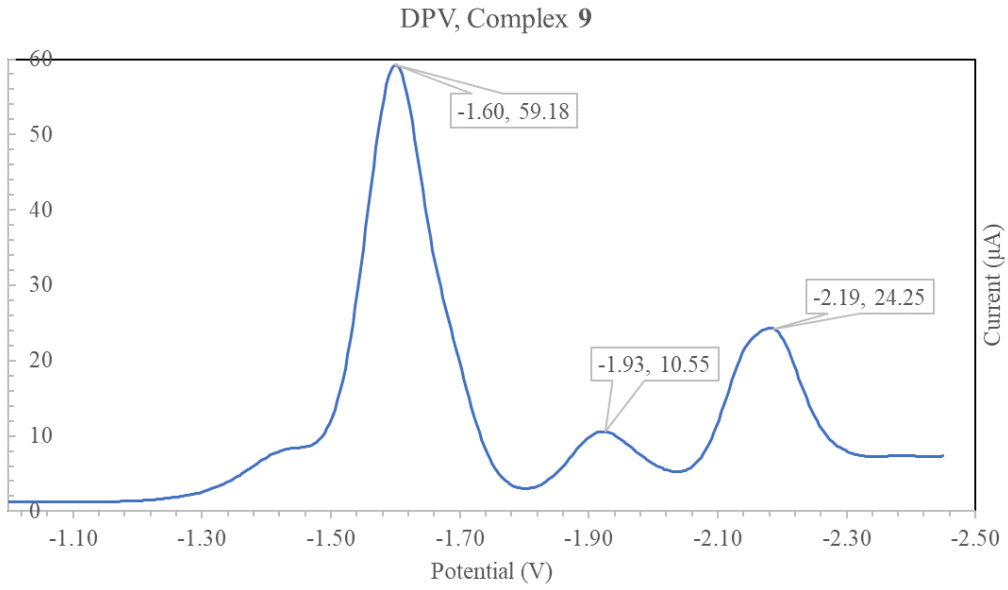

*Figure A. 4. DPV voltammogram of complex **9** (1 mM) in 0.5 M $TBAPF_6$/MeCN, glassy carbon working electrode, vs. Fc^+/Fc), showing ligand-based reductions, 100 mV scan rate.*

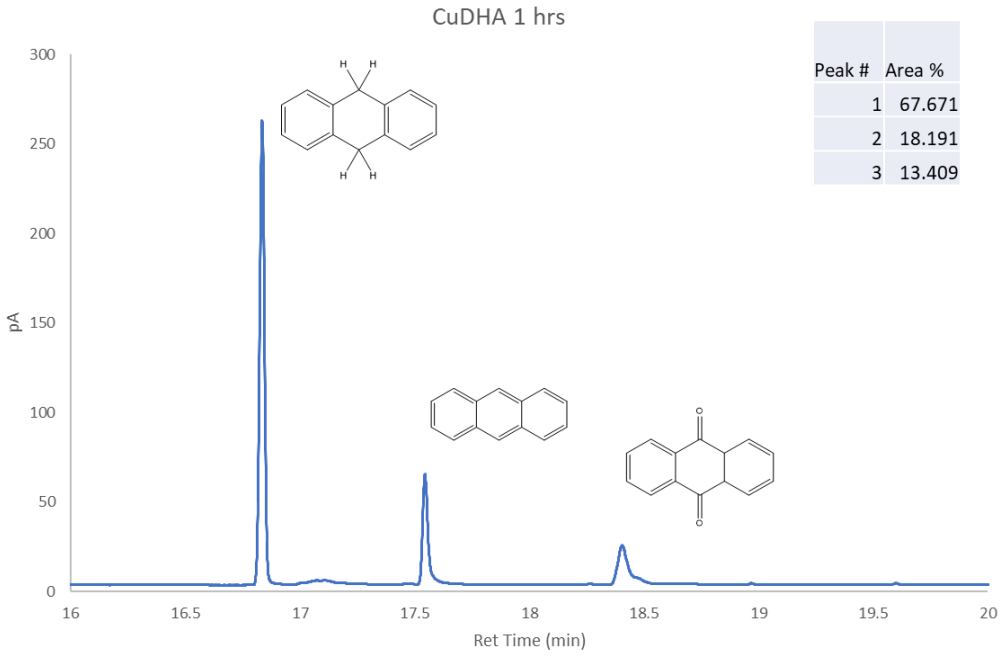

Figure A. 5. GCMS spectrum for the oxidation of DHA, 1 h, 1:100 ratio. Solution: MeCN, DHA concentration: 1 mM, catalyst concentration: 0.01 mM. Injected after 1 hr stirring at room temperature.

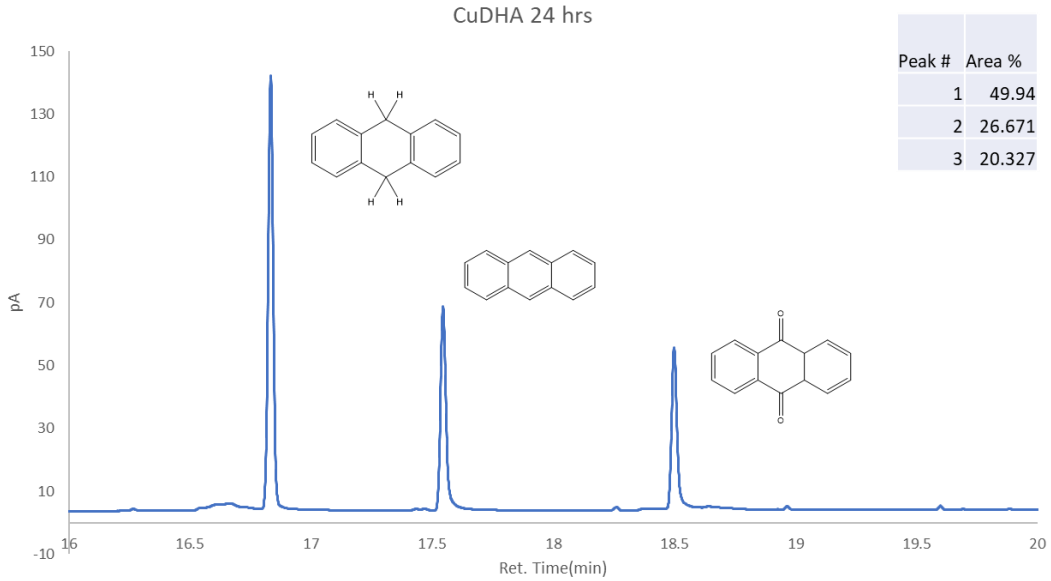

Figure A. 6. GCMS spectrum for the oxidation of DHA, 24 h, 1:100 ratio. Solution: MeCN, DHA concentration: 1 mM, catalyst concentration: 0.01 mM. Injected after 24 hrs stirring at room temperature.

VITA

EDUARDO MOLLINEDO

Born, Santa Clara, Cuba

2012-2016	B.S., Chemistry Nova Southeastern University Davie, Florida
2016-2018	Lab Assistant SERC, Florida International University Miami, Florida
2018-2023	Graduate Teaching Assistant Florida International University Miami, FL
2021	M.S., Chemistry Florida International University Miami, Florida
2021	Doctoral Candidate, Chemistry Florida International University Miami, Florida

SELECTED PUBLICATIONS AND PRESENTATIONS

- Henry O. Briceño, Eduardo Mollinedo, Sandro Stumpf, Dilip Shinde, Piero Gardinali, and Reinaldo García. "*Fractionation of Phosphorous in Canals Draining to NE Shark River Slough."* GEER 2019, Marriott Fort Lauderdale & Coral Springs, Coral Springs, FL, USA, April 22nd-25th, 2019.